

A SEARCH FOR A NEW GAUGE BOSON

Eric Lyle Jensen

Herndon, Virginia

Master of Science, College of William and Mary, 2010
Bachelor of Arts, Christopher Newport University, 2008

A Dissertation presented to the Graduate Faculty
of the College of William and Mary in Candidacy for the Degree of
Doctor of Philosophy

Department of Physics

The College of William and Mary
January 2014

©2013
Eric Lyle Jensen
All rights reserved.

APPROVAL PAGE

This Dissertation is submitted in partial fulfillment of
the requirements for the degree of

Doctor of Philosophy

Eric Lyle Jensen

Approved by the Committee, September, 2013

Committee Chair

Professor Todd Averett, Physics
The College of William and Mary

Professor David Armstrong, Physics
The College of William and Mary

Professor Carl Carlson, Physics
The College of William and Mary

Assistant Professor Michael Kordosky, Physics
The College of William and Mary

Dr. Bogdan Wojtsekhowski, Staff Scientist
Thomas Jefferson National Accelerator Facility

ABSTRACT

In the Standard Model, gauge bosons mediate the strong, weak, and electromagnetic forces. New forces could have escaped detection only if their mediators are either heavier than $\mathcal{O}(\text{TeV})$ or weakly coupled to charged matter. New vector bosons with small coupling α' arise naturally from a small kinetic mixing with the photon and have received considerable attention as an explanation of various dark matter related anomalies. Such particles could be produced in electron-nucleus fixed-target scattering and then decay to e^+e^- pairs. New light vector bosons and their associated forces are a common feature of Standard Model extensions, but existing constraints are remarkably sparse.

The APEX experiment will search for a new gauge boson A' with coupling $\alpha'/\alpha_{\text{fs}} \gtrsim 6 \times 10^{-8}$ to electrons in the mass range $65 \text{ MeV} < m_{A'} < 550 \text{ MeV}$. The experiment will study e^+e^- production off an electron beam incident on a high- Z target in Hall A at Jefferson Lab. The e^- and e^+ will be detected in the High Resolution Spectrometers (HRSs). The invariant mass spectrum of the e^+e^- pairs will be scanned for a narrow resonance corresponding to the mass of the A' .

A test run for the APEX experiment was held in the summer of 2010. Using the test run data, an A' search was performed in the mass range 175-250 MeV. The search found no evidence for an $A' \rightarrow e^+e^-$ reaction, and set an upper limit of $\alpha'/\alpha_{\text{fs}} \simeq 10^{-6}$.

TABLE OF CONTENTS

Acknowledgements	vi
1 Introduction	2
1.1 The A' Boson	3
1.2 Searching for an A'	4
1.3 Impact of the A' Search	5
2 Motivation	7
2.1 Standard Model Extensions	8
2.1.1 Kinetic Mixing	9
2.2 Dark Matter	10
2.2.1 Astrophysical Anomalies	11
2.2.2 Relic Abundance of Dark Matter	12
2.3 Anomalous Magnetic Moment	14
2.4 Current Limits	15
3 Jefferson Lab	20
3.1 CEBAF	21
3.2 Hall A	23
3.2.1 Beamline	24
3.2.2 High Resolution Spectrometers	28
3.2.3 HRS Detector Package	31
3.2.4 Data Acquisition	37
4 The APEX Experiment	40
4.1 A' Production in Fixed Target Experiments	41
4.2 Signal and Trident Kinematics	44
4.3 Accidentals and rates	49
4.4 Experimental Setup	51

4.4.1	Target	53
4.4.2	Septum Magnet	55
4.4.3	Track Measurement	55
4.4.4	SciFi Detector	57
4.4.5	Particle Identification	60
4.4.6	Trigger and DAQ	60
4.5	Proposed Measurement	63
5	The APEX Test Run	65
5.1	PAC Concerns	66
5.2	Experimental Setup	67
5.2.1	Targets	68
5.2.2	Septum and Beam Steering Magnets	68
5.2.3	Electronics and Trigger	71
6	Detector Calibrations	74
6.1	HRS Detectors	75
6.1.1	Scintillators	75
6.1.2	Gas Cherenkov Detector	77
6.1.3	Drift Chambers	78
6.2	Beam Position	80
6.3	Optics Calibration	83
6.3.1	Coordinate Systems	83
6.3.2	General Approach	85
6.3.3	Procedure	88
6.3.4	Results	91
7	Data Analysis	96
7.1	Analysis Software	97

7.2	Particle Identification	98
7.3	Event Selection	99
7.3.1	Coincidence Timing	101
7.3.2	Acceptance Cuts	102
7.3.3	Final Event Sample	103
7.4	Track Reconstruction	106
7.5	Invariant Mass Calculation and Comparison to MC Data	111
7.6	Mass Resolution	118
7.6.1	Angular Resolution	119
7.6.2	Determining the Mass Resolution	121
7.7	Addressing the PAC Concerns	124
8	Resonance Search and Results	133
8.1	Searching for a Resonance	133
8.1.1	Pseudo-data Sets	135
8.1.2	Profile Likelihood Ratio	137
8.1.3	The Look Elsewhere Effect	139
8.1.4	Search Parameters	142
8.1.5	Results	144
8.2	Setting Limits on $\alpha'/\alpha_{\text{fs}}$	144
8.2.1	Setting Limits on S	147
8.2.2	Results	148
9	Conclusion	151
9.1	Impact of the APEX Test Run Results	152
9.2	Future Experiments	152
	List of Tables	155
	List of Figures	156

Bibliography 159

ACKNOWLEDGEMENTS

First and foremost, I would like to thank my Jefferson Lab supervisor, Bogdan Wojtsekhowski. Bogdan and I worked side by side for the last three years of my graduate career. He provided me with several opportunities to work at different particle accelerator facilities around the world, which is something I will remember for the rest of my life. Bogdan has taught me the value of hard work and dedication. He was not only my supervisor at Jefferson Lab, but also my teacher, mentor, and friend. My experience working with Bogdan has molded me into the scientist/engineer that I am today, and I owe much of my success to him.

I would like to thank my advisor, Todd Averett, for introducing me to this thesis topic. I could not imagine working on a more interesting experiment than APEX. My conversations with Todd were always full of new and exciting ideas that reminded me of why I loved experimental physics. His help and advice has guided me along this path to completing my degree. He continued to support me after I accepted my job offer, despite his warnings of how difficult it would be to finish this thesis while working full time. I would not have been able to complete this journey without his assistance.

I can only attribute my understanding of physics to the wonderful teachers I have had throughout my academic career. While attending CNU, it was Edward Brash and John Hardie who encouraged me to pursue a career path in physics. Once I arrived at W&M, it was David Armstrong who finally made quantum mechanics “click” for me. I must also acknowledge Carl Carlson, who made the daunting subject of quantum field theory one of my favorite classes of all time. I would like to thank all the physics teachers I had the pleasure of meeting at W&M for all of their patience and help with the many questions I have had as a student.

While working on research at Jefferson Lab, I had the pleasure of sharing an office with Albert Shahinyan and Sergey Abrahamyan. I first met Albert as an undergraduate from CNU. Over the years we have developed a great friendship and shared many great times together. I appreciate the invaluable support he has always given me with my research, and I hope we remain friends for many years to come. Since I began my research at Jefferson Lab as a graduate student, Sergey has always helped me to understand the analysis of our data. It seems I had a new question for him every day, but I never felt bad asking because he was always happy to answer.

Working with the APEX collaboration has given me the opportunity to work with many great people. The APEX spokespeople, Rouven Essig, Philip Schuster, Natalia Toro, and Bogdan Wojtsekhowski, are some of the most brilliant scientists I have ever worked with. Jin Huang played a large role in our optics calibration, and also contributed to our calculation of the experimental mass resolution. I first met Jin while setting up the polarized ^3He target lab at Jefferson Lab. The lab became fully operational in very little time, an accomplishment that could not have been achieved without Jin’s hard work and expertise. I must also thank James Beacham, who did excellent work with our peak search analysis. The peak search was an essential part of our experiment, and I would have certainly struggled much more with writing this chapter of my thesis if it were not for the James’ help.

I am truly blessed to have met my friends at W&M. I have to thank Josh Magee, whom I managed to talk into proofreading several of my papers. With his help I was able to become a much better writer, a skill that obviously proved useful while composing this thesis. I enjoyed the time I spent with Ben Rislow working on homework sets while listening to 70's soul music. Who would have thought Aretha Franklin and quantum field theory would go together so well? Many memories were created with friends like Josh and Alena Devan, Ekaterina Mastropas, Matt Simons, Megan Ivory, Juan Carlos Cornejo, Melissa Cummings, and Lei Wang. I will always remember our weekly band practices with Austin Ziltz, Travis Horrom, and Zach Brown. I have to thank all of my friends within the W&M physics department for constantly reminding of my passion for science.

Last but not least, I have to thank my family for all of their love and support throughout this journey. Dad, thank you for encouraging me to chase my dreams. Mom, thank you for always believing in me, even when I didn't. Bailey, thank you for supporting me through all the ups and downs I have been through in my life. Thank you to all my friends for their support and encouragement during this long process. I would not have gotten this far without the support of Stevie Mitchell, Patrick Landman, David Speirs, Kevin Brown, Graham Reed, and Ashley Driskill. I am truly grateful for the support I have received from my fellow employees at IBA, whose interest in my research was a motivating factor in completing this thesis. Finally, I would like to thank my grandfather, Cecil Lumbsden, for teaching me that our family and friendships are the most important things in this world.

A SEARCH FOR A NEW GAUGE BOSON

1

Introduction

In the Standard Model, subatomic particles interact through the electromagnetic, strong, and weak nuclear forces. These interactions are mediated by force carriers called gauge bosons. The Standard Model contains three types of gauge bosons: photons, which carry the electromagnetic interaction; W^\pm and Z bosons, which carry the weak interaction; and gluons, which carry the strong interaction. Additional forces could have escaped our detection only if their mediators are heavier than $\mathcal{O}(\text{TeV})$ or weakly coupled to charged matter. The latter case can be tested through electron-nucleon fixed-target experiments.

This thesis presents the results of a search for a new force mediated by a sub-GeV gauge boson A' with weak coupling α' to electrons. The experiment was performed in Hall A at Jefferson Lab in 2010. Chapter 2 discusses the motivation for the existence of an A' boson and the current status of other experimental searches. Chapter 3 describes Jefferson Lab's CEBAF electron beam and the experimental

equipment used in Hall A. The fourth and fifth chapters describe the experimental setup of the future A' Experiment (APEX) and the test run that was held in 2010. Calibration of the experimental equipment is covered in Chapter 6, the data analysis is covered in Chapter 7, and the results of the statistical peak search are provided in Chapter 8.

1.1 The A' Boson

The A' (also known as a dark photon, heavy photon, and U boson) is a $\mathcal{O}(\text{MeV})$ spin-1 gauge boson that mediates a new $U(1)$ gauge group. The A' can mix with the ordinary photon through quantum loops. This mixing produces a small coupling of the A' to electrically charged matter. The existence of such a particle is common in many Standard Model extensions; however, existing constraints are remarkably weak.

The A' can couple to Standard Model fermions, but it also couples to dark matter. Recent astrophysical experiments observe an enormous excess in high-energy cosmic-ray electrons and positrons relative to what is expected from current models. These excesses could be explained through the annihilation of dark matter particles into A' 's, which then decay into electrons and positrons due to their ability to couple to electrically charged matter. If the A' indeed mediates the interaction of e^+e^- pairs with dark matter, it would provide a new portal through which we can explore the dark sector of our universe.

1.2 Searching for an A'

When high energy electrons scatter off material they lose energy in the form of a photon. This process is known as bremsstrahlung radiation. A' 's can be generated through the same type of process. When an electron beam collides with a fixed target, the rate at which A' 's are radiated can be reliably estimated using the Weizsäcker-Williams approximation (see Ch. 4 for more details) [1]. The radiated A' 's will decay into e^+e^- pairs whose properties can be measured with high-resolution spectrometers. A diagram of this process is shown in Fig. 1.1.

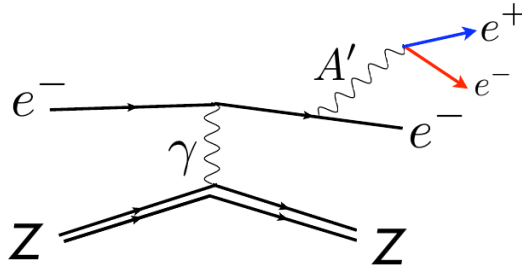


FIG. 1.1: A' 's are produced via bremsstrahlung radiation off a scattered electron beam and then decay into e^+e^- pairs.

The A' search is performed by analyzing the invariant mass of the e^+e^- pairs measured in the spectrometers. The majority of these e^+e^- pairs come from ordinary bremsstrahlung radiation of virtual photons. To search for the A' , a peak search is performed on the entire invariant mass spectrum. The identification of a significant peak on top of a uniform background would be evidence of $A' \rightarrow e^+e^-$ electro-production, with the center of the peak corresponding to the mass of the A' . The width of this peak would be equal to the mass resolution of the experiment.

An A' signal with a narrow peak would contain a higher amplitude, and therefore be easier to detect. Therefore, high experimental mass resolution is critical when searching for an A' signal. Hall A of Jefferson Lab has two identical High Resolution Spectrometers (HRSs) capable of momentum measurements with $\sigma \sim 10^{-4}$ resolution, making it an ideal setup for searching for A' s.

Because the A' has a small coupling strength α' to electrons, the A' production rate is much smaller than the rate of ordinary bremsstrahlung radiation. The A' production rate relative to ordinary bremsstrahlung radiation decreases with smaller α' . Detecting A' s with extremely small α' would therefore require collecting a massive amount of data. For this reason, the amount of data collected can be related to the search sensitivity achievable by the experiment. A high-intensity electron beam, such as the one provided at Jefferson Lab, produces more statistics and allows the experiment to be sensitive to A' s with smaller α' . Combining this with the excellent mass resolution of the two HRS setups in Hall A make Jefferson Lab an ideal location to perform an A' search.

1.3 Impact of the A' Search

The dashed box in Fig. 1.2 indicates the area of parameter space where the existence of the A' is most motivated. While this region has high discovery potential, it remains unconstrained by existing data. The APEX experiment at Jefferson Lab will explore much of this territory, probing values of $\alpha'/\alpha_{\text{fs}}$ as low as 6×10^{-8} .

The discovery of an A' could provide an explanation for the large excesses

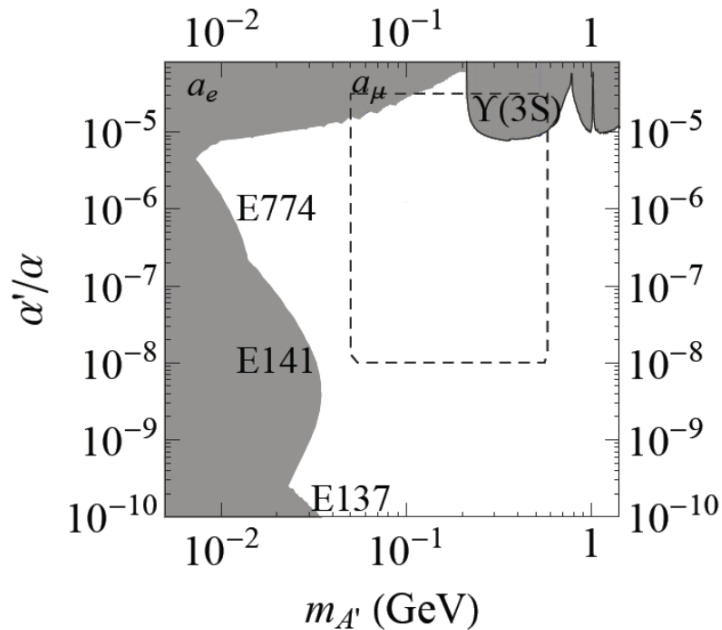


FIG. 1.2: 2-dimensional parameter space of $\alpha'/\alpha_{\text{fs}}$ vs. $m_{A'}$. The dashed box denotes the region where the A' 's existence is most motivated.

in cosmic-ray electrons and positrons observed by several recent astrophysical experiments. The coupling of A' 's to both dark and Standard Model matter could provide a new way in which we can explore the dark sector of our universe, the nature of which is one of the greatest questions perplexing scientists today. This could open doors to a new realm of yet-unobserved quantum fields and their corresponding particles. The existence of a new force mediated by A' 's may also resolve the discrepancy between the measurement and calculation of the muon anomalous magnetic moment (see Ch. 2 for more details). Due to the motivating implications of its existence and the weak constraints from existing data, a search for new A' bosons deserves immediate attention.

2

Motivation

The existence of A' bosons is theoretically natural and could explain several recent dark matter-related anomalies. Their existence could also explain the discrepancy between the measured and observed anomalous magnetic moment of the muon [2]. The A' can be a force carrier for new Abelian forces, an idea that is ubiquitous in extensions of the Standard Model [3]. Many Standard Model extensions involve a “hidden sector” or “dark sector” of the universe which contains new quantum fields and their corresponding particles that do not directly interact via the gauge boson forces of the Standard Model. This dark sector, however, may still interact indirectly with the visible sector through a kinetic mixing between the dark gauge boson A' and the photon. The existence of such A' bosons with sub-GeV masses is one of the very few remaining ways in which new forces can be added to the Standard Model.

In addition to their conformity with possible Standard Model extensions, A' s

are also motivated by recent physical observations. Several astrophysical observations show enormous deviations from what is predicted by the Standard Model [4, 5, 6, 7]. These cosmic anomalies may be evidence of dark matter annihilation with visible matter mediated by the A' . Furthermore, the existence of this new dark matter annihilation channel produces the correct relic abundance of dark matter that we see in our universe today.

In this chapter we will discuss the potential existence of new weakly coupled forces with sub-GeV mediators. We will describe the cosmic anomalies recently observed by several astrophysical experiments and how they motivate the existence of an A' . We will also discuss the muon anomalous magnetic moment and how it could be resolved by the existence of an A' . Finally, we will highlight the region of phase space with the highest motivation and show the current limits on light $U(1)$ gauge bosons.

2.1 Standard Model Extensions

The Standard Model is a well tested theory that explains the electromagnetic, weak, and strong nuclear forces that govern the interactions of subatomic particles. These three forces are mediated by force carrier particles called gauge bosons. New forces could have escaped detection only if their mediators are either heavier than $\mathcal{O}(\text{TeV})$ or weakly coupled to charged matter. The latter case can be tested using high precision colliding beam and fixed target experiments.

Many extensions of the Standard Model contain additional hidden forces under

which ordinary matter is neutral. These forces would have gone largely unnoticed because gauge symmetry prohibits renormalization interactions between Standard Model particles and the other hidden gauge bosons or matter that is charged under them [1]. Gauge bosons of hidden forces, however, can couple to charged matter through a kinetic mixing with the photon [8].

2.1.1 Kinetic Mixing

If there exists an additional $U(1)$ symmetry in nature, there will be mixing between the photon and the new gauge boson. Consider the Lagrangian

$$\mathcal{L} = \mathcal{L}_{\text{SM}} + \frac{\epsilon}{2} F^{Y,\mu\nu} F'_{\mu\nu} + \frac{1}{4} F'^{\mu\nu} F'_{\mu\nu} + m_{A'}^2 A'^{\mu} A'_{\mu}, \quad (2.1)$$

where \mathcal{L}_{SM} is the Standard Model Lagrangian, $F'_{\mu\nu} = \partial_{\mu} A'_{\nu} - \partial_{\nu} A'_{\mu}$, and A' is the gauge field of an additional $U'(1)$ gauge field [1]. The second term in (2.1) is a mixing of the kinetic terms of the $U(1)$ and $U'(1)$ gauge fields.

Kinetic mixing can be generated by loops of any heavy particle Ψ coupling to both the photon and the A' (Fig. 2.1). Kinetic mixing produces an effective interaction $\epsilon e A'_{\mu} J_{\text{EM}}^{\mu}$ of the A' with the electromagnetic current J_{EM}^{μ} . This interaction is suppressed relative to the electron charge e by the parameter ϵ , with $\epsilon^2 = \frac{\alpha'}{\alpha_{\text{fs}}} (\alpha_{\text{fs}} = \frac{e^2}{4\pi})$. These loops naturally generate $\epsilon \sim 10^{-6} - 10^{-2}$ ($\frac{\alpha'}{\alpha_{\text{fs}}} \sim 10^{-12} - 10^{-4}$) [1].

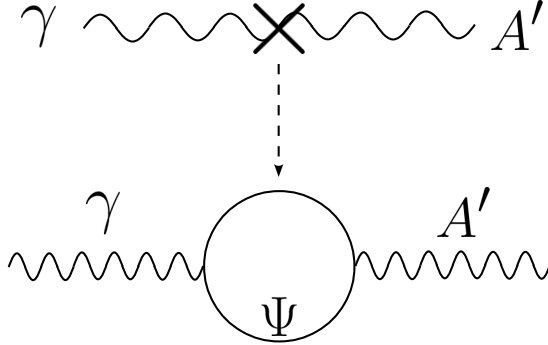


FIG. 2.1: A Feynman diagram of the kinetic mixing operator is shown at the top. This kinetic mixing is generated by loops of any heavy particle Ψ coupling to both the photon and the A' , naturally generating $\epsilon \sim 10^{-6} - 10^{-2}$.

2.2 Dark Matter

The nature of dark matter is one of the great mysteries of our universe. Dark matter accounts for about a quarter of the total mass-energy content of the observable universe, yet it does not seem to interact with any of the known Standard Model forces. Its presence is inferred only by its gravitational effects on visible matter. Recent cosmological observations, however, suggest that dark matter may couple to Standard Model matter through the exchange of an A' . The interaction of dark matter with A' s would also reproduce the theoretical success of the “WIMP miracle” in explaining the relic abundance of dark matter that we observe in our universe today. In this section we will discuss how the interaction of dark matter with A' s is well motivated both theoretically and experimentally.

2.2.1 Astrophysical Anomalies

The satellites PAMELA [4] and Fermi [5], the balloon-borne detector ATIC [6], the terrestrial-based Cherenkov telescope HESS [7], and other experiments have reported a large excess in the cosmic-ray flux of high-energy electrons and positrons relative to what is expected from normal astrophysical processes. The PAMELA results are shown in Fig. 2.2. This excess could naturally arise through the annihilation or decay of dark matter, suggesting that dark matter couples to ordinary matter through some force other than gravity.

One possible solution to the mysterious nature of dark matter is that it is composed of 10 GeV to 10 TeV particles that interact via the electroweak force (weakly interacting massive particles or WIMPs). While this theory succeeds in explaining the relic abundance of dark matter observed in our universe today (a theoretical observation known as the “WIMP miracle”), it fails to explain the observed excess of cosmic electrons and positrons. The annihilation cross-section of WIMPs required for the “WIMP miracle” is 50-1000 times smaller than what is required to explain the excess [9]. Instead, if dark matter interacts with an $\mathcal{O}(\text{GeV})$ -mass A' , the annihilation rate of dark matter in today’s universe would be enhanced sufficiently to explain the observed excess. This is explained in more detail in Sec. 2.2.2.

While the PAMELA satellite observed an excess in high-energy positrons, it did not see any excess in anti-protons [10] (see Fig. 2.2). This means that if dark matter annihilation is responsible for producing the excess of positrons, the annihilation is not producing baryons. This contradicts the idea of dark matter annihilating

through Standard Model interactions, i.e. annihilating into W^\pm or Z bosons. If dark matter annihilates into light A 's, this result would be expected since the decay of A 's into protons and anti-protons is kinematically forbidden.

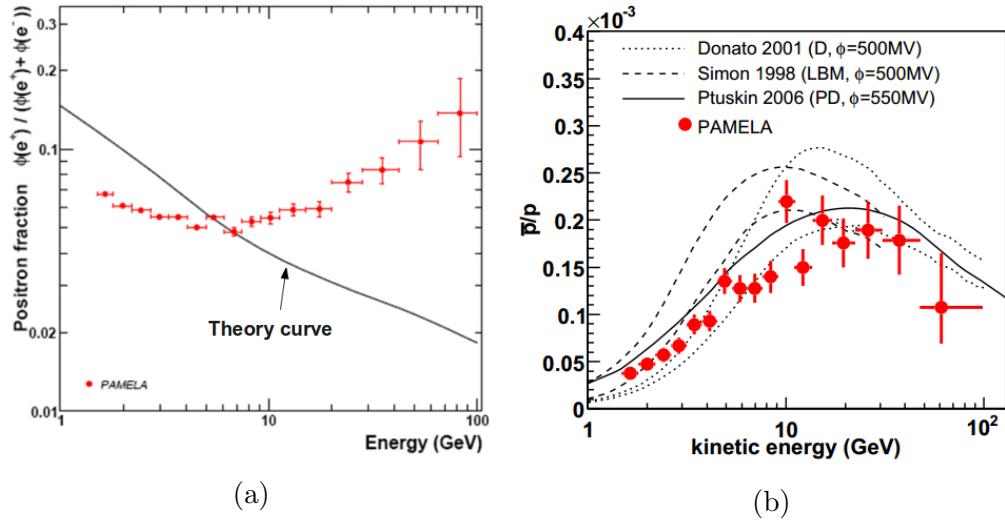


FIG. 2.2: Results from the PAMELA satellite [4]. (a) The PAMELA positron fraction compared with theoretical calculations. (b) The PAMELA anti-proton-to-proton flux compared with theoretical calculations. If dark matter annihilations are producing the extra high-energy positrons, the annihilation is not producing baryons. This result is incompatible with dark matter annihilating through Standard Model forces, but is expected for dark matter annihilating into A 's.

2.2.2 Relic Abundance of Dark Matter

During the early stages of the universe, when temperatures were extremely high, dark matter was constantly being created from and annihilating into Standard Model particles. As the universe expanded and cooled, the thermal energy of Standard Model particles decreased until it became insufficient to create dark matter. The annihilation of dark matter, however, still continued and the amount of dark matter in the universe began to decrease. Eventually the density of dark matter dropped

to a low enough level that the probability for annihilation became relatively small and the number density would “freeze-out” [11]. The amount of dark matter left in today’s universe can be roughly predicted as:

$$\Omega_{\text{DM}} \approx \frac{10^{-26} \text{cm}^3 \text{s}^{-1}}{\langle \sigma v \rangle}, \quad (2.2)$$

where $\langle \sigma v \rangle$ is the thermally averaged cross section of two dark matter particles annihilating into ordinary particles.

Dark matter composed of WIMPs would have an annihilation cross-section that produced the correct amount of dark matter we observe in our universe today. This annihilation cross-section, however, would be 50-1000 times too small to account for the observed cosmic-ray electron/positron excesses described above. Let’s instead consider the case where dark matter interacts through a force with an $\mathcal{O}(\text{GeV})$ -mass A' mediator. During the early universe, when the relative velocity of dark matter was high, the annihilation cross-section of dark matter would still have produced the correct abundance of dark matter observed in our universe today. Furthermore, the annihilation rate would be enhanced at low velocities due to Sommerfeld enhancement [12]. Sommerfeld enhancement takes into account the effect of the attractive potential created by dark matter particles due to the “long-range” force mediated by the A' . In other words, at lower velocities a dark matter particle is more likely to interact with its neighboring antiparticle, thus increasing the annihilation cross-section. Sommerfeld enhancement boosts the annihilation rate of dark matter enough to explain the observed cosmic electron/positron excesses [9].

To summarize, the interaction of dark matter with a new force mediated by a $\mathcal{O}(\text{GeV})$ -mass A' would produce the correct relic abundance of dark matter while also accounting for the large excess of high-energy cosmic-ray electron/positron flux observed by several recent astrophysical experiments. Therefore, a search for such an A' is extremely well motivated and deserves immediate attention.

2.3 Anomalous Magnetic Moment

The magnetic moment of the muon is given by the equation

$$\vec{M} = g_\mu \frac{e}{2m_\mu} \vec{S}, \quad (2.3)$$

where g_μ is the g-factor, e is the electron charge, m_μ is the muon mass, and \vec{S} is the spin angular momentum. The Dirac equation predicts $g_\mu = 2$; however, quantum loop effects lead to a small, calculable deviation parameterized by the anomalous magnetic moment

$$a_\mu \equiv \frac{g_\mu - 2}{2}. \quad (2.4)$$

This quantity can be precisely predicted in the QED framework, and also measured with great accuracy by experiment. Comparison between theory and experimental measurements provides a good test of the Standard Model, and the present result has excellent agreement for the electron. The muon, however, is ~ 200 times heavier than the electron, and therefore quantum loops with heavier particles are not suppressed (see Fig. 2.3). As a result, the muon anomalous magnetic moment is

much more sensitive to new physics beyond the Standard Model. Currently, experimental measurement disagrees with the Standard Model by 3.6 standard deviations [13].

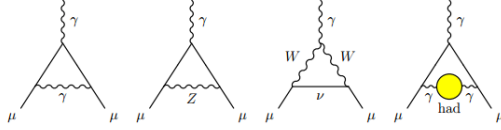


FIG. 2.3: Feynman diagrams representing the different contributions to the Standard Model muon anomalous magnetic moment. Because the muon is ~ 200 times heavier than the electron, the muon anomalous magnetic moment is more sensitive to new physics beyond the Standard Model.

The existence of a new force mediator that couples to muons, like the A' , is one possible explanation to the a_μ discrepancy. The A' contribution is like that of the photon (left side of Fig. 2.3), but suppressed by the mixing parameter ϵ^2 and dependent on the A' mass [2]. The green region in Fig. 2.4 is the 2σ band in the A' phase plane that is favored to explain the a_μ discrepancy. An interaction between muons and A' s would also have an effect on the electron anomalous magnetic moment a_e . This puts significant constraints on the existence of an A' since a_e has been confirmed experimentally with great precision. The exclusion region from a_e is shown in red in the top left corner of Fig. 2.4.

2.4 Current Limits

Additional forces with sub-GeV mediators are a common feature of Standard Model extensions and may also resolve several anomalies (see above), but existing

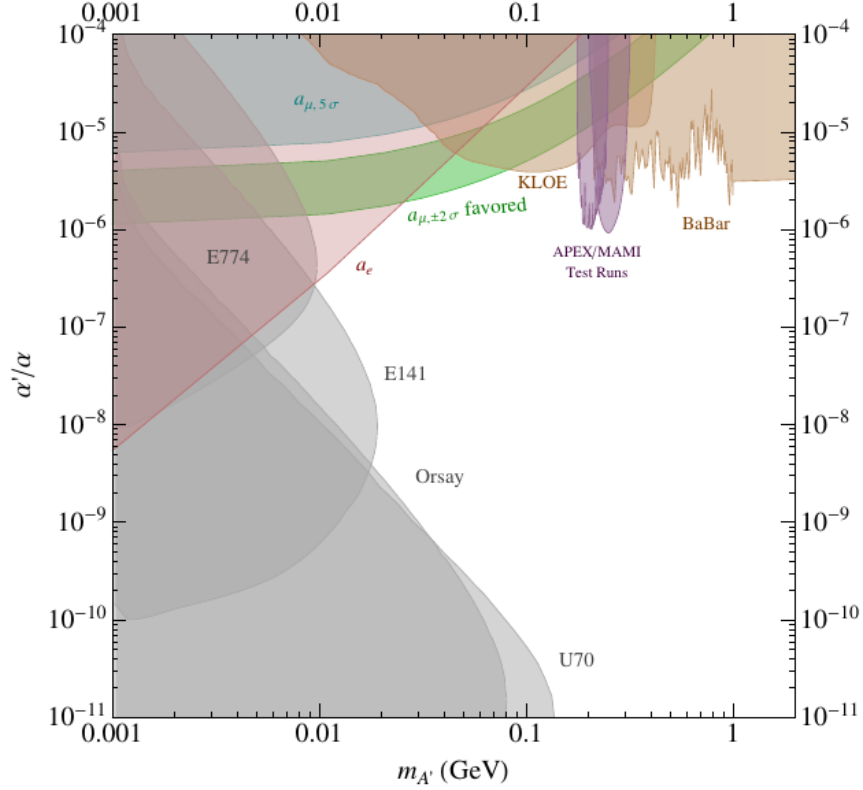


FIG. 2.4: Except for the green band, the shaded regions denote the current existing constraints on A' 's [14]. Shown are the 90% confidence level limits from the "beam-dump" experiments E141, E774, Orsay, and U70 [15], electron and muon anomalous magnetic moment measurements a_e and a_μ [2], KLOE [16], test run results from APEX [17] and MAMI [18], and the BaBar search for $\Upsilon(3S) \rightarrow \gamma\mu^+\mu^-$ [19]. The green band denotes the region where the A' can explain the observed a_μ discrepancy with 90% confidence.

constraints are surprisingly weak. The constraints on the existence of an A' can be summarized using a 2-dimensional phase plane of $\alpha'/\alpha_{\text{fs}}$ versus $m_{A'}$. Fig. 2.4 shows the regions of phase space where the existence of an A' is currently excluded. In this section we will briefly discuss these exclusion regions as well as the reach of the proposed APEX experiment.

A' s can be produced in electron collisions on fixed targets by a process analogous to ordinary photon bremsstrahlung. Electron beam experiments often use a thick shield, or a beam-stop, to stop the beam downstream of the target. There exist several “beam-stop” experiments that use detectors to look for decay products from rare penetrating particles behind the stopped electron beam. These experiments are also sensitive to A' s radiated by electrons scattering within the beam-stop, and can therefore be used to constrain the A' . Data from the E141, E774, Orsay, and U70 [15] experiments constrains $\gtrsim 10$ cm vertex displacements and $\epsilon \gtrsim 10^{-7}$ [1].

The BaBar detector at the PEP-II asymmetric-energy collider at the Stanford Linear Accelerator was used to search for $\Upsilon(3S)$ decays into a pseudoscalar a , $\Upsilon(3S) \rightarrow \gamma a \rightarrow \gamma \mu^+ \mu^-$ [19]. Assuming that A' s couple to muons, data from this search can also be used to search for $e^+e^- \rightarrow \gamma A' \rightarrow \gamma \mu^+ \mu^-$ reactions. A data sample consisting of $\sim 122 \times 10^6$ $\Upsilon(3S)$ events was used to find a 90% confidence level upper limit on $\alpha'/\alpha_{\text{fs}} \gtrsim (1 - 10) \times 10^{-6}$ with $m_{A'}$ ranging from $2m_\mu - 1$ GeV [1] (see Fig. 2.4).

The KLOE experiment at the DAΦNE e^+e^- collider in Frascati, Italy was used to search for the decay $\phi \rightarrow \eta A'$ [16]. Analysis of the data is ongoing, but

the preliminary results are shown in Fig. 2.4. Also shown are the results of the Mainz Microtron (MAMI) [18] and APEX [17] test runs. The experimental setup of the MAMI test run is very similar to that of the APEX test run (see Ch. 5). The MAMI test run data showed no evidence of $A' \rightarrow e^+e^-$ production in the mass range $\sim 200 - 300$ MeV and established a 90% confidence level upper limit of $\alpha'/\alpha_{\text{fs}} \simeq 10^{-6}$.

Although much effort has gone into placing limits on the A' , constraints on highly motivated regions of phase space remain weak. The APEX experiment at Jefferson Lab will explore these regions, improving by over two orders of magnitude the sensitivity in $\alpha'/\alpha_{\text{fs}}$ over all previous experiments. The proposed experiment will search for A' s with $\alpha'/\alpha_{\text{fs}} \gtrsim 9 \times 10^{-8}$ and $m_{A'} \simeq 100 - 500$ MeV. The sensitivity of the proposed experiment is shown in Fig. 2.5.

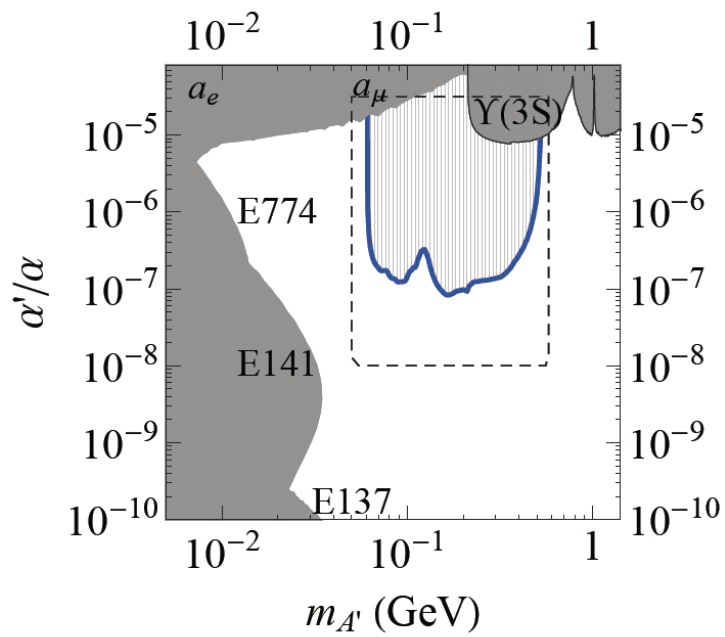


FIG. 2.5: The anticipated 2σ sensitivity for the full APEX experiment is shown in blue[20].

3

Jefferson Lab

The APEX experiment will run in Hall A of the Thomas Jefferson National Accelerator Facility (Jefferson Lab, or JLab). Jefferson Lab is a U.S. national laboratory used to study the structure of nuclear matter. The laboratory's main research tool is the Continuous Electron Beam Accelerator Facility (CEBAF). The CEBAF accelerator uses superconducting radio frequency cavities to accelerate electrons to energies up to 5.7 GeV. The electron beam is delivered to three different experimental halls where it interacts with stationary targets. Each hall can be equipped with unique spectrometers and detectors that allow physicists to study these interactions.

This chapter will describe the details of the accelerator and experimental Hall A at Jefferson Lab. The details of the APEX experimental setup will be discussed in Chapter 4.

3.1 CEBAF

The Continuous Electron Beam Accelerator Facility (CEBAF) is a medium energy electron accelerator capable of delivering continuous beams of electrons with energies up to 5.7 GeV and currents up to 200 μA . The energy and high current of this electron beam allow us to search for the A' within a particularly well motivated region of parameter space.

The CEBAF configuration consists of a polarized electron source, an injector, two linear accelerators (linacs), two sets of recirculating magnetic arcs, and extraction elements. The accelerator is capable of delivering continuous wave electron beams to three experimental halls simultaneously (Fig. 3.1).

The initial electrons are created in the injector by illuminating a single photocathode with three interlaced RF-gain-switched lasers to produce 100 keV electrons through the photoelectric effect and using an electric field gradient. The injector provides separate beams to the three experimental halls by interlacing light from three diode lasers pulsed at 499 MHz onto a strained GaAs photocathode. Separated by 120° of RF space, the three beams form a 1497 MHz train of electrons.

After the electrons are produced, they are accelerated to 5 MeV in a cryounit (a single pair of superconducting cavities) and then accelerated to 45 MeV in two cryomodules (four cryounits per cryomodule). These electrons are then injected into the main accelerator where they can accelerate to higher energies.

The main accelerator features a pair of superconducting radio frequency linacs that accelerate the electrons until they reach the desired energy. Each linac consists

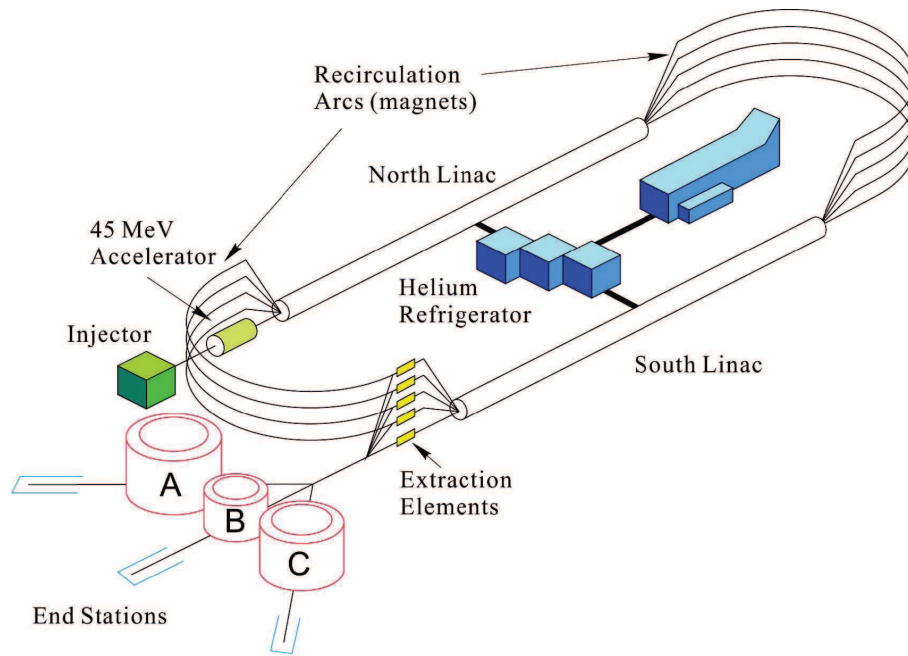


FIG. 3.1: The CEBAF accelerator layout for 6 GeV operation. The electrons are produced in the injector and then accelerated to 45 MeV before entering the main accelerator ring. The electrons can then be accelerated to up to 5.7 GeV by being recirculated five times through two linear accelerators. After the electrons reach the desired energy, the beam is simultaneously delivered to all three experimental halls.

of 160 superconducting cavities housed by 20 cryomodules. After injection, the electrons pass through the first linac and gain about 600 MeV of energy before passing through the first recirculation arc. After passing through the second linac, the “one pass” electrons can be either delivered to one of the experimental halls, or recirculated around the accelerator loop to acquire more energy and become a higher “pass” beam. The electrons can be recirculated a maximum of five times before being sent to one of the experimental halls [21].

Liquid helium is used to keep the superconducting cavities at a temperature of 2 K. The liquid helium is produced at the Central Helium Liquifier (CHL) located on site.

The properties of the beam can be monitored through the EPICS data system. Furthermore, a 499 MHz phase-locked clock is used to generate a signal for every electron bundle. This signal is sent to the CEBAF Online Data Acquisition (CODA) system for each event so that events in the detectors can be associated with a specific bundle.

3.2 Hall A

Hall A is the largest of the three experimental halls at Jefferson Lab. It has a circular shape measuring 174 ft in diameter and is 80 ft from floor to ceiling. The floor of the hall is located 35 ft below ground, and the entire hall is well shielded with concrete and a thick layer of earth to contain radiation and reduce cosmic background radiation. The basic layout of Hall A is shown in Fig. 3.2. The

experimental hall features two High Resolution Spectrometers (HRSs) that pivot around a target located at the center of the hall.

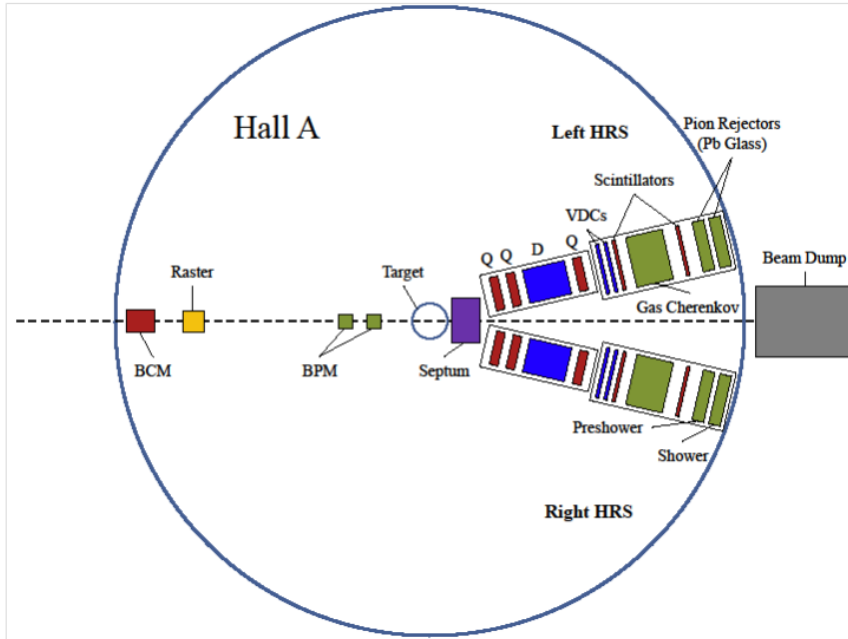


FIG. 3.2: Top view schematic of Hall A. The electron beam enters the hall from the left, then passes several beam quality monitors before hitting the target at the center of the hall. Two high resolution spectrometers are used to detect the products of the electron-target interaction.

3.2.1 Beamline

The Hall A beamline carries the beam from the beam switch yard to the target. Electrons that do not interact with the target continue along the beamline to a well shielded, isolated beam dump. Along the beamline are several components used to monitor certain properties of the beam. Some of the properties measured include

the beam's current, position, and direction. In this section, we will describe the components along the beamline that are relevant to the APEX experiment.

Beam Current Monitors

The beam current monitor (BCM) in Hall A is used to measure the current and integrated charge of the electron beam over a period of time. It consists of two RF cavities tuned to the frequency of the beam (1497 MHz), resulting in voltage levels at their outputs that are proportional to the beam current. The two RF cavities sandwich an Unser monitor, which is used as an absolute reference for calibration [22]. In addition, instrumentation at the injector section of the accelerator provides a reference for calibration. The cavities and Unser monitor are enclosed in a temperature-stabilized box located 25 m upstream of the target.

Each of the RF output signals from the two cavities is split into two parts: sampled and integrated data. The sampled data is sent to a high-precision voltmeter. The voltmeter provides an output representing the RMS value of the input signal to the EPICS data stream every 1-2 seconds. The integrated data is sent to an RMS to DC converter, and then to a Voltage-To-Frequency (VTOF) converter whose output frequency is proportional to the input voltage level. The output signals are fed to 200 MHz scalars, and accumulate during the run. At the end of the run, the scalars give a number proportional to the time-integrated voltage and therefore accurately record the integrated current, i.e., the total beam charge. The output of the RMS to DC converter is linear for currents of $5 \mu\text{A}$ to $200 \mu\text{A}$. A set of

amplifiers with gain factors of 1, 3, and 10 is used to extend the linear region to lower currents at the expense of saturating at high currents. Hence there are three signals coming from each BCM, giving six total signals going to the scalers of each spectrometer to provide beam charge data for each run. A BCM calibration is typically performed every 2-3 months, allowing the accumulated charge to be determined with an accuracy of $\pm 0.5\%$ [23].

Beam Position Monitors

Two beam position monitors (BPMs), located 7.524 m and 1.286 m upstream of the target (see Fig. 3.3), are used to determine the position and direction of the beam at the target. Each BPM contains four antennas surrounding the beamline. When the beam passes through the BPM, it induces signals on the antennas that can be measured and used to determine the position of the beam to within $100\ \mu\text{m}$ for currents above $1\ \mu\text{A}$. These BPMs provide non-destructive determination of the position and direction of the beam at the target location.

The BPMs are calibrated with respect to a set of wire scanners known as SuperHarps, which are located 7.353 m and 1.122 m upstream of the target. The positions of the SuperHarps are regularly surveyed with respect to the Hall A coordinates with the accuracy of better than $200\ \mu\text{m}$.

For each event, information from the BPMs is recorded into the CODA data stream, for each of the 8 antennas. In addition, the beam position averaged over a 0.3 s interval is logged into the EPICS datastream once every second.

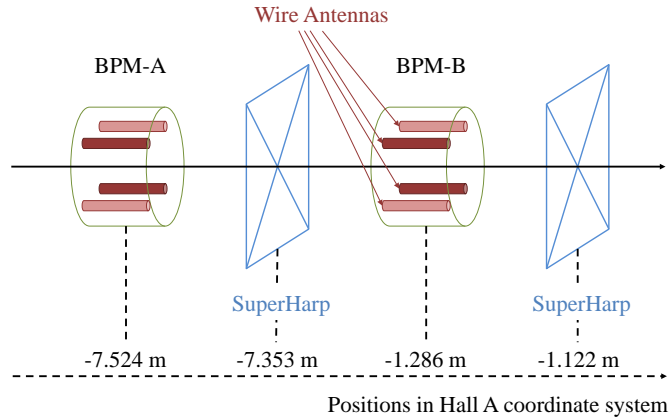


FIG. 3.3: Layout of the beam position monitors which are located upstream of the target. Each BPM contains four antennas. The relative beam position is determined using the difference-over-sum technique between two opposite antennas [24]. To determine the absolute position, the BPMs are calibrated against the SuperHarps.

Raster

If the beam position at the target were fixed at a single point, the target material would heat up to extremely high temperatures, causing damage to the target. A set of fast rastering field coils is used to produce small deviations in the beam position at the target in order to avoid overheating the target material. The fast rastering system, located 23 m upstream of the target, produces deviations of several mm in both directions at the target location. It is able to sweep across the range at a rate of 17 to 24 kHz. The current supplied to the raster is recorded into the CODA data stream for each event to be used to accurately determine the beam position at the target. Fig. 3.4 illustrates an example of a reconstructed beam spot using a $2.5 \times 2.5 \text{ mm}^2$ raster size.

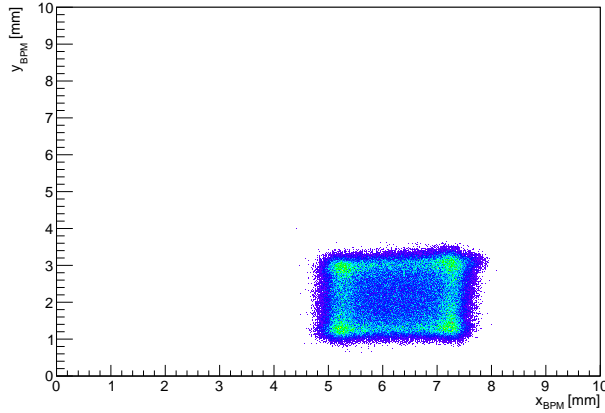


FIG. 3.4: Reconstructed beam spot determined by the BPMs for a $2.5 \times 2.5 \text{ mm}^2$ raster size.

Beam Dump

After passing the target, the exiting electron beam travels down a thin-walled aluminum spiral corrugated pipe towards the beam dump. The end of the corrugated pipe is connected to a beam diffuser which diffuses the beam over the beam dump surface. The beam dump is designed to operate at a maximum beam power of 900 kW and $190 \mu\text{A}$.

3.2.2 High Resolution Spectrometers

Hall A boasts a pair of $4 \text{ GeV}/c$ superconducting High Resolution Spectrometers (HRSs), which are nominally identical in terms of their magnetic properties. The vertical bending design includes two quadrupoles followed by a dispersive dipole. Following the dipole is a third quadrupole. The (QQDQ) configuration is used to deflect charged particles 45° upward toward the detector hut (Fig. 3.5). All magnets are superconducting and have independent cryogenic controls and reservoirs.

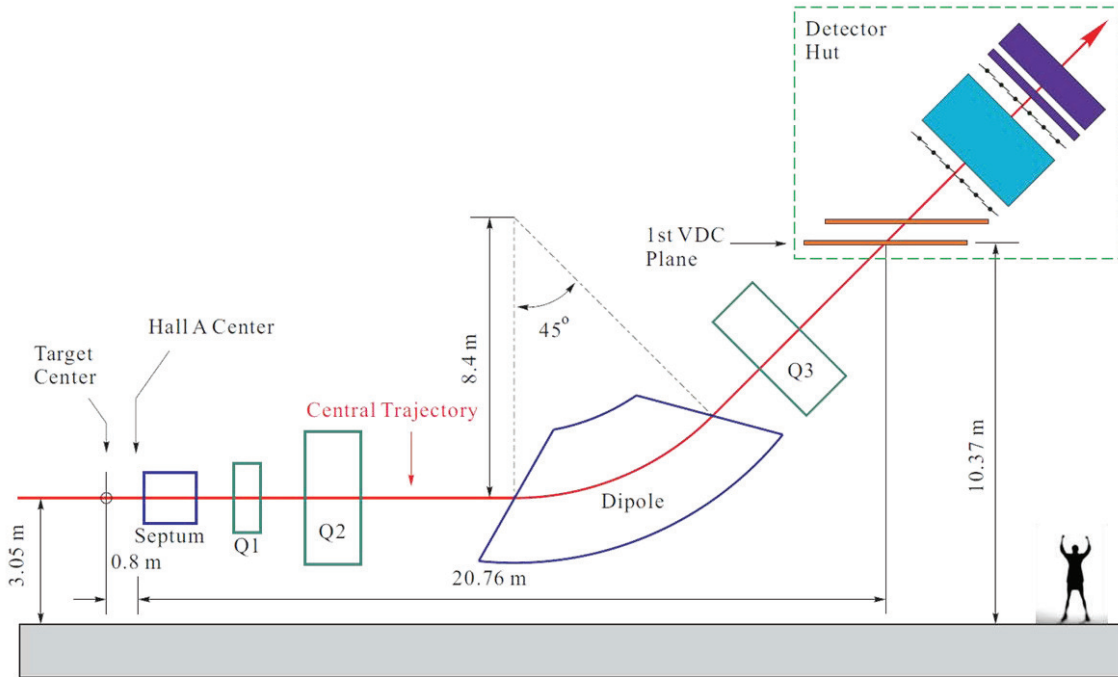


FIG. 3.5: Schematic layout of an HRS. The septum dipole magnet bends charged particles with small scattering angles toward the spectrometer. Two quadrupole magnets focus the incoming particles into the dispersive dipole magnet. The dipole magnet bends the charged particles 45° upward, and the final quadrupole magnet focuses the particles into the detector hut.

The main purpose of the HRSs is to measure the momentum of particles scattered from the target. The momentum of a charged particle is determined by analyzing the trajectory of the particle through the spectrometer. When charged particles enter the spectrometer, the dipole magnet bends the particles vertically upward. The angle at which the particle bends depends on the particle's momentum. Vertical drift chambers are used to measure the position and angle of incoming particles. This information is used to reconstruct the particle's trajectory back to the target. The momentum of the particle can then be calculated using information from the

reconstructed track and the magnetic setting of the spectrometer. More details on the magnetic optics of the HRSs will be discussed in Sec. 6.3.

The HRSs were designed to provide a high momentum resolution, large acceptance in both angle and momentum, good position and angular resolution in the scattering plane, an extended target acceptance, and a large angular range. The momentum resolution of the HRSs is better than 2×10^{-4} over a 0.4 to 4.0 GeV/ c momentum range. The momentum acceptance is $\pm 4.5\%$ with an angular acceptance of ± 30 mrad horizontal and ± 60 mrad vertical. Table 3.1 summarizes the general characteristics of the HRSs. More details can be found in [23].

TABLE 3.1: Main design characteristics of the Hall A High Resolution Spectrometers. The resolution values are for the full width at half maximum (FWHM).

Configuration	QQDQ vertical bend
Bending angle	45°
Optical length	23.4 m
Momentum range	0.3 – 4.0 GeV/ c
Momentum acceptance	$-4.5\% < \delta p/p < +4.5\%$
Momentum resolution	1×10^{-4}
Angular range	
Left HRS	$12.5 - 150^\circ$
Right HRS	$12.5 - 130^\circ$
Angular acceptance	
Horizontal	± 30 mrad
Vertical	± 60 mrad
Angular resolution	
Horizontal	0.5 mrad
Vertical	1.0 mrad
Solid angle at $\delta p/p = 0, y_0 = 0^a$	6 msr

^aDetector coordinate system, see Fig. 6.5

3.2.3 HRS Detector Package

The HRS detector package is designed to perform various measurements of charged particles passing through the spectrometer. The detectors provide a trigger to activate the data acquisition electronics, collect tracking information (position and direction), precisely measure the timing for time-of-flight measurements and coincidence determination, and identify the scattered particles. The detector package and all data-acquisition (DAQ) electronics are housed within a shielding hut for protection from radiation. Each detector package is composed of a pair of vertical drift chambers (VDCs), scintillator planes, Cherenkov detectors, and electromagnetic calorimeters (Fig. 3.6).

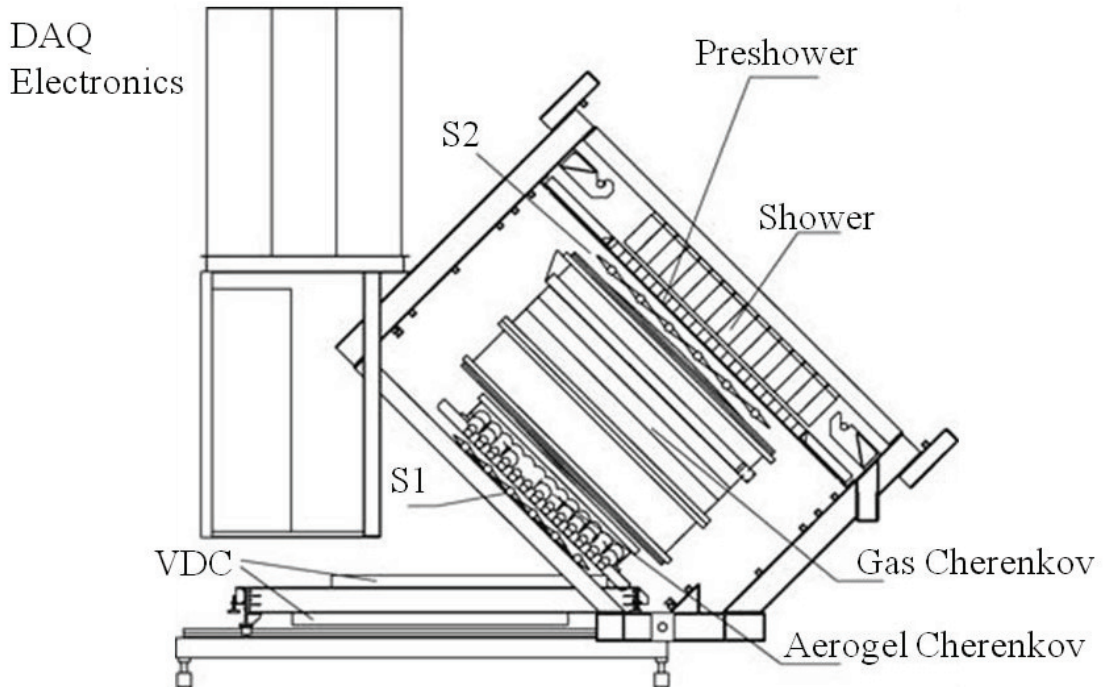


FIG. 3.6: Side view of the detector stack. The relevant detectors for the APEX test run are the VDCs, S2m plane, gas Cherenkov, and electromagnetic calorimeter.

Vertical Drift Chambers

A pair of Vertical Drift Chambers (VDCs) provides precise ($\pm 125 \mu\text{m}$) particle tracking information for each HRS. The lower VDC is positioned to coincide as closely as possible with the focal plane of the HRS, and the second VDC is positioned right above it to provide precise angular reconstruction of particle trajectories. Each VDC chamber contains two wire planes (labeled U and V) separated by about 105 mm. The wires of each successive plane are oriented at 90° to one another and lie within the laboratory horizontal plane. The wires are oriented at an angle of 45° with respect to the dispersive and non-dispersive directions, as shown in Fig. 3.7. Each plane consists of 368 wires, spaced 4.24 mm apart from one another [25].

The VDC chamber is filled with a gas mixture of argon (62%) and ethane (38%). The VDCs normally operate with their cathode planes at -4 kV, but for the APEX test run the planes were set to -3.5 kV due to the expected high rates. Custom-made discriminator cards were also installed to allow the VDCs to operate at very high rates (see Sec. 4.4.3).

As charged particles pass through the chamber, they ionize the gas. These ions drift along the electric field lines defined by the cathode planes and are collected on the signal wires in the form of an analog pulse. The pulses are then amplified, discriminated, and used to start multihit Time-to-Digital converters (TDCs) operating in common stop mode. The TDC data is read out to the CODA data stream, and tracking algorithms are applied offline to provide information about the position and direction of the track.

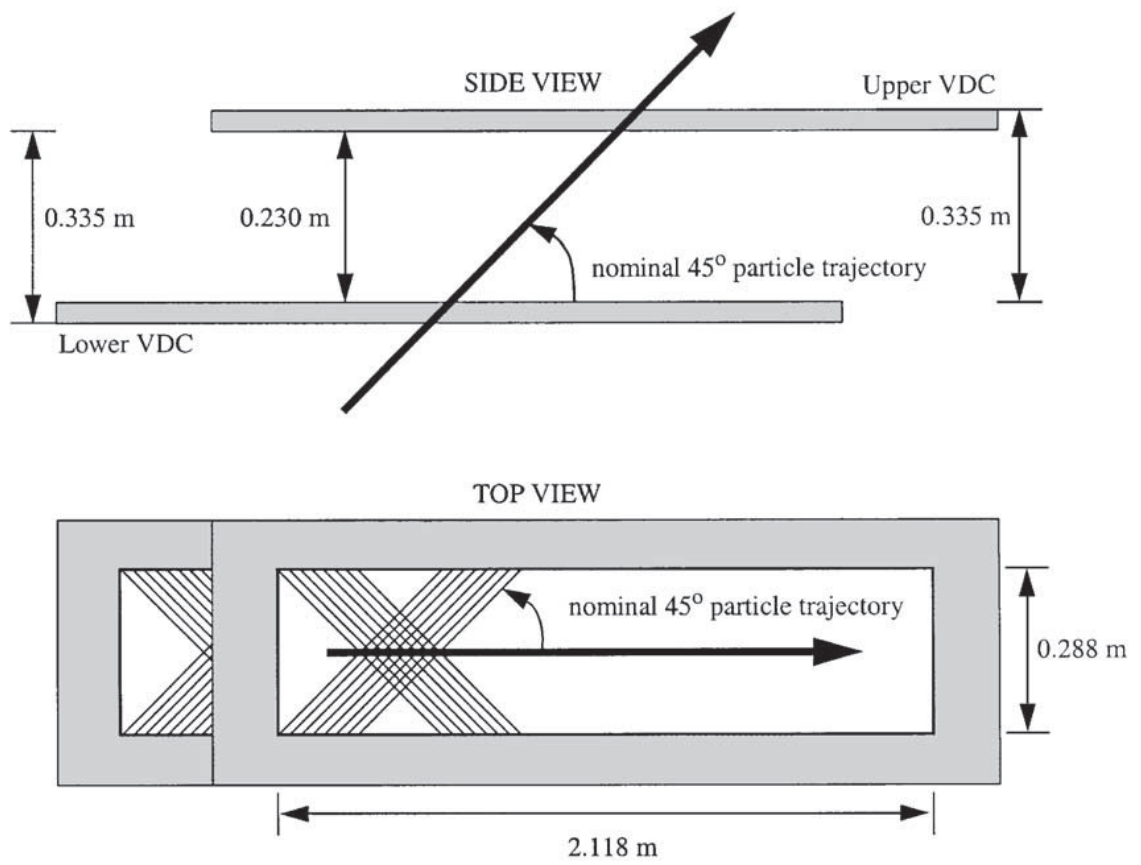


FIG. 3.7: Schematic layout of the VDCs (not to scale).

Scintillators

The S2m scintillator plane provides triggering and timing information for each HRS. The S2m plane consists of sixteen bars made of fast plastic scintillator (Eljen EJ-230). Each bar measures 17 in by 5.5 in by 2 in thick, and is wrapped with 25 μm of mylar and 50 μm of black tedlar. Trapezoidal lucite light guides on both ends couple the bar to 2" photomultiplier tubes (Photonis XP2282B). Fig. 3.8 shows a schematic layout of the S2m plane.

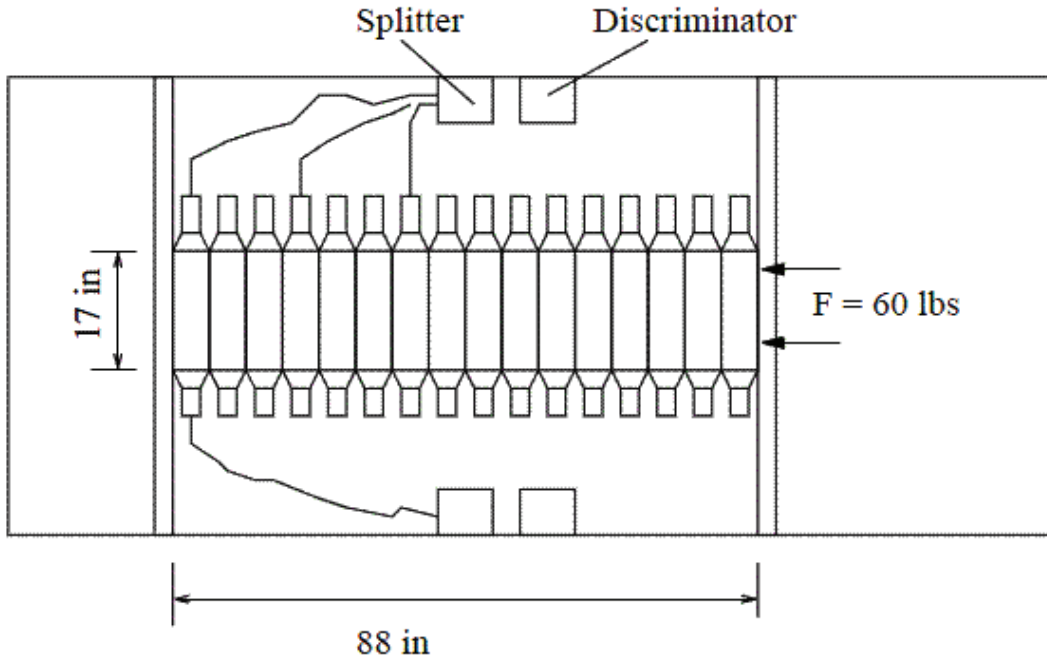


FIG. 3.8: Schematic layout of the S2m scintillator plane.

Although the S2m plane is relatively thick, it is located behind the tracking VDCs and the gas Cherenkov and does not compromise particle detection. For cosmic rays, each PMT observes about 900 photo-electrons. The average timing resolution for each PMT is $\sigma_{pmt} < 150$ ps [26].

An additional S0 scintillator paddle is used for the timing calibration of the

detectors. The S0 paddle is a 10 mm thick BICRON 408 plastic scintillator with an active area that is 170 cm long by 25 cm wide. Each end of the paddle is coupled to a 3" PMT (Photonis XP4312B). The S0 paddle is located between the VDCs and the gas Cherenkov detector, and is vertically oriented (perpendicular to the S2m paddles). The timing resolution of the S0 counter is $\sigma_t \approx 200$ ps [26].

Gas Cherenkov Detectors

Particle identification is provided by a gas Cherenkov detector filled with CO₂ at atmospheric pressure which is mounted between the S0 counter and the S2m plane. The detector consists of ten spherical mirrors with an 80 cm focal length, each viewed by a 5" PMT (Burle 8854). The mirrors are placed at the back of the detector near the output window and are grouped into two columns of five mirrors (Fig. 3.9).

If a charged particle passes through a dielectric medium at a speed greater than the phase velocity of light in that medium, such that $v/c > 1/n$ (where n is the index of refraction of the medium), the particle emits Cherenkov light. When Cherenkov light is produced in the gas Cherenkov detector, the light reflects off of the mirrors into the PMTs. For electrons, the momentum threshold to produce Cherenkov light in our detector is 0.017 GeV/ c , which is sufficiently low. For pions, the momentum threshold is 4.8 GeV/ c , which is above the momentum acceptance range of the HRSs (4 GeV/ c). Detection of Cherenkov radiation can thus be used to tag electrons and can even be used as part of the online trigger of the HRS.

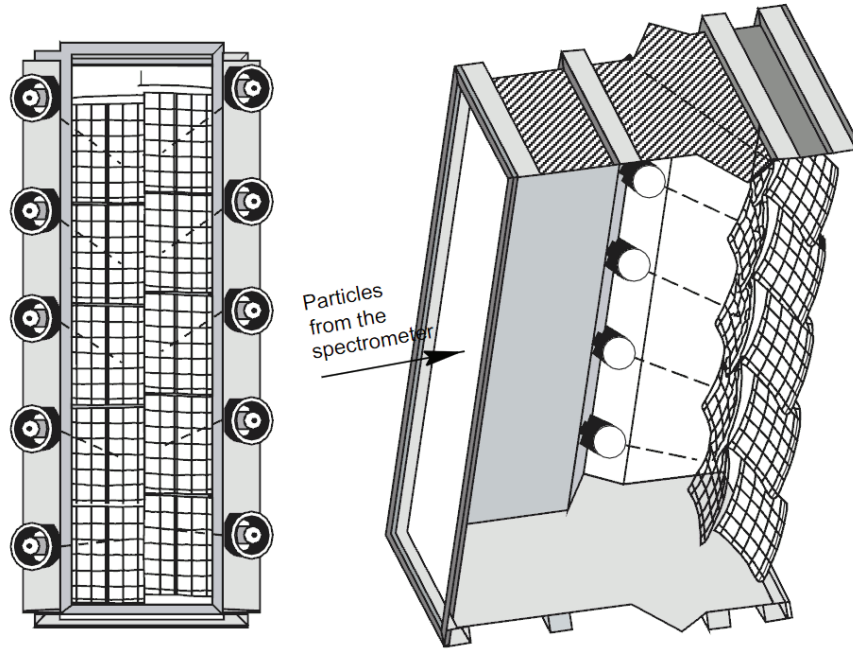


FIG. 3.9: Schematic layout of the gas Cherenkov detector.

Electromagnetic Calorimeters

The electromagnetic calorimeters, or shower detectors, also provide good particle identification. The shower detectors of both HRSs are located behind the S2m plane. However, their configurations are slightly different for each spectrometer. Fig. 3.10 shows the structure of the shower detectors for both HRSs. The blocks in both layers in the left HRS (used to detect electrons) and the first layer of the right HRS (used to detect positrons) are oriented perpendicular to the particle tracks. In the second layer of the right HRS, the blocks are parallel to the tracks. The first (second) layer of the left HRS consists of 34 lead glass blocks of dimensions 15 cm by 15 cm by 30 (35) cm. The front layer of the right HRS consists of 48 lead glass blocks of dimensions 10 cm by 10 cm x 35 cm, and the second layer consists of 80 lead glass blocks of dimensions 15 cm by 15 cm by 35 cm. All blocks are coupled to

a single PMT (Photonis XP2050) [26].

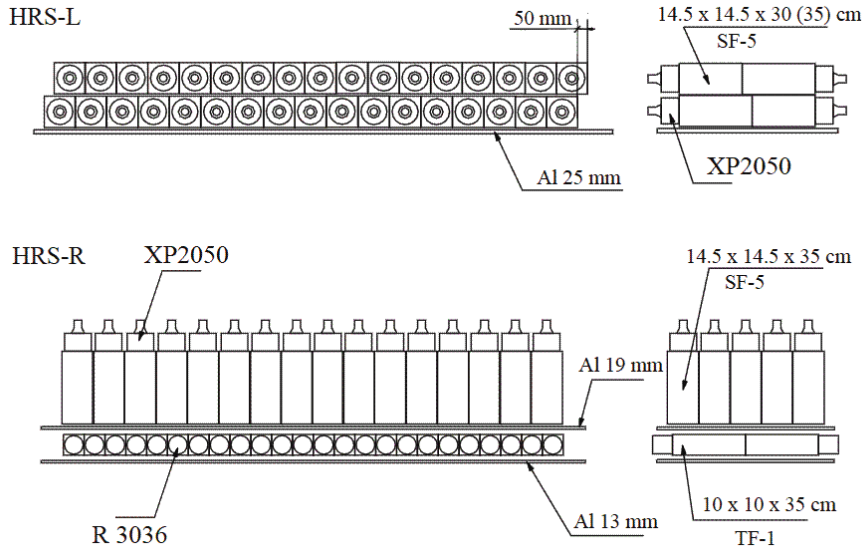


FIG. 3.10: Schematic layout of the shower detectors in the left HRS (top) and right HRS (bottom). Particles enter from the bottom of the figure.

The energy of electrons is fully absorbed in the shower detectors. About 20% of hadrons pass through the shower detectors without interaction, releasing only ionization energy. Of the other 80%, many particles escape from the detector with a large fraction of their initial energy. Plotting the ratio of energy deposited in the shower detectors to the particle's initial momentum can thus be used for identification of electrons.

3.2.4 Data Acquisition

Experiments in Hall A use the CEBAF On-line Data Acquisition system (CODA) to collect data during the experiment. CODA [27] is the standard data acquisition system designed for use at Jefferson Lab. It provides software tools for monitoring, accumulating, recording, and decoding data taken during experiments.

The raw signals from detectors are first amplified and then sent to Analog-to-Digital converters (ADCs), which are used to measure the integrated charge of the raw signals. Copies of the signals are also sent to discriminators, which produce new logic signals with fixed width and amplitude for incoming signals with amplitudes greater than the discriminator threshold. These logic signals are then sent to Time-to-Digital converters (TDCs) and scalers to provide timing and counting information. These modules are all installed on the front-end crates. The operation of modules in a single crate is controlled by the Readout Controller (ROC). ROCs are single-board computers mounted at the beginning of each crate. Each ROC is loaded with a programming script that specifies the types of modules in the crate, their positions within the crate, and certain properties of each module (such as the number of channels). ROCs also manage the communication of the crate through an Ethernet network that transports data from the modules to the CODA Event Builder (EB). The EB is a program that collects information from all modules and constructs a single data structure. This structure is called an event. The data is then sent to the CODA Event Recorder (ER), which records the event.

The trigger supervisor (TS) decides which events are recorded and which are rejected based on the experiment-specific triggering system. Trigger signals are accepted by the TS through eight input channels, T1 to T8. The TS decides which trigger signals to accept based on a set of scaling factors called pre-scale factors, and is capable of accepting multiple triggers. When a trigger signal is accepted, the TS returns a Level One Accept (L1A) pulse, which tells the ROCs to start

reading data from the modules. During this data readout, the TS is unable to accept any additional signals until the ROCs are finished processing the data. The time that the TS is unable to record new triggers is called DAQ dead time. Dead time tells us the percentage of triggers (good events) that were not recorded and can be determined by comparing the number of recorded CODA events with the number of scaler events.

In addition to the CODA system, the Experimental Physics and Industrial Control System (EPICS) is used to provide slow, real-time information about the incoming beam, target, and spectrometer magnets. This data is typically stored every few seconds into a raw data file with ASCII format.

During the experiment, data taking is controlled by operators in the Hall A counting house using the CODA graphical user interface (GUI) known as Run Control. The Run Control GUI is first used to load configuration scripts to all relevant parts of the DAQ for proper readout of the detectors. After CODA is properly configured, the GUI is used to start and stop the data acquisition. During data taking, the GUI allows the user to check the data recording rate and dead time. The data recorded between each start and stop is called a run. Each run is assigned a sequential run number and is written to a local disk array. Recorded runs are later sent to a tape silo called the Mass Storage System (MSS) for long-term storage.

4

The APEX Experiment

The APEX experiment will search for an A' with a mass ranging from 65 to 550 MeV and couplings as small as $\alpha'/\alpha_{\text{fs}} \approx 6 \times 10^{-8}$ [20]. The experiment will measure the invariant mass spectrum of e^+e^- pairs produced by electron scattering on a high- Z target. This spectrum will be scanned for a narrow peak with a width corresponding to the mass resolution of the experiment. The e^- and e^+ will be detected in the High Resolution Spectrometers (HRSs). The HRSs contain detectors to accurately measure the momentum, direction, and identity of the incoming particles.

In this chapter I will discuss A' production in fixed target experiments and give an overview of the APEX experimental setup.

4.1 A' Production in Fixed Target Experiments

An A' can be produced by colliding charged particles with nuclei, and can decay into e^+e^- or $\mu^+\mu^-$ pairs. An electron beam scattering off a high- Z target will produce A' 's through bremsstrahlung reactions with a cross section

$$\sigma_{A'} \sim 100\text{pb} \left(\frac{\epsilon}{10^{-4}}\right)^2 \left(\frac{100\text{MeV}}{m_{A'}}\right)^2, \quad (4.1)$$

where $m_{A'}$ is the mass of the A' and $\epsilon^2 \equiv \alpha'/\alpha$ is the ratio of the A' and electromagnetic fine structure constants [28]. This cross section is several orders of magnitude greater than the A' production cross sections in colliding electron and hadron beams [20]. Electron fixed-target experiments can have a high luminosity and favorable kinematics, and are therefore perfectly suited for searching for the A' in the sub-GeV mass range.

An A' is radiated from electrons scattering off target nuclei in a process analogous to ordinary photon bremsstrahlung (Fig. 4.1). When a charged particle decelerates from the deflection of other charged particles, the moving particle loses kinetic energy in the form of a photon. This process is known as bremsstrahlung.

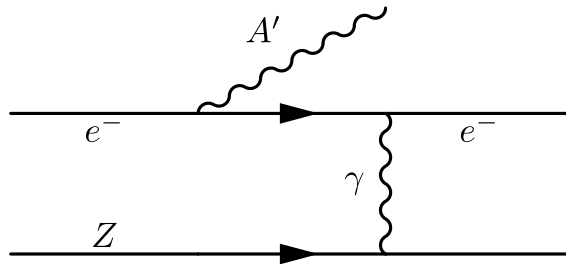


FIG. 4.1: A' production by bremsstrahlung from an incoming electron scattering off protons in a target with atomic number Z .

The production of A' s from scattered electrons can be reliably estimated using the Weizsäcker-Williams approximation [1]. For an incoming electron with energy E_0 , the differential cross section to produce an A' with mass $m_{A'}$ and energy $E_{A'} \equiv xE_0$ (where x is a constant less than one) is

$$\frac{d^2\sigma}{dx d\cos(\theta_{A'})} \approx \frac{8Z^2\alpha_{\text{fs}}^3\epsilon^2 E_0^2 x}{U^2} \tilde{\chi} \times \left[\left(1 - x + \frac{x^2}{2}\right) - \frac{x(1-x)m_{A'}^2(E_0^2 x \theta_{A'}^2)}{U^2} \right] \quad (4.2)$$

where Z is the atomic number of the target, $\alpha_{\text{fs}} \simeq 1/137$, $\theta_{A'}$ is the angle in the lab frame between the emitted A' and the incoming electron,

$$U(x, \theta_{A'}) = E_0^2 x \theta_{A'}^2 + m_{A'}^2 \frac{1-x}{x} + m_e^2 x \quad (4.3)$$

is the virtuality of the intermediate electron in initial-state bremsstrahlung, and $\tilde{\chi} \equiv \chi/Z^2 \sim 0.1 - 10$ is the reduced Weizsäcker-Williams effective photon flux, which depends on kinematics, atomic screening, and nuclear size effects. The above results are valid for

$$m_{e^-} \ll m_{A'} \ll E_0, \quad x\theta_{A'}^2 \ll 1. \quad (4.4)$$

Dropping m_{e^-} and performing the angular integration gives us

$$\frac{d\sigma}{dx} \approx \frac{8Z^2\alpha_{\text{fs}}^3\epsilon^2 x}{m_{A'}^2} \left(1 + \frac{x^2}{3(1-x)}\right) \tilde{\chi} \quad (4.5)$$

The rate and kinematics of massless bremsstrahlung and massive A' -strahlung differ in several important ways [20]:

- The A' production rate is proportional to $\frac{\alpha_{\text{fs}}^3 \epsilon^2}{m_{A'}^2}$. Therefore, it is suppressed relative to photon bremsstrahlung by $\epsilon^2 \frac{m_{e^-}^2}{m_{A'}^2}$. Additional suppression can occur for small $\tilde{\chi}$ when $m_{A'}$ is large or E_0 is small.
- When $x \approx 1$ (so that $E_{A'} \approx E_0$), $U(x, 0)$ is minimized and the production rate is sharply peaked. When the A' is produced, it carries nearly all of the beam energy.
- A' emission is dominant at angles $\theta_{A'}$ such that $U(x, \theta_{A'}) \lesssim 2U(x, 0)$ (beyond this point, wide-angle emission falls as $1/\theta_{A'}^4$). For x near its median value, the cutoff emission angle is

$$\theta_{A' \text{max}} \sim \max \left(\frac{\sqrt{m_{A'} m_{e^-}}}{E_0}, \frac{m_{A'}^{3/2}}{E_0^{3/2}} \right). \quad (4.6)$$

This is much smaller than the opening angle of the A' decay products, which is $\sim m_{A'}/E_0$.

Using Eq. (4.5), we can obtain approximate expressions for the rate of A' production. These approximations are correct within about one order of magnitude [20]. The number of A' 's produced when N_{e^-} electrons scatter in a target of thickness $T \ll 1$ radiation lengths is

$$N_{A'} \sim N_{e^-} \frac{N_0 X_0}{A} T \frac{Z^2 \alpha_{\text{fs}}^3 \epsilon^2}{m_{A'}^2} \tilde{\chi} \sim N_{e^-} \zeta T \epsilon^2 \frac{m_{e^-}^2}{m_{A'}^2}, \quad (4.7)$$

where X_0 is the radiation length of the target in g/cm^2 , $N_0 \simeq 6 \times 10^{23} \text{ mol}^{-1}$ is Avogadro's number, and A is the target atomic mass in g/mol . The numerical factor $\zeta \approx 5$ is logarithmically dependent on the choice of nucleus and on $m_{A'}$ [1]. For a Coulomb of incident electrons

$$\frac{N_{A'}}{\text{Coulomb}} \sim 10^6 \tilde{\chi} \left(\frac{T}{0.1} \right) \left(\frac{\epsilon}{10^{-4}} \right)^2 \left(\frac{100\text{MeV}}{m_{A'}} \right)^2. \quad (4.8)$$

4.2 Signal and Trident Kinematics

The A' signal will appear as a small resonance in the QED trident invariant mass spectrum. The kinematic differences between the A' signal and QED trident backgrounds are of primary consideration in selecting the optimal spectrometer settings for APEX. In this section we will discuss the kinematics of these processes.

The dominant QED backgrounds for A' production are the radiative trident and Bethe-Heitler trident reactions. The diagrams of these two processes are shown in Fig. 4.2. The production of these trident background events was simulated using the nuclear elastic and inelastic form-factors found in [29]. The simulation was done using MadGraph and MadEvent [30]. MadGraph is a matrix element generator written in the Python programming language, and MadEvent is a package derived from MadGraph used to simulate events. The effect of nuclear excitations on the kinematics in inelastic processes was neglected. The MadEvent code was also modified to account for the nucleus-electron kinematics [20].

A' signal events have the same kinematics as radiative trident events whose

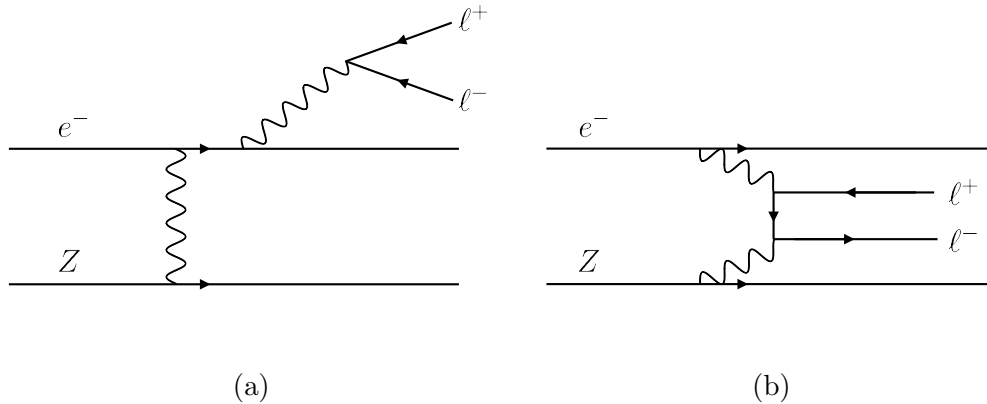


FIG. 4.2: Diagrams of (A) radiative trident and (B) Bethe-Heitler trident reactions that comprise the QED background of the $A' \rightarrow \ell^+\ell^-$ search channels.

invariant mass is inside a small window centered at the mass of the A' . The rate of A' events is related to the radiative trident cross section by

$$\frac{d\sigma(e^- Z \rightarrow e^- Z(A' \rightarrow \ell^+\ell^-))}{d\sigma(e^- Z \rightarrow e^- Z(\gamma^* \rightarrow \ell^+\ell^-))} = \left(\frac{3\pi\epsilon^2}{2N_{\text{eff}}\alpha_{\text{fs}}} \right) \left(\frac{m_{A'}}{\delta m} \right) \quad (4.9)$$

where N_{eff} is the number of available decay products and δm is the width of the invariant mass window [1]. A Monte Carlo simulation was performed simulating A' signal events and radiative background events restricted to a small mass window δm . The simulation showed almost perfect agreement with equation (4.9) [20]. Therefore, a radiative background subsample can be used to analyze the A' signal.

The Bethe-Heitler process has a much larger cross section than both the signal and radiative processes, but much different kinematics. A' 's are produced forward carrying most of the beam energy, while the recoiling electrons are soft and scatter at wide angles. In contrast, the Bethe-Heitler processes are not enhanced at high pair energies. They also possess a forward singularity that strongly favors

an asymmetric configuration with one energetic, forward electron or positron and the other constituent of the pair much softer [1]. Fig. 4.3 shows the electron vs. positron momenta for the A' signal events (red crosses) and Bethe-Heitler background events (black circles). The signal e^+e^- pairs are concentrated in the region where $E(e^+) + E(e^-) \approx E_0$. Bethe-Heitler background rejection is optimized when the two spectrometers have equal angles and momentum acceptances equal to half the beam energy. This acceptance window is shown by the blue box in Fig. 4.3.

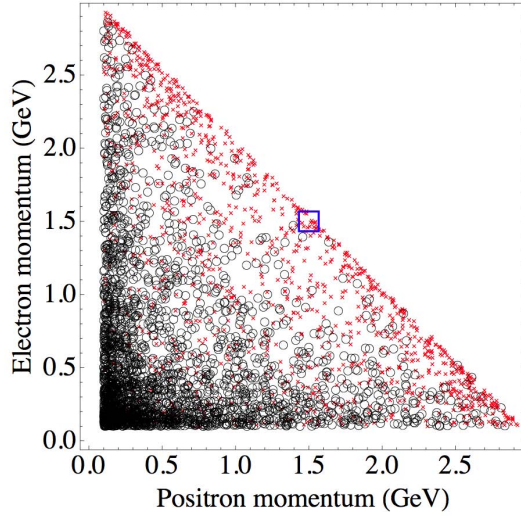


FIG. 4.3: Electron momentum vs. positron momentum for A' signal events with $m_{A'} = 200$ MeV (red crosses) and for Bethe-Heitler background events (black circles) using a 3 GeV beam [20]. The blue box shows a spectrometer acceptance window that optimizes signal sensitivity.

Calculation of the ϵ reach

To set a limit on the coupling α' we use a ratio method that normalizes A' production to the measured QED trident background rate. This method will set a limit on ϵ^2 , or $\alpha'/\alpha_{\text{fs}}$, while minimizing the systematic uncertainty from acceptance

and trigger efficiencies [17]. A' production is simply related to radiative production through Eq. 4.9. The ratio f of the radiative-only cross section to the full trident cross section can be reliably computed using MadGraph and MadEvent. The results of the simulations show that f varies linearly from 0.21 to 0.25 across the APEX mass range with an uncertainty of 0.01. This uncertainty dominates over the Monte Carlo statistical uncertainty and possible next-to-leading order QED effects [17]. By scaling the radiative cross section in Eq. 4.9 by f we compute the upper limit on $\alpha'/\alpha_{\text{fs}}$ using

$$\left(\frac{\alpha'}{\alpha_{\text{fs}}}\right)_{\text{max}} = \left(\frac{S/m_{A'}}{f\dot{B}/\delta m}\right) \times \left(\frac{2N_{\text{eff}}\alpha_{\text{fs}}}{3\pi}\right). \quad (4.10)$$

To calculate the $\alpha'/\alpha_{\text{fs}}$ reach of the proposed experiment we first calculate the rates of all reactions entering into the spectrometer acceptance by integrating over the target profile used in each kinematic setting (see Table 4.1). Trident rates were calculated as a function of invariant mass. An estimate of the mass resolution δm obtainable for APEX is calculated, and the bin size of the invariant mass acceptance region is set to $2.5 \times \delta m$. The total number of signal events S is calculated using Eq. 4.7, and the number of background events is calculated using $S/\sqrt{B} = 2$. The resulting limit for the full experiment is shown in Fig. 4.4.

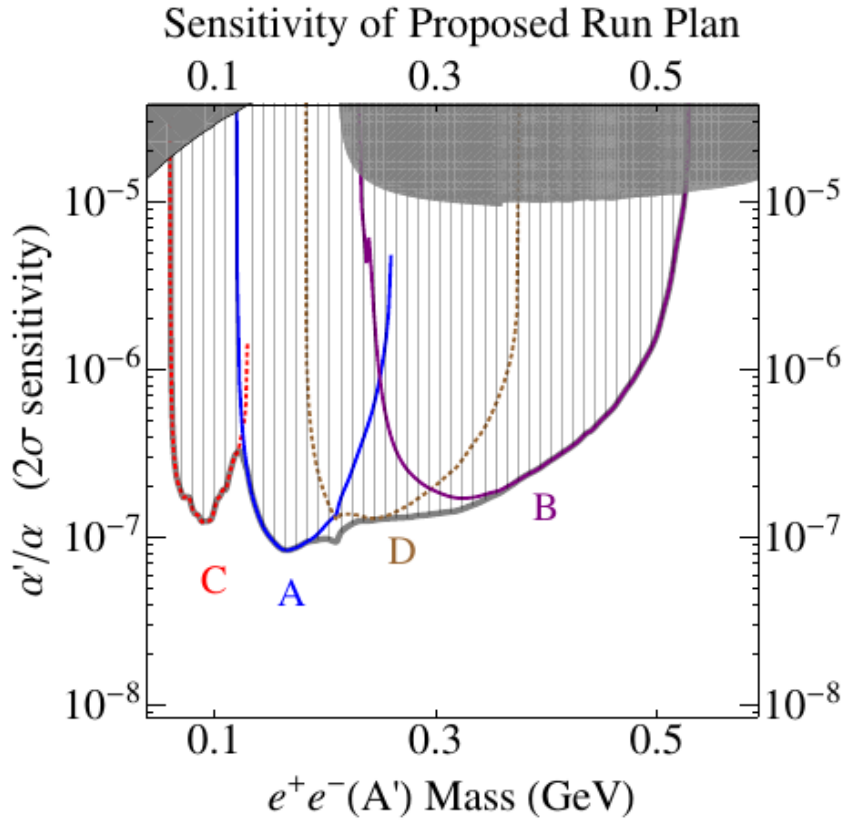


FIG. 4.4: Anticipated 2σ sensitivity for each of the individual energy settings of the proposed run plan [20]. The different energy settings are: A - 2.2 GeV, B - 4.4 GeV, C - 1.1 GeV, and D - 3.3 GeV. The grey curve reflects the sensitivity of a combined analysis.

4.3 Accidentals and rates

The final APEX production data will be comprised of coincidences between the two spectrometers, many of which are accidental coincidence events. A coincidence trigger is produced when both spectrometers detect a good event within the defined coincidence timing window. A true coincidence occurs when an e^+e^- pair is produced and both constituents are detected in coincidence. An accidental coincidence occurs when the two particles that produce the coincidence trigger do not come from an e^+e^- pair. The accidental coincidences will mainly consist of accidental e^+e^- and true $e^-\pi^+$ events.

The rate of accidentals can be estimated from the singles rate in each HRS and the duration of the timing window:

$$N_{\text{accidentals}} \simeq \sigma N_{\text{Left}} N_{\text{Right}} \quad (4.11)$$

where $N_{\text{accidentals}}$ is the rate of accidentals, N_{Left} and N_{Right} are the singles rates of each HRS, and σ is the size of the timing window. This means that $N_{\text{accidentals}}$ scales with the square of the total coincidence trigger rate.

At small angles, the main contributions to the counting rate in the spectrometers are due to electrons, pions, and protons scattering into the HRS acceptance. Table 4.1 summarizes the expected singles rates for each proposed kinematic setting. Kinematic settings A, B, and D will use a target that provides uniform coverage in scattering angles ranging from 4.5° to 5.5° . Kinematic setting C will have the tar-

get material concentrated at the ends of the angular acceptance so that the effective angles are 4.5° and 5.5° , with three times more material at the downstream end (4.5°) than at the upstream end (5.5°).

The table also includes the projected trigger rates. These rates assume a 20 ns coincidence timing gate and an online π^+ rejection of 30 by including the Right-HRS gas Cherenkov counter in the trigger. The observed trigger rates will have contributions from trident processes, the “two-step” trident process, and accidentals. The “two-step” trident process occurs when an electron radiates a real, hard photon in the target that converts to a high-mass e^+e^- pair. For thin targets it is suppressed compared to the trident rates, so it is sub-dominant for all kinematic settings. The accidental coincidence rates are dominated by e^+e^- accidentals, but π^\pm contributions are also included. The calculation of the accidental rates assumes that π^+ and π^- will be rejected offline by a factor of 100 and 3, respectively. It also assumes a 2 ns wide cut on the coincidence timing spectrum and an additional factor of four rejection from correcting on the target vertex. These rejection factors are quite conservative, and further rejection can be expected by exploiting kinematics (e.g. $E_{e^+} + E_{e^-} \leq E_0$).

The rates given in the table have been checked against measurements made by experiment E03-012 [20]. This experiment used a 5 GeV electron beam incident on a hydrogen target with the HRS positioned 6° relative to the beam and an HRS momentum setting of 2 GeV. The rates were also checked with the APEX test run data (see Sec. 7.7).

4.4 Experimental Setup

High-intensity fixed-target beams and high precision spectrometers are ideally suited to search for a new A' particle. The A' production rate, the luminosity, and the mass resolution attainable at Jefferson Lab vastly exceed what is available using colliding electron beam facilities. The APEX experiment will use Jefferson Lab's Continuous Electron Beam Accelerator Facility (CEBAF) and the High Resolution Spectrometers (HRS) in Hall A to search for the A' . The proposed experiment will probe couplings $\alpha'/\alpha \gtrsim 10^{-7}$ and masses $m_{A'} \sim 50 - 550$ MeV.

The experiment will study e^+e^- production off an electron beam incident on a tungsten target as illustrated in Fig. 4.5. The two HRSs will be used to detect the e^+e^- pairs and measure their invariant mass. Electrons will be detected in the Left-HRS and positrons will be detected in the Right-HRS. The invariant mass spectrum will be scanned for a narrow peak with a width corresponding to the instrumental resolution. The relative mass resolution will be 0.5%, limited by multiple scattering in the target material, track measurement errors by the HRS detectors, and imperfections in the magnetic optics reconstruction matrix (see Sec. 7.6).

Dipole septum magnets between the target and the HRS aperture will allow the detection of e^- and e^+ at angles of 5° relative to the incident beam. An elongated target with ten tungsten ribbons spaced along the beam line will increase the mass coverage by providing a variation of $\pm 0.5^\circ$ in the scattering angle. The e^+e^- pairs will be detected in coincidence within a timing window of 20 ns. The rejection of pion backgrounds will be done online using the Right-HRS gas Cherenkov detector.

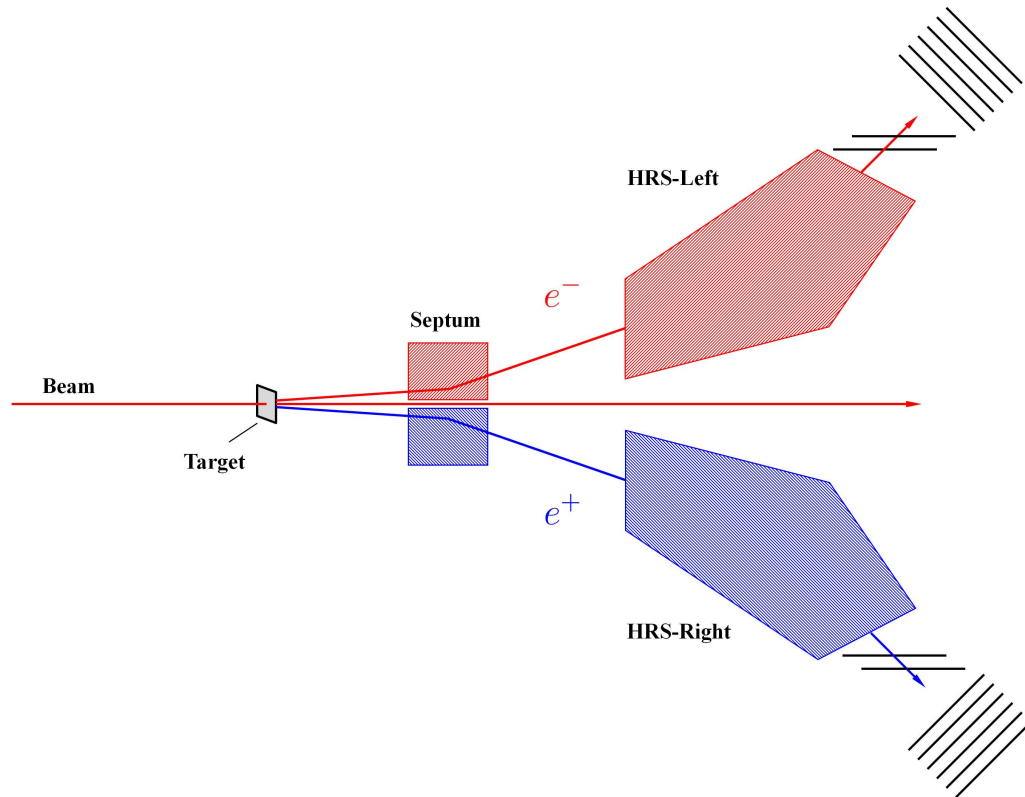


FIG. 4.5: The layout of the experimental setup. The experiment will study e^+e^- pairs produced off an electron beam incident on a high- Z target. The septum magnets allow detection of e^- and e^+ at angles of 5° relative to the incident beam. The HRSs will be used to detect the e^- and e^+ .

4.4.1 Target

There are several factors that need to be considered when designing the target to be used for production data taking. We want to maximize the production rate of e^+e^- pairs while also attaining the best mass resolution possible. To achieve this, we need to minimize multiple scattering of e^- and e^+ in the target and also have enough material to get a sufficient production rate. The target must be made of a high Z material in order to maximize the bremsstrahlung to pion production ratio. The stability of the target material at high temperatures also needs to be considered in the design. Finally, using a target elongated along the beamline would provide a wide and uniform mass coverage [20].

The final design of the target contains three sections: a production section (bottom) used for production data taking, a beam-target alignment section (middle) used for aligning the target components with the beam, and an optics section (top) used to perform the optics calibration along the entire length of the target. A drawing of the target is shown in Fig. 4.6.

The production section of the target consists of 10 ribbons of tungsten, each with a thickness of $15\ \mu\text{m}$ (0.43% radiation lengths). The ribbons are 2.5 mm wide and spaced 5.5 cm apart along the beamline. The e^+e^- pairs produced within the acceptance of the spectrometers miss all downstream material, so only one ribbon contributes to multiple scattering in the target. Using 10 targets separated along the beam line provides a variation of 1° in the scattering angle, which increases the $m_{A'}$ coverage by 50% [31].

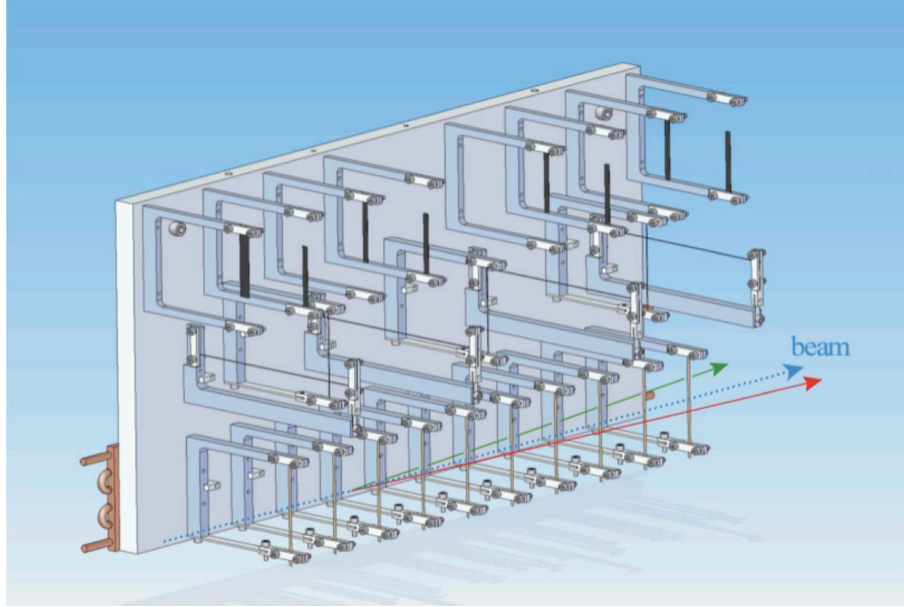


FIG. 4.6: Final design of the APEX target. The target is split into three sections: production section at the bottom, beam-target alignment section in the middle, and optics section at the top.

The alignment section (middle) consists of 4 horizontal and 3 vertical tungsten foils, each $100\mu\text{m}$ in diameter. The horizontal wires are arranged in 5 mm vertical steps and are located along the beam line at -25, -10, 10, and 25 cm. The vertical wires are arranged in 2.5 mm horizontal steps and are located along the beam line at -20, 0, and 20 cm. The alignment target system has been surveyed relative to the full target system, so the beam direction relative to the alignment section will provide alignment calibration for the entire APEX target system.

The optics calibration section (top) consists of 8 carbon foils providing calibration points along the full length of the target system. The foils are arranged so that the beam can pass through either 4 or 8 foils at a time in order to provide an initial calibration with either 7 or 14 cm spacing along the beam line.

For an electron beam of $80\ \mu\text{A}$ incident on a $10\% X_0$ tungsten target, the

maximum heat load is about 140 W. The APEX target system includes 4 Lytron CP15 cold plates installed on the back of the primary aluminum mounting plate. All target holders are made of aluminum so that heat is efficiently conducted into the aluminum mounting plate (over 1 cm thick). By supplying the cooling plates with nitrogen gas, a heat removal of up to 200 W is achievable [20].

4.4.2 Septum Magnet

The radiated A' 's travel forward at very small angles. The opening angle of the A' 's decay products is also small. The two High Resolution Spectrometers used to detect the decay products can pivot freely around the center of Hall A; however, they can only rotate to a minimum angle of 12.5° with respect to the beamline. In order to detect e^+e^- pairs at small angles, room temperature dipole septum magnets are installed between the target and the spectrometers. The septum magnets bend particles scattered at angles as small as 5° relative to the incident beam so that their trajectories overlap the trajectories detectable by the HRSs. Section 5.2.2 describes how the septum magnets were used during the test run.

4.4.3 Track Measurement

Good particle tracking is essential for precise reconstruction of a particle's momentum vector at the target. Two vertical drift chambers (VDCs) in each spectrometer are used for the measurement of the track's coordinates and direction in the focal plane (see Sec. 3.2.3). The VDCs have a spatial resolution $\sigma_{x,y} \approx 100 \mu\text{m}$

and an angular resolution $\sigma_{\theta,\phi} \approx 0.5$ mrad.

APEX will experience detector rates of up to 5 MHz in the VDCs. Operation of the HRS tracking at a rate higher than 100 kHz is uncommon. However, by modifying the detector electronics, using the VDC at a maximum track rate of 5-6 MHz can be justified. A track rate of 30-50 kHz of elastic scattering events from a ^{12}C target was used during many HRS optics calibrations. This rate of elastic events corresponds to a track density of ~ 10 kHz per cm of the chamber length [20]. The total length of the chamber is 2 m, so operation of the HRS tracking should be possible at a rate of 2 MHz for the whole chamber under standard operational voltage.

The VDC read-out system uses amplifier/discriminator (A/D) cards to read out the wire signals. Previously, LeCroy 2475 type cards were used in the VDCs. These cards require a minimum threshold of $5\mu\text{A}$, which requires a working high voltage of -4 kV for the VDCs. This limits the maximum rate for stable operation of the HRS tracking. One way to improve the high rate capability of the VDCs is to reduce the gain and increase the corresponding sensitivity of the A/D cards. New A/D cards were developed by JLab's Electronics Group to increase the signal sensitivity by a factor of five [32]. This directly translates to an additional factor of five in rate capability, which brings the VDC rate limit to 10 MHz for the whole chamber.

The VDC has a maximum drift time of 350 ns, which corresponds to 1.75 accidental tracks per event at 5 MHz. However, the timing of such accidental tracks

will not match the timing of the trigger. Tracks of real coincidence events will reside within a 20 ns timing window, and tracks outside this window will be rejected. Applying this timing condition will reduce the number of accidental tracks by a factor of 10, or 0.2 accidentals per event at 5 MHz. Because this reduction is independent for each VDC, the probability of an accidental track being reconstructed in both VDCs will be at most 5%. In these remaining 5% of events, the real track will be determined using the fact that its trajectory intersects the proper scintillator paddle of the 16 paddle S2m trigger plane (see Sec. 5.3). As a result, the probability of a false track drops below 0.5% [20].

4.4.4 SciFi Detector

The sensitivity of our A' search depends critically on precise reconstruction of the invariant mass of e^+e^- pairs. The HRS has an excellent relative momentum resolution of $\mathcal{O}(10^{-4})$, so the mass resolution is dominated by the angular resolution of the spectrometers.

The track reconstruction of the spectrometers is normally calibrated using the sieve slit method. The sieve slit is a 5 mm thick tungsten plate with a grid of holes drilled through it. It is positioned between the target and the entrance of the spectrometer during optics calibration runs. Electrons scatter off a target and travel toward the sieve slit. The tungsten plates are thick enough so that electrons incident on the plate never enter the acceptance of the spectrometer. Thus, only electrons whose trajectories pass through the holes of the sieve slit enter into the

spectrometer. Their tracks are reconstructed back to the sieve plane and their positions at the sieve plane are compared with the surveyed hole locations. By analyzing the deviations between the reconstructed and surveyed hole positions, one can optimize the coefficients used to reconstruct the particle trajectories (see Sec. 6.3).

The sieve slit method works well only when the HRS has a negative polarity. To perform the optics calibration with positive polarity, positrons are produced via pair production off the electron beam incident on the target. Positrons with momentum equal to that of the HRS momentum setting travel toward the sieve plate located at the entrance of the spectrometer. Positrons incident on the sieve plate never enter the HRS acceptance, so only positrons traveling through the sieve holes enter into the spectrometer. However, there is a high rate of electrons scattering from the target that are also incident on the sieve plate. These electrons then pair produce in the sieve plate and create many positrons with momentum equal to that of the HRS momentum setting. The result is a flood of positrons entering into the spectrometer, making the sieve holes impossible to distinguish.

A scintillating fiber detector (SciFi) was designed to allow optics calibration of the HRS with both negative and positive polarity. The SciFi detector will also provide a more thorough calibration over the full spectrometer acceptance. A drawing of the detector is shown in Fig. 4.7. It will be located in the target chamber approximately one meter downstream of the target and immediately upstream of the septum magnet.

The active area of the detector is $8.8 \text{ cm} \times 10.3 \text{ cm}$ and consists of two orthogonal planes of 32 scintillating fibers with a 1 mm diameter. The active area is mounted to a mechanical arm coupled with a stepper motor, allowing the detector to be precisely positioned inside of the vacuum chamber. The scintillator fibers are optically coupled to clear 1.5 mm diameter optical fibers that transport the scintillation light to a Hamamatsu 64 channel multi-anode photomultiplier tube (maPMT). The optical fibers are necessary to locate the PMT assembly away from the intense magnetic field and radiation surrounding the beamline. The PMT assembly is a Faraday cage containing the maPMT and four 16 channel amplifier/discriminator cards.

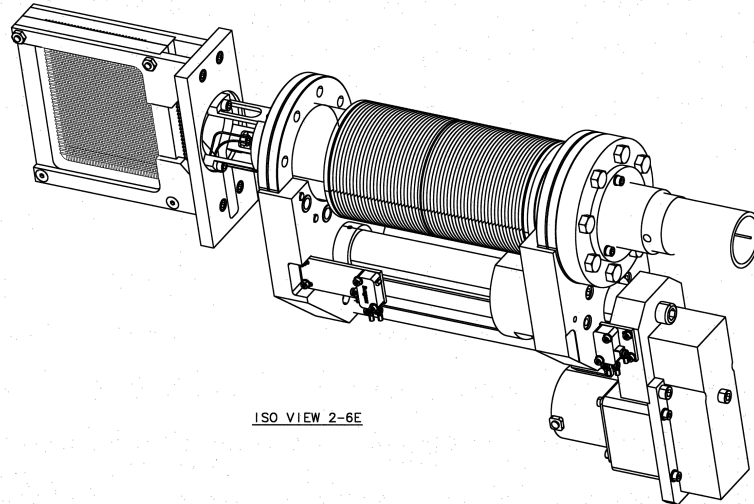


FIG. 4.7: Drawing of the scintillating fiber (SciFi) detector. The SciFi detector will be used for optics calibration of the spectrometers during APEX.

Two SciFi detectors (one for each spectrometer) are being built for APEX. One

detector has been fully assembled and is currently being tested. Preliminary results demonstrate a ~ 7 photoelectron yield per fiber. Both detectors will be completely assembled and commissioned well before the start of the experiment.

4.4.5 Particle Identification

The HRSs are able to detect various types of particles, but APEX is only interested in detecting electrons and positrons. The HRS spectrometer detector packages are equipped with gas Cherenkov counters and two-layer lead-glass calorimeters for identification of electrons and positrons (see Sec. 3.2.3). Under the APEX configuration settings, the highest projected ratio of rates for e^+/π^+ is $\sim 1/340$ (see Sec. 4.1). Therefore, the production data sample is especially susceptible to π^+ contamination. The gas Cherenkov counter of the Right-HRS will be used as part of the coincidence trigger to provide online π^+ rejection. This will provide a π^+ rejection factor of ~ 100 for true coincidence events. The combined pion rejection factor using both the gas Cherenkov counter and the calorimeter in the offline analysis is at least as high as 10^4 [20].

4.4.6 Trigger and DAQ

Trigger

Triggers are signals responsible for prompting the DAQ system to start reading out detector information. A trigger signal can be produced when a particle hits a detector or a combination of detectors. The trigger configuration is set up so

that detector information is read out only for events of interest. After triggers are created, they are sent to the Trigger Supervisor (TS). The TS decides which trigger to accept according to user-defined pre-scale factors (see Sec. 3.2.4).

The APEX experiment is interested in detecting e^- and e^+ coincidence events. To select these events, the main trigger will consist of a coincidence between the S2m scintillator planes of both HRSs, and the gas Cherenkov counter of the Right-HRS. The gas Cherenkov counter is used to provide online pion rejection. A 20 ns wide signal is formed when there is a hit in one of the sixteen paddles of either S2m plane. A 10 ns wide signal is formed when the Right-HRS gas Cherenkov counter sees a valid signal. When these three signals overlap (Fig. 4.8), the main trigger is formed and detector information is read out to the DAQ system. The triple coincidence of these three signals forms a 40 ns coincidence timing window.

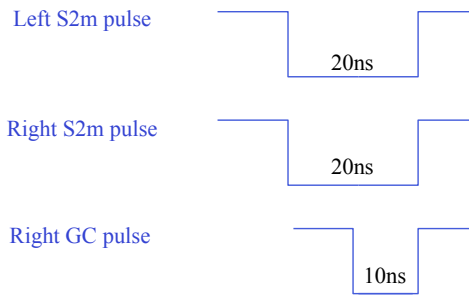


FIG. 4.8: Main coincidence trigger. When pulses from the left S2m plane (20 ns), right S2m plane (20 ns), and right gas Cherenkov (10 ns) overlap, a trigger signal is formed. The overlap of these three pulses creates a 40 ns coincidence timing window.

Sparsification

During the experiment, the spectrometers will experience high detector rates of up to 5 MHz. As a result, the VDCs will read out a large rate of background hits, leading to a significant increase in DAQ dead time.

The VDC signals travel from amplifier discriminator cards to LeCroy 1877S TDCs. These TDCs will operate in common stop mode. When operating in common stop mode, the TDC sees a stop pulse from the Level-1 Accept trigger signal and records all start pulses that occurred within a programmable full scale time window (see Fig. 4.9). There is a considerable delay between the start and stop pulses, so the full scale time window needs to be long enough to record the signals of interest. As a result, many background hits that occur close to the stop pulse are also recorded.

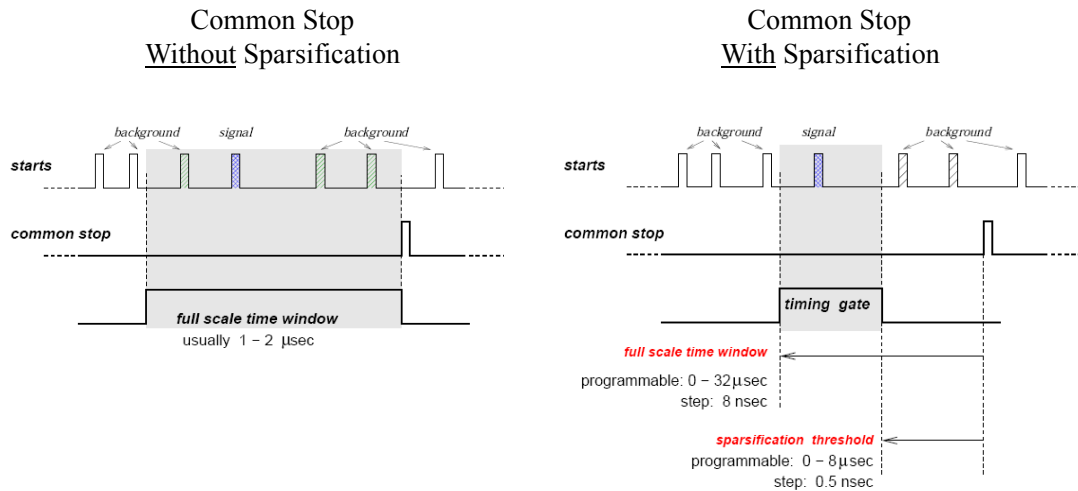


FIG. 4.9: A timing diagram for the 1877S TDC running in common stop mode [33]. Without sparsification, background signals near the stop pulse are recorded. When operating in sparsification mode, these background signals can be ignored.

Fortunately, the 1877S TDCs can run in sparsification mode. In sparsification

mode, start pulses are only recorded if they occur after the edge of the full scale time window and before the programmed sparsification threshold (see Fig. 4.9). Background pulses that occur close to the stop pulse are thus disregarded.

4.5 Proposed Measurement

The APEX experiment will run after the CEBAF 12 GeV upgrade is complete. The experiment will use a beam energy of 1.1 GeV for 6 days, 2.2 GeV for 6 days, 3.3 GeV for 6 days, and 4.4 GeV for 12 days. We expect to collect true coincidence e^+e^- events with a rate in the range of 100-500 Hz, providing $O(1)$ A' signal events per minute at the threshold of sensitivity. The total e^+e^- sample size will exceed 10^8 pairs in a 6-day period for each setting [20].

As shown in Fig. 2.5, the proposed experiment will be sensitive to A' 's with couplings as small as $\alpha'/\alpha \sim (6-8) \times 10^{-8}$ for masses in the range 65-300 MeV, and couplings as small as $\alpha'/\alpha \sim 2 \times 10^{-7}$ for larger $m_{A'} \lesssim 525$ MeV. This is a factor of $\sim 3-35$ times lower in ϵ than existing constraints, and corresponds to $\sim 10-1000$ times smaller cross-sections [20].

TABLE 4.1: Singles rates, trigger rates, and coincidence rates (including both true coincidences and accidentals that can not be rejected offline) predicted for the full APEX run.

Settings	A	B	C	D
Beam energy (GeV)	2.2	4.4	1.1	3.3
Beam current (μA)	70	60	50	80
Effective angles	4.5-5.5	4.5-5.5	4.5-5.5	4.5-5.5
Target T/X_0 (ratio ^a)	4%	8%	0.7% (1:3)	8%
Central momentum of the spectrometers (GeV)	1.095	2.189	0.545	1.634
Singles (negative polarity)				
e^- (MHz)	4.1	0.7	4.5	2.2
π^- (MHz)	0.1	1.7	0.025	0.9
Singles (positive polarity)				
e^+ (kHz)	27	5	18	17
$\pi^+ + p$ (kHz)	90	1700	25	900
Trigger^b/DAQ (kHz)	3.0	3.1	2.0	3.3
Coincidence backgrounds:				
Tridents: $e^-Z \rightarrow e^-e^+e^-Z$ (Hz)	500	110	260	370
“Two-step” tridents (Hz)	30	16	3	45
Accidentals ^c (Hz)	55	30	40	40

^aThe A, B, and D settings all use targets that provide uniform coverage in effective scattering angles from 4.5° to 5.5° . Setting C uses a target that is concentrated at the edges of the angular acceptance, so that the effective angles are 4.5° and 5.5° , with three times more target material at the downstream end (5.5°) than the upstream end (4.5°).

^bThe trigger rate assumes a 20 ns time window and a π^+ rejection factor of 30 by including the Right-HRS gas Cherenkov counter in the trigger.

^cAssumes offline π^+ rejection by a factor of 100, π^- rejection by a factor of 3, a 2 ns true coincidence time window, and an additional factor of four rejection from correcting on the target vertex.

5

The APEX Test Run

The APEX experiment held a test run at Jefferson Lab in experimental Hall A in the summer of 2010. The purpose of the test run was to address specific PAC concerns about the experiment's proposal and to collect enough statistics to search for the A' within a significant region of parameter space.

The A' search was performed by studying e^+e^- production off an electron beam incident on a tantalum foil target of thickness 22 mg/cm^2 . The test run used a $2.260 \pm 0.002 \text{ GeV}$ electron beam with a current up to $150 \mu\text{A}$. The central momentum of the HRSs was set to $\simeq 1.131 \text{ GeV}$. Dipole septum magnets allowed the detection of e^- and e^+ at angles of 5° relative to the incident beam.

5.1 PAC Concerns

APEX received conditional approval from the Program Advisory Commity (PAC) in January of 2010. We were asked to demonstrate needed performance in a two week test run. The PAC gave seven conditions that needed to be addressed in the test run [34]:

1. *Run with the zig-zag mesh design of the tungsten target and prove that it allows the requested vertex resolution.*
2. *Prove that it is possible to reach the uncertainty of 0.1 mrad in determining the central scattering angle between the two spectrometers.*
3. *Prove that the vertical drift chambers (VDCs) can operate at a rate higher than 20 kHz/wire (That, according to the TAC report, is the maximum Hall A has operated until now).*
4. *Prove that it is possible to use the gas Cherenkov counters in the trigger to help clean pions. In fact, the TAC report claims that this is not possible with total rates/PMT at the level of a few hundred Hz to MHz. Also, prove that the off-line rejection of 10,000:1 can be achieved.*
5. *Prove that 20 ns (S0-S0) and 40 ns (S0-S0-C) can be achieved.*
6. *If it is possible (not obvious for a test run), it will be advisable to*

set the septum magnets at higher fields to prove that also at energies higher than 2 GeV it is possible to reach the uniformity of the field requested from the experiment.

- 7. Provide a detailed description of different contributions to background and their importance (how assumptions and/or approximations can influence the predictions) and comparison with measurement.*

5.2 Experimental Setup

The APEX test run took place in Hall A from June 21st, 2010 to July 12th, 2010. While it was originally scheduled only for a two week period, it was extended by a further week.

The first week was spent removing equipment from the previous experiment (PREX) and installing the Left-HRS detector components. The detectors were commissioned using cosmic rays and low beam currents. The first optics data was collected, and high rate data was collected using a lead/diamond target.

During the second week the Right-HRS detector components were installed. The coincidence trigger electronics were installed and the DAQ was tested. After commissioning the Right-HRS detectors and setting up the coincidence triggers, production data was collected that included e^+e^- coincident events. Also, the VDCs were tested at rates up to 8 MHz (single arm).

The third week was crucial to the success of the test run. A sizeable amount of high quality optics data was collected for both spectrometers. Most of the week was spent collecting production data. Having this extra week enabled us to collect four million events that passed our coincidence trigger. Collecting this large data sample allowed us to search for an A' within a significant region of phase space and obtain a publishable result.

5.2.1 Targets

A production target was constructed and delivered to Jefferson Lab to be used in the test run. Due to a lack of technical manpower and high radiation levels, however, the target was never installed. Instead, a single tantalum foil of thickness 22 mg/cm^2 was used for production data taking.

To test the high rate performance of the HRS detectors, a lead/diamond target was used (Fig. 5.1). This target was designed for the PREX experiment [35]. It consists of a 0.5 mm foil of lead sandwiched between two 0.2 mm sheets of diamond.

5.2.2 Septum and Beam Steering Magnets

The HRSs can rotate to a minimum angle of 12.5° with respect to the beam-line. To detect e^+e^- pairs at a scattering angle of 5° , room temperature dipole septum magnets were installed between the target and opening of the spectrometers (Fig. 5.2). These septum magnets were originally designed for the PREX experiment [35].

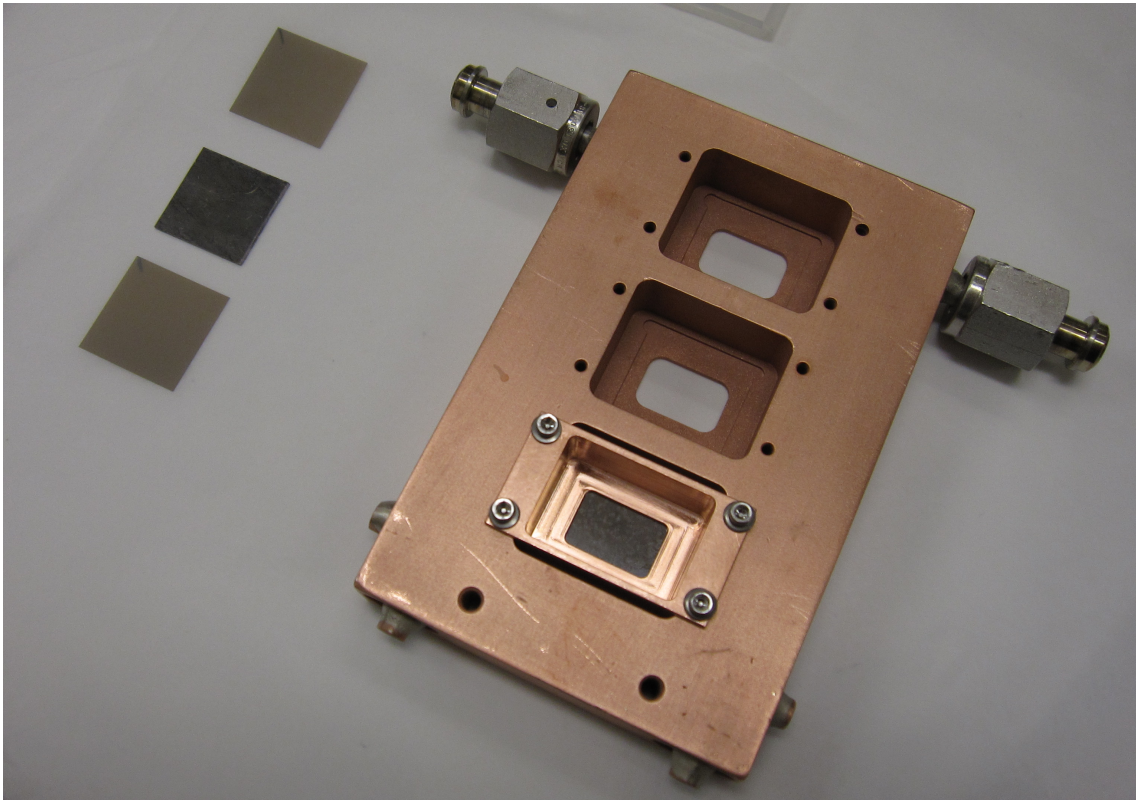


FIG. 5.1: The lead/diamond target used for high rate data taking.

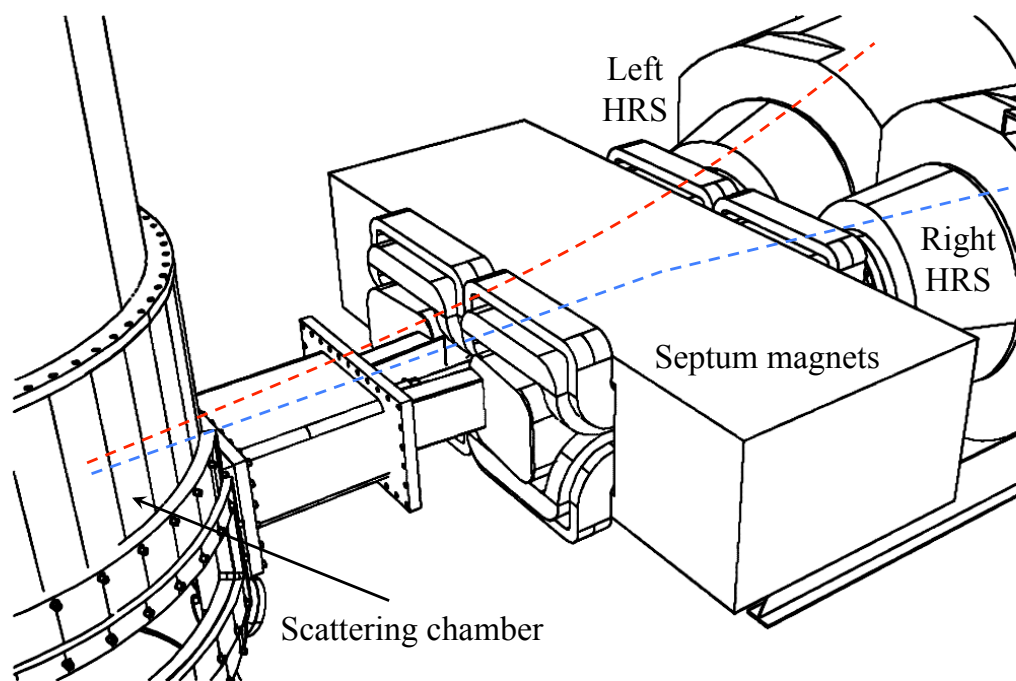


FIG. 5.2: The dipole septum magnets allow detection of e^- and e^+ at angles of 5° relative to the incident beam.

During the test run, the polarity of the septum magnets was set to bend electrons toward the left spectrometer and positrons toward the right spectrometer. As the electron beam passed downstream of the target, the septum magnets would bend its trajectory toward the left spectrometer. Three additional magnets were installed onto the beam line to correct the beam's trajectory back to the beam dump. Two were installed upstream of the target, and the third was installed downstream. The two that were installed upstream of the target had to be taken into account when calculating the beam position at the target.

5.2.3 Electronics and Trigger

The design of the front end electronics is driven primarily by the need to operate accurately at rates up to 5 MHz. The electronics system was comprised of NIM electronics, VME scalers, and FastBus Analog-to-Digital converters (ADCs) and Time-to-Digital converters (TDCs). To improve the high rate capabilities of the detectors, efforts were made to lower PMT high voltages and shorten the logic pulse widths. The PMT voltages for the gas Cherenkov detectors were adjusted so that their average single photoelectron pulse had an amplitude of 5 mV. The length of the logic pulses used for the digital electronics was kept to 10 ns.

To improve the high rate capability of the VDCs, new amplifier/discriminator cards were used in the VDC read-out system. These cards were designed by JLab's Electronics Group to reduce the signal threshold and allow operation of the VDCs at smaller gains (see Sec. 4.4.3). With these cards installed, a high voltage of -3.5

kV was supplied to the VDCs instead of the nominal -4 kV.

Trigger

The APEX test run used seven different triggers, labeled T1-T6 and T8. T1 and T3 were a logical OR of the 16 PMTs on the right side of the S2m plane in the left and right spectrometers, respectively. T2 was taken from the top PMT of the S0 counter in the left HRS. T5 was based on a 40 ns coincidence window from the left HRS S0 and gas Cherenkov detectors.

T4 and T6 were used to record coincidences between the left and right spectrometers. T4 corresponded to a coincidence between the left and right S2m planes, and T6 to a coincidence between T4 and the gas Cherenkov detector in the right HRS (used to detect positrons). The gas Cherenkov detector in T6 was used to remove the pion background. T8 was a 1024 Hz clock used to normalize rates recorded in the scalers.

Table 5.1 summarizes the triggers used. Fig. 5.3 shows a schematic of the logic used to construct the trigger electronics. Most of the trigger components reside on the left HRS due to the location of the trigger supervisor. This ensured that the delay of the cables and distortion of the pulses were minimized.

TABLE 5.1: Triggers of the APEX test run.

T1	LHRS S2m
T2	LHRS S0
T3	RHRS S2m
T4	LHRS S2m AND RHRS S2m
T5	LHRS S0 AND LHRS gas Cherenkov
T6	T4 AND RHRS gas Cherenkov

6

Detector Calibrations

The detectors used in any experiment must be calibrated in order to make accurate measurements. This chapter will cover the detector calibrations performed during the APEX test run.

Determining the invariant mass of e^+e^- pairs requires a careful understanding of the reconstructed beam position at the target, as well as the reconstruction of the e^- and e^+ trajectories inside the spectrometers. Due to the high luminosity of APEX, additional considerations must be made when calibrating the detectors to ensure accurate detector and data acquisition performance at high rates. In this chapter we will discuss the calibration of the BPMs and HRS detectors used during the test run. We will also examine the magnetic optics calibration of the HRSs that allows us to achieve precise track reconstruction.

6.1 HRS Detectors

6.1.1 Scintillators

The S2m scintillator planes were used for timing and trigger purposes during the APEX test run. Both S2m planes were used along with the Right-HRS gas Cherenkov counter for the final coincidence trigger to select true e^+e^- pairs. Because of the high rates experienced by the detectors during the experiment, it was important to use a small coincidence timing gate in order to avoid recording an excess of accidental coincidence events. To achieve a small enough timing gate, the timing of the PMT signals must be aligned in each scintillator plane.

A logical OR between the left PMTs of each S2m plane was used as part of the coincidence trigger. Therefore, it was only necessary to align the timing of the left PMTs of each plane. LeCroy 1877 TDCs were used to measure the timing of the PMT signals. These TDCs have 0.5 ns resolution and were operated in common stop mode. To align the timing of the PMTs, electrons were scattered off a lead/diamond target in order to provide sufficient statistics. The S0 scintillator counter was used as a timing reference, and 1-5 ns delay cables were inserted to adjust the timing of each PMT. Fig. 6.1 demonstrates an example of the timing spread that was achieved during the test run.

The amount of charge in a PMT signal produced for a fixed amount of light depends on the gain of the PMT. The gain can be controlled by adjusting the high-voltage (HV) supplied to the PMT. The HV supplied to the S2m PMTs must be

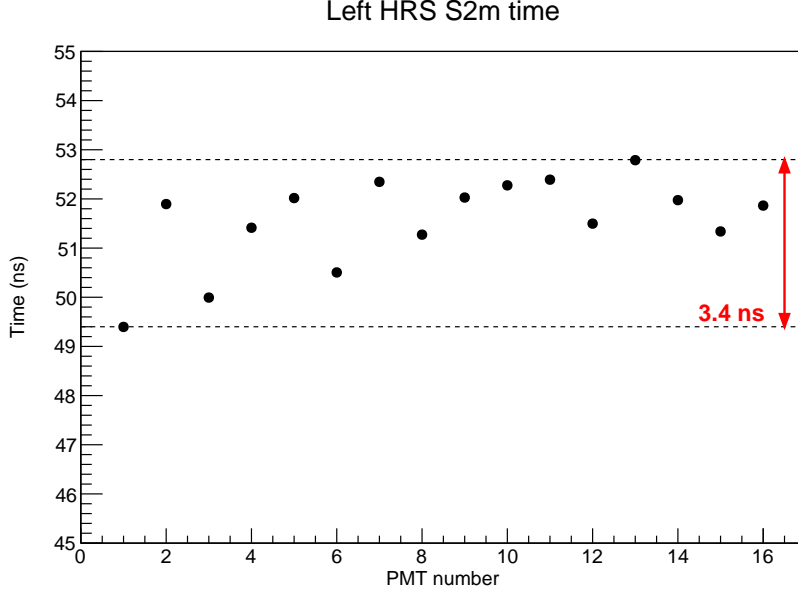


FIG. 6.1: The average timing of the PMT signals for the Left-HRS S2m plane after inserting 1-5 ns delay cables. The S0 counter was used as a reference. A timing spread of ~ 3.5 ns was achieved.

adjusted so that gain of each PMT is the same. The gain matching was done using cosmic ray data. Events were selected from the center of the paddles using TDC information from the VDCs. The ADC distributions were plotted and the first photoelectron peaks were fit with a Gaussian for each PMT. The HV of each PMT was then adjusted using

$$HV_{new} = \sqrt[10]{\frac{20}{ADC_{peak} - ADC_{pedestal}}} \times HV_{old}, \quad (6.1)$$

where ADC_{peak} is the centroid of the Gaussian fit and $ADC_{pedestal}$ is the pedestal value. The pedestal represents the output of an ADC channel when there is no signal at its input. The pedestal acts as a starting point from which the ADC output starts counting. Thus, the pedestal must be subtracted from the raw ADC

value to obtain the true ADC readout corresponding to the size of the input signal. The pedestal locations vary for each channel, and need to be determined for each channel separately.

6.1.2 Gas Cherenkov Detector

The gas Cherenkov detector in the Right-HRS was used as part of the coincidence trigger to provide trigger-level π^+ rejection. Just as for the S2m scintillator planes, it was essential that all ten PMTs in the detector had the same timing and gain. The timing alignment and gain matching of the gas Cherenkov PMTs was done using the same procedures described in Sec. 6.1.1.

The ADC spectrum of the gas Cherenkov detector was used to select the final event sample, so a more detailed off-line ADC calibration was needed. The sum of the amplitudes of all ten PMT signals was used to separate the e^+ from meson background (see Sec. 7.2). Positrons were identified by making a cut above the sum of the first photoelectron peaks for all ten PMTs. Therefore, it was essential to align the first photoelectron peak of each PMT.

The first photoelectron peaks were aligned by applying amplitude transformation coefficients to the ADC spectrums. The first photo electron peaks were each fit with a Gaussian (as in Sec. 6.1.1), and the corrected ADC values were calculated using

$$A_i^{corr} = \frac{20}{ADC_{peak} - ADC_{pedestal}} \times A_i^{raw}, \quad (6.2)$$

where ADC_{peak} is the centroid of the Gaussian fit, $ADC_{pedestal}$ is the pedestal

value, and A_i^{raw} is the uncorrected ADC value. Fig. 6.2 shows the sum ADC spectrum before and after the correction.

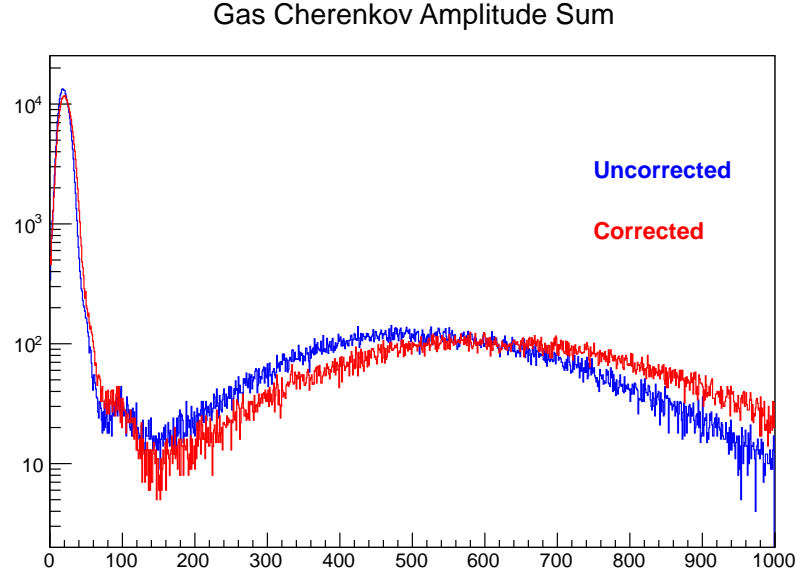


FIG. 6.2: The sum of all ten gas Cherenkov PMT amplitudes before and after off-line correction.

6.1.3 Drift Chambers

Time offsets

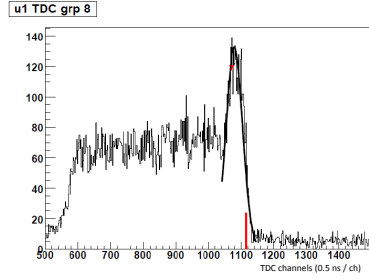
The vertical drift chambers are responsible for reconstructing the e^- and e^+ tracks inside the spectrometers. When a charged particle passes through the drift chamber it produces ionization. The resulting ions and electrons are accelerated by the electric field surrounding the nearest wire, producing an electric current on the wire. TDCs are used to measure the timing of the resulting signal relative to the timing of the trigger. The time it takes the ionization to drift to the wire is called the drift time, and can be extracted from the time measured by the TDC.

The readout time for each wire, i , can be expressed

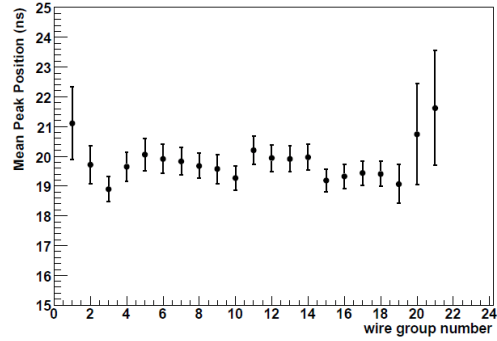
$$t_{\text{TDC}} = t_{\text{drift}} + t_{\text{delay},i} - t_{\text{path}} - t_{\text{trig}} \approx t_{\text{drift}} + t_{0,i} \quad (6.3)$$

where t_{drift} is the drift time, $t_{\text{delay},i}$ is the time it takes for the signal to travel to the TDC and is unique for each wire, t_{path} is the time it takes for the electron to travel from the drift chamber to the trigger detectors, and t_{trig} is the time it takes for the trigger to occur and be sent to the common stop of the TDC [36]. The last three terms can be grouped into a single offset, $t_{0,i}$.

The wire signals travel to amplifier/discriminator (A/D) cards before going to the input of the TDCs. Each A/D card takes signals from 16 wires and sends the output along a ribbon cable to the TDC. Because these 16 wires use the same A/D card and travel along the same length of ribbon cable, it is sufficient to determine a single time offset t_0 for the entire group of 16. An example of a typical VDC time spectrum is shown in Fig. 6.3a. Since the TDCs were operating in common stop mode, the histogram is backward in time. The peak on the right corresponds to the sudden movement of charged particles near the wire, whereas the rest of the spectrum corresponds to the movement of particles located farther from the wire. To calibrate the time offset of a group of wires, the peak is fit with a Gaussian and the offset is fixed at 1.4σ to the right of the peak position. Fig. 6.3b shows the time offset determined for each group of wires in one VDC.



(a)



(b)

FIG. 6.3: An example of a raw TDC spectrum for a group of 16 wires is shown in (a). The histogram is backward in time because the TDCs were operating in common stop mode. The peak towards the right corresponds to the sudden movement of charged particles near the wire. To determine the time offset t_0 , the peak is fit with a Gaussian and t_0 is fixed at 1.4σ to the right of the peak (red line). (b) compares t_0 for each group.

6.2 Beam Position

An accurate determination of the beam position at the target is essential for APEX. During the experiment the beam position needs to be monitored in order to ensure that it stays within the target area. If the beam strays outside of the target area it could damage the apparatus. Furthermore, a precise knowledge of the beam position at the target for every event is important for the optics calibration of the spectrometers.

Two beam position monitors (BPMs) located upstream of the target are used to determine the position of the beam. The BPM signals are read out by ADCs, the output of which can be related to position through a linear transformation. To perform this transformation one must determine the x and y position offsets and gain coefficients. These parameters are calibrated with respect to a set of wire

scanners located adjacent to the BPMs.

There is a difference of a few μs from the time when the particle hits the target and the time when the BPMs return the corresponding beam position [37]. Therefore, when using a rastered beam the BPMs alone are not sufficient for determining the beam position at the target for each event. To account for this, the current information of the two raster magnets is used in addition to the BPM information to determine the event-by-event on-target beam position. The beam position is calculated by

$$x_{tg}^{\text{raster}} = O_x + A_x I_x^{\text{raster}}, \quad y_{tg}^{\text{raster}} = O_y + A_y I_y^{\text{raster}}, \quad (6.4)$$

where O_x and O_y are the offset corrections, A_x and A_y are the transformation coefficients, and I_x^{raster} and I_y^{raster} are the currents in each of the raster magnets. The transformation coefficients are calculated from the widths of the BPM and current distributions (see Fig. 6.4):

$$A_x = \frac{\Delta x_{\text{BPM}}}{\Delta I_x^{\text{raster}}}, \quad A_y = \frac{\Delta y_{\text{BPM}}}{\Delta I_y^{\text{raster}}}. \quad (6.5)$$

The offsets are calculated by comparing the average beam position measured by the BPMs to the average reconstructed beam position from the raster current:

$$O_x = \bar{x}_{\text{BPM}} - \bar{I}_x^{\text{raster}} A_x, \quad O_y = \bar{y}_{\text{BPM}} - \bar{I}_y^{\text{raster}} A_y. \quad (6.6)$$

After all the parameters are calibrated they are stored in a database file that is used to create the corrected beam position variables.

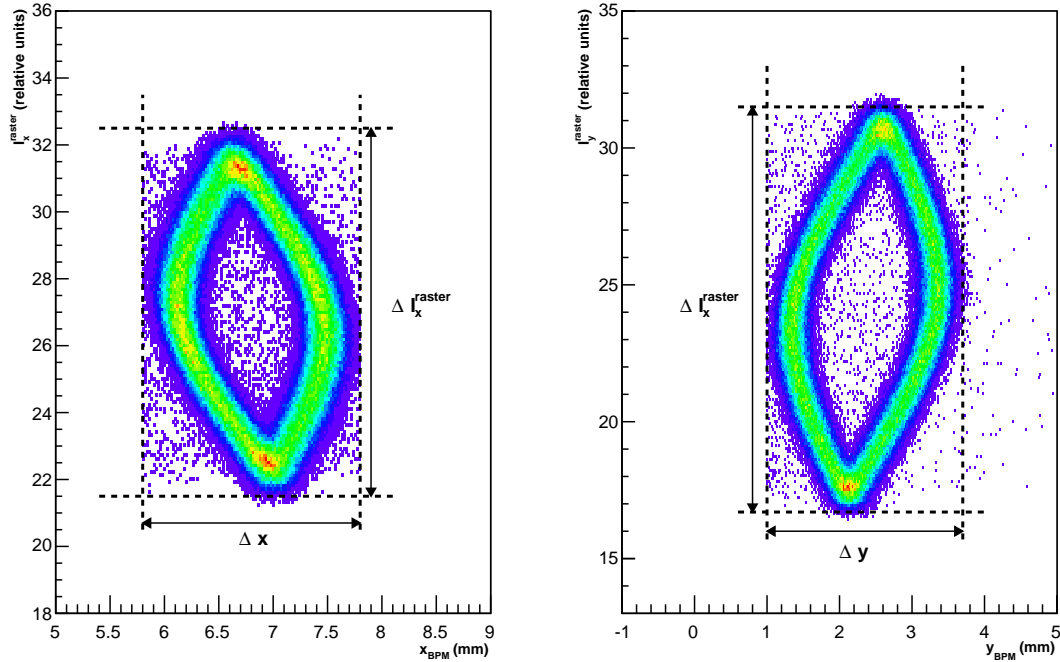


FIG. 6.4: The raster current vs. the horizontal beam position measured by the BPMs. The widths of the distributions are used to calculate the corrected beam position. Note the $\pi/2$ phase difference between the x and y plots.

Additional Beamline Magnets

The septum magnet was used to bend negatively charged particles toward the left-HRS and positively charged particles toward the Right-HRS. As the electron beam travels downstream of the target the septum magnet bends its trajectory towards the Left-HRS. Three additional magnets were installed onto the beam line to correct the beam's trajectory back to the beam dump. Two of the magnets were installed upstream of the target, so their bending effects must be taken into account

when determining the on-target beam position.

The bending of the beam can be calculated using the field integral of each magnet ($\int Bdl$), the momentum of the beam (p), and the distance from the magnet to the target (d):

$$\Delta x = d \times \theta = d \times \frac{\int Bdl}{p}. \quad (6.7)$$

The final beam position at the target was shifted toward the Left-HRS by 2.9 ± 0.2 mm due to the bending of the additional beam line magnets. This value was inserted into a database file used to create the variables for the final on-target beam position.

6.3 Optics Calibration

Reconstructing the invariant mass of e^+e^- pairs requires the precise determination of the position and angle of the particles at their reaction vertex. The focal plane coordinates of a detected particle are measured directly by the vertical drift chambers (VDCs). The spectrometer's optics matrix establishes a mapping between the focal plane coordinates and the interaction vertex. The optics matrix elements must be calibrated to provide an accurate and precise measurement of the vertex of the e^+e^- pairs. This section will cover the optimization of these matrix elements.

6.3.1 Coordinate Systems

A detailed description of the coordinate systems used in the reconstruction of trajectories is given below. Fig. 6.5 illustrates the orientation of each coordinate

system.

Hall Coordinate System

The origin of the Hall Coordinate System (HCS) is at the center of the hall, which is defined by the intersection of the beam axis and the vertical symmetry axis of the target system. The positive \hat{z} direction is along the beam axis towards the beam dump, and the positive \hat{y} direction is vertically up.

Target Coordinate System

Each spectrometer has its own Target Coordinate System (TCS). The positive \hat{z}_{tg} direction is along a line perpendicular to the sieve plane that passes through the central sieve hole. In the ideal case, where the spectrometer is pointing directly at the center of the hall and the sieve slit is perfectly centered on the spectrometer, \hat{z}_{tg} points directly at the hall center. For this case, Z_0 is defined as the distance from the hall center to the central sieve hole. The origin of the TCS is defined as the point on the \hat{z}_{tg} axis that is a distance Z_0 from the sieve surface. The positive \hat{x}_{tg} direction is parallel to the sieve plane, pointing vertically down. The out-of-plane angle (θ_{tg}) and in-plane-angle (ϕ_{tg}) are given by $\frac{dx}{Z_0}$ and $\frac{dy}{Z_0}$ respectively.

Detector Coordinate System

In the lower VDC, the intersection of wire 184 of the U1 plane and wire 184 of the V1 plane defines the origin of the Detector Coordinate System (DCS). In this coordinate system, \hat{y} is parallel to the short symmetry axis of the lower VDC, and

\hat{x} is parallel to the long symmetry axis pointing away from the center of curvature of the dipole. The positive \hat{z} direction is vertically up.

Transport Coordinate System

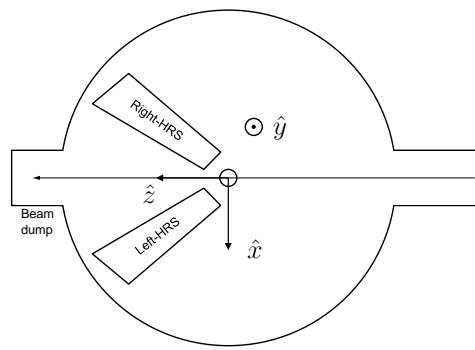
The Transport Coordinate System (TRCS) is generated by rotating the DCS clockwise around the y -axis by 45° . In the TRCS the trajectory of a particle can be represented by a vector

$$\vec{x} = \begin{bmatrix} x \\ \theta \\ y \\ \phi \\ \delta \end{bmatrix} \quad (6.8)$$

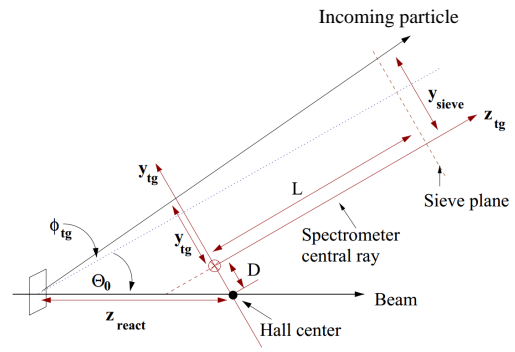
where x is the displacement of the trajectory in the dispersive plane relative the central reference trajectory (vertical direction for the HRS), θ is the tangent of the angle the trajectory makes in the dispersive plane, y and ϕ are the same as x and θ in the transverse plane (horizontal direction for the HRS), and $\delta(\Delta p/p)$ is the fractional momentum of the trajectory from the central momentum setting of the spectrometer.

6.3.2 General Approach

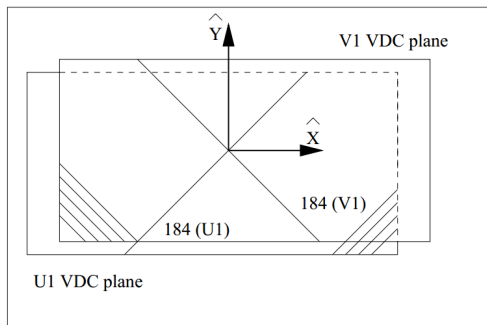
The variables x_{det} , θ_{det} , y_{det} , and ϕ_{det} are measured by the VDCs and are used to calculate the x , θ , y , ϕ , and δ variables at the target. The x_{tg} value can



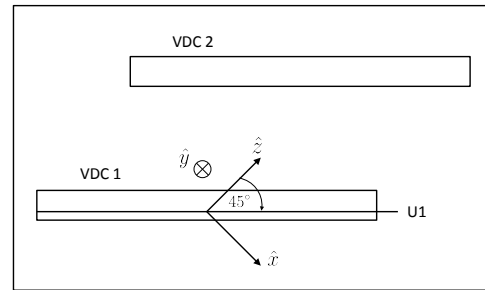
(a) Hall Coordinate System



(b) Target Coordinate System



(c) Detector Coordinate System



(d) Transport Coordinate System

FIG. 6.5: Hall A coordinate systems.

be fixed at zero during optics calibration by requiring the on-target beam position to be within 250 μm of the origin of the Hall Coordinate System. As a first-order approximation the relationship between the focal plane and target coordinates can be written [38]

$$\begin{bmatrix} \delta \\ \theta \\ y \\ \phi \end{bmatrix}_{tg} = \begin{bmatrix} \langle \delta|x \rangle & \langle \delta|\theta \rangle & 0 & 0 \\ \langle \theta|x \rangle & \langle \theta|\theta \rangle & 0 & 0 \\ 0 & 0 & \langle y|y \rangle & \langle y|\phi \rangle \\ 0 & 0 & \langle \phi|y \rangle & \langle \phi|\phi \rangle \end{bmatrix} \begin{bmatrix} x \\ \theta \\ \phi \\ y \end{bmatrix}_{fp} \quad (6.9)$$

where the bra-ket notation denotes the scalar product between directional unit vectors, e.g. $\langle \alpha|\beta \rangle \equiv \hat{\alpha} \cdot \hat{\beta}$. The zero tensor elements result from the mid-plane symmetry of the spectrometer.

The focal plane coordinates are linked to the target coordinates through a set of tensors $Y_{j,k,l}$, $T_{j,k,l}$, $P_{j,k,l}$, and $D_{j,k,l}$ according to [38]

$$y_{tg} = \sum_{j,k,l} Y_{j,k,l} \theta_{fp}^j y_{fp}^k \phi_{fp}^l, \quad (6.10)$$

$$\theta_{tg} = \sum_{j,k,l} T_{j,k,l} \theta_{fp}^j y_{fp}^k \phi_{fp}^l, \quad (6.11)$$

$$\phi_{tg} = \sum_{j,k,l} P_{j,k,l} \theta_{fp}^j y_{fp}^k \phi_{fp}^l, \quad (6.12)$$

$$\delta = \sum_{j,k,l} D_{j,k,l} \theta_{fp}^j y_{fp}^k \phi_{fp}^l, \quad (6.13)$$

where the superscripts denote the power of each focal plane variable. The tensors $Y_{j,k,l}$, $T_{j,k,l}$, $P_{j,k,l}$, and $D_{j,k,l}$ are polynomials in x_{fp} . For example, $Y_{j,k,l}$ can be expressed

$$Y_{j,k,l} = \sum_{i=1}^m C_i^{Y_{j,k,l}} x_{fp}^i, \quad (6.14)$$

so the final expression for y_{tg} is

$$y_{tg} = \sum_{j,k,l} \sum_{i=1}^m C_i^{Y_{j,k,l}} x_{fp}^i \theta_{fp}^j y_{fp}^k \phi_{fp}^l. \quad (6.15)$$

The coefficients $C_i^{Y_{j,k,l}}$ are the optics matrix elements which are stored in a database used to reconstruct the target variables.

6.3.3 Procedure

The transport tensors are optimized by performing a χ^2 minimization on the difference between the reconstructed target variables and the actual target variables. In practice, however, it is difficult to obtain the actual values for the basic target variables y_{tg} , θ_{tg} , and ϕ_{tg} . Instead, the optics matrix elements are calibrated by using a sieve slit collimator. The sieve slit is a removable 5 mm thick tungsten plate with a grid of holes drilled through at known positions, and is inserted in front of the entrance of the spectrometer during a calibration run (see Fig. 6.6). Electrons

lose enough energy when passing through the sieve plate so that only electrons with trajectories passing through the sieve holes reach the detectors. The horizontal and vertical positions of the scattered electron in the sieve plane, x_{sieve} and y_{sieve} , are uniquely determined for quasi-elastic scattered electrons. The basic target variables can be used to calculate the sieve plane variables using the equations

$$x_{\text{sieve}} = x_{tg} + L \tan \theta_{tg}, \quad (6.16)$$

$$y_{\text{sieve}} = y_{tg} + L \tan \phi_{tg}, \quad (6.17)$$

where L is the distance from the hall center to the sieve plane. The vertical coordinate x_{tg} is obtained using the BPMs. The optics matrix elements are optimized by minimizing the following function:

$$\chi_x^2 = \sum_{i=1}^{\text{Events}} (x_{\text{sieve}}^i - x_{\text{sieve}}^0)^2 \quad (6.18)$$

$$\chi_y^2 = \sum_{i=1}^{\text{Events}} (y_{\text{sieve}}^i - y_{\text{sieve}}^0)^2, \quad (6.19)$$

where x_{sieve}^0 and y_{sieve}^0 correspond to the surveyed location of the sieve hole. Only 1000 events are selected for each hole in order to avoid any bias across the full acceptance.

The momentum calibration is performed by scanning the central momentum of

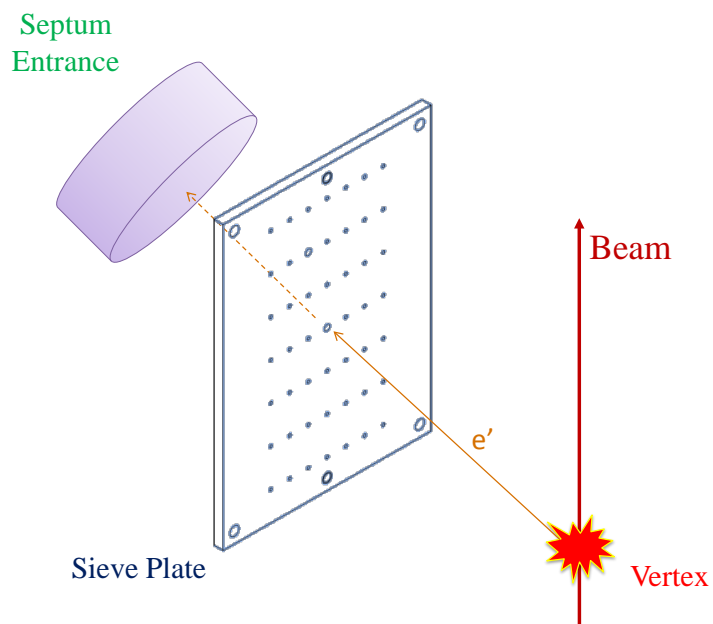


FIG. 6.6: During the angular calibration sieve slits were inserted between the reaction vertex and the entrance to the septum magnet [39]. Only the electrons whose trajectories pass through the sieve holes reach the detectors. The optics matrix elements can be optimized by comparing the reconstructed holes locations with the surveyed hole locations.

the spectrometer p_0 around the elastic peak, i.e., δ -scans at $p_0 = p_{\text{elastic}}, \pm 1\%, \pm 2\%, \pm 3\%$, and $\pm 4\%$. The real momentum is calculated using the scattering angle and the corrections due to the radiative energy losses in the target material. The δ matrix elements are optimized by performing a global fit on data from all δ -scan points.

The full APEX experiment will use a target consisting of multiple tungsten ribbons located along the beam axis. Therefore, it is important to calibrate the reconstruction of the reaction vertex, z_{react} . The reaction vertex can be calculated using the equation

$$z_{\text{react}} = -(y_{tg} + D) \frac{\cos \phi_{tg}}{\sin \theta_0 + \phi_{tg}} + x_{\text{bpm}} \cot \theta_0 + \phi_{tg}, \quad (6.20)$$

where D is the horizontal displacement of the spectrometer from its ideal position and θ_0 is the central angle of the spectrometer. The vertex calibration is done using data from deep inelastic scattering on a multi-carbon foil target. Like the calibration procedure described above, the δ_{tg} optics matrix elements are optimized using χ^2 minimization. Fig. 6.7 shows an example of the reconstructed foil vertex peaks after calibration.

6.3.4 Results

During the APEX test run the optics calibration was done by Jin Huang (MIT) and Vincent Sulkosky (MIT). All calibration data used a 1.162 GeV electron beam.

The angular calibration used elastic scattering on a tantalum foil target with the sieve slits inserted in front of the entrance of the septum magnets. Calibrating

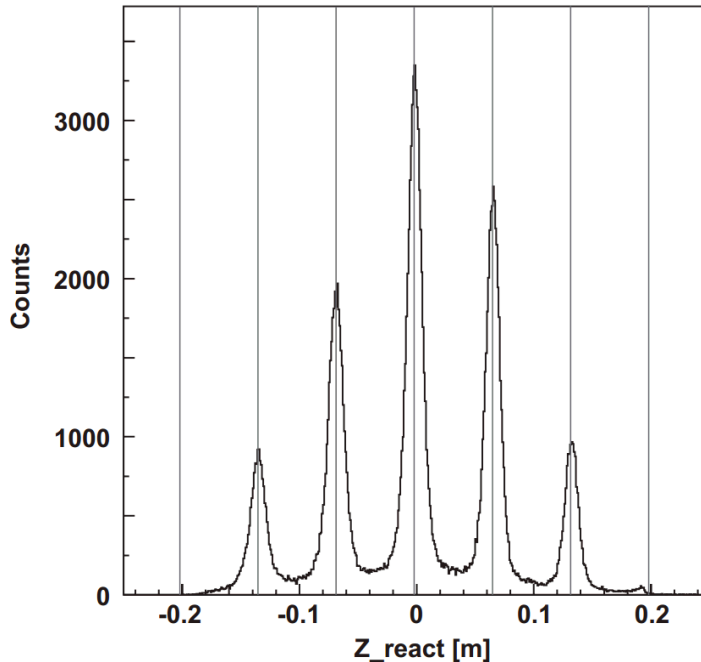
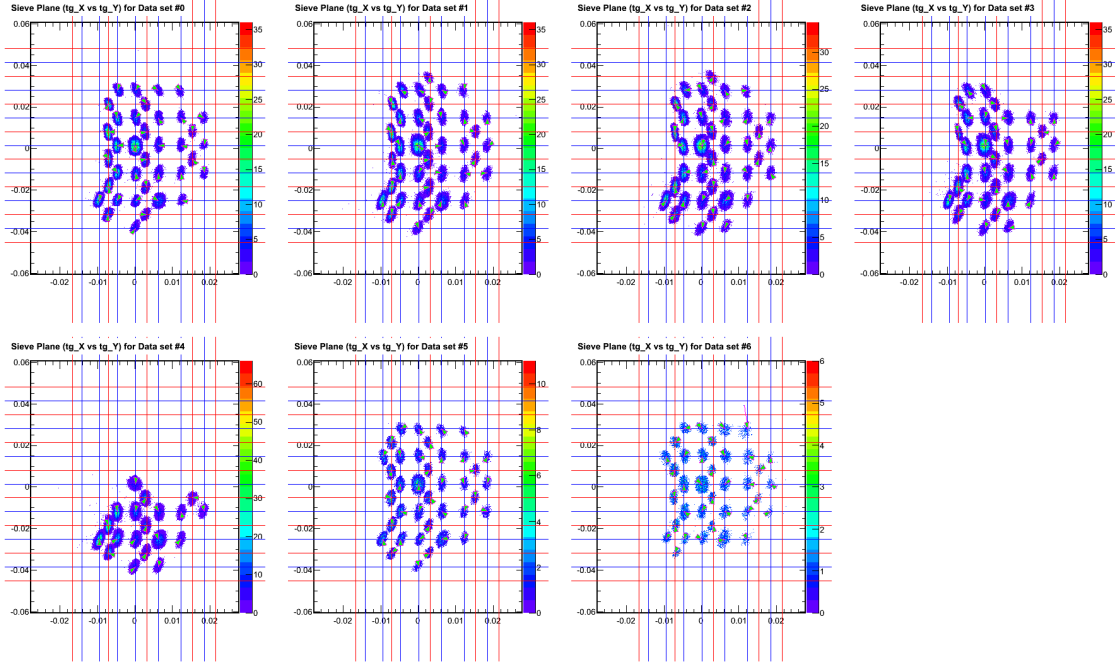


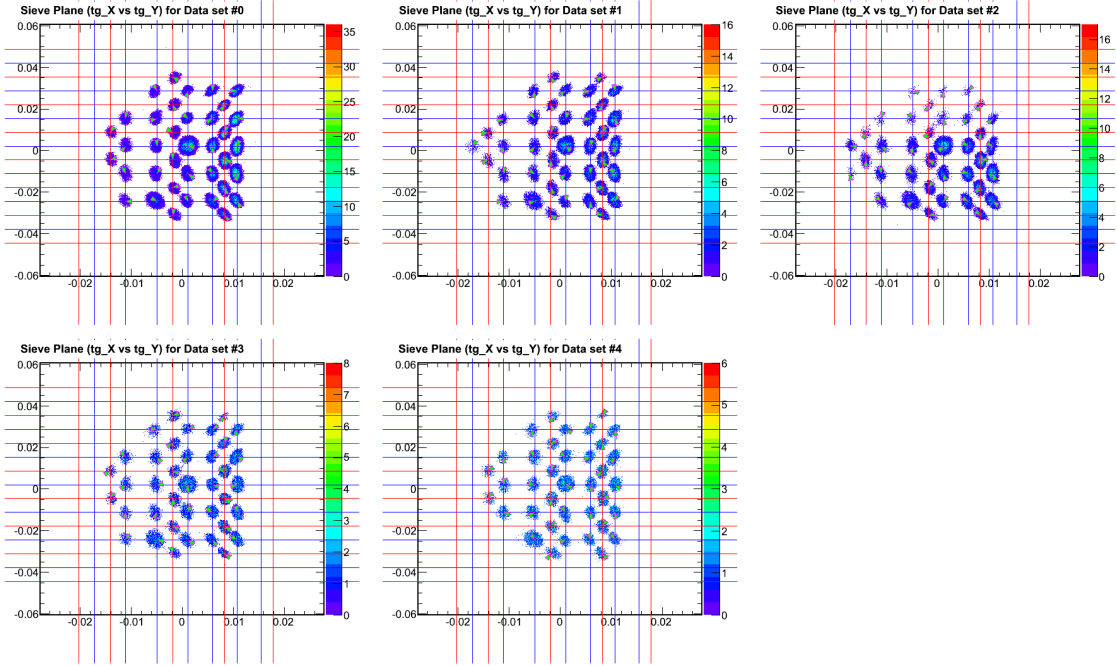
FIG. 6.7: An example of the reconstructed foil positions along the beam line after performing the vertex calibration (plot taken from [23]). The blue lines indicate the surveyed positions of the foils.

the full coverage of the HRS momentum acceptance is normally done by scanning the HRS central momentum setting from $\delta \approx -4\% \sim +4\%$. However, due to limitations of the septum magnet current, it was only possible to scan the $\delta \approx 0\% \sim +4\%$ acceptance region. To calibrate the full momentum acceptance, data from the elastic radiative tails of $\delta \approx 0\%$ was used. Table 6.1 summarizes the data used to perform the angular calibration. The matrix elements for each spectrometer were optimized for all data sets simultaneously. The reconstructed sieve holes after calibration are shown in Fig. 6.8. The final horizontal (vertical) angular resolutions achieved were 0.29 (1.86) mrad for the Left-HRS and 0.44 (1.77) for the Right-HRS. See Sec. 7.6.1 for details on determining the angular resolution.

The momentum calibration used the same elastic data as the angular calibra-



(a) Left-HRS



(b) Right-HRS

FIG. 6.8: Reconstructed sieve holes for all data sets (see Table 6.1) after calibration. The red and blue lines correspond to the surveyed sieve hole locations. All units are in mm.

TABLE 6.1: Summary of the angular calibration data sets.

Left-HRS		
Data set	Run number	δ
0	1170	0% with elastic peak
1	1172	+1% with elastic peak
2	1181	+2% with elastic peak
3	1183	+3% with elastic peak
4	1190	+4% with elastic peak
5	1169-1170	-3% \sim -1% with elastic tail
6	1169-1170	-4% \sim -3% with elastic tail

Right-HRS		
Data set	Run number	δ
0	1898	0% with elastic peak
1	1911	+2% with elastic peak
2	1920	+4% with elastic peak
3	1898-1899	-2% \sim -1% with elastic tail
4	1898-1899	-3.5% \sim -2% with elastic tail

tion. Although the momentum could only be calibrated for $\delta \approx 0\% \sim +4\%$, the reach of the calibration was extended to negative δ through a linear extrapolation of the optics database used for the pentaquark search E04-012 experiment [40]. Despite the lack of negative δ data, the extrapolation of the existing δ matrix elements allowed us to achieve a relative momentum resolution of $< 5 \times 10^{-4}$ (Fig. 6.9). The relative momentum resolution has a small contribution to the mass resolution, so this result is sufficient.

Since the test run used a single foil target, a good vertex resolution is not heavily demanded. The vertex position was roughly calibrated for both spectrometers using the tantalum foil and multi-carbon foil targets. The HRS central momentum setting was set such that $\delta \approx -10\%$. The vertex resolution achieved for the tantalum foil target was 27 mm for the Left-HRS and 17 mm for the Right-HRS.

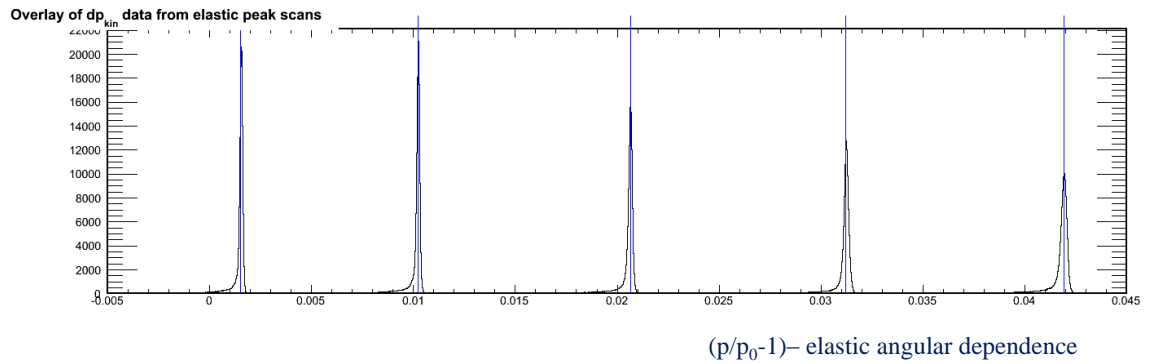


FIG. 6.9: An overlay of the δ -scans for the Left-HRS after calibration. The final relative momentum resolution achieved was $< 5 \times 10^{-4}$.

7

Data Analysis

The ultimate goal of the data analysis is to generate the final invariant mass spectrum of all true e^+e^- pairs collected during the APEX test run and determine the mass resolution achieved by the experiment. Once the final event sample is produced we can search for the A' by performing a peak search on the e^+e^- invariant mass spectrum. The details of the peak search will be discussed in Chapter 8.

Selecting true e^+e^- pairs requires the ability to distinguish true coincidence events from accidental coincidence events. It also requires sufficient particle identification by the detectors. Only events with good quality tracks in the vertical drift chambers and trajectories falling within the calibrated acceptance of the spectrometers should be used in the final event sample. All aspects of the final event selection will be discussed in this chapter. We will also discuss the procedure for determining the mass resolution of the experiment. Finally, all concerns raised by the PAC on the experiment's proposal will be addressed.

7.1 Analysis Software

The ADC and TDC data from the detectors is initially stored in a raw CODA format. Each piece of information coming from the electronics is written as a hexadecimal data word. The raw data is converted into ROOT trees using the Hall A ROOT/analyzer facility [41]. The Hall A analyzer is object-oriented code written in C++ and is built on top of the ROOT platform [42]. It provides abstraction for physical objects such as a spectrometer composed of several detector systems. The analyzer decodes the raw data into physical variables that are ready to be visualized with histograms.

The Hall A analyzer can be installed and used on any computer; however, the APEX test run data could not be stored on a single machine. Instead, the raw data is stored on Jefferson Lab's 7 PB storage silo. Each data file requires ≈ 2 hours on a work-station computer to be analyzed. That means it would take almost three weeks to analyze all of the APEX test run data sequentially on a single computer. Therefore, the analysis of the data was performed on Jefferson Lab's batch farm. The farm's cluster contains ≈ 100 computing nodes and is capable of running ≈ 1000 simultaneous jobs, with the limitation of 256 jobs per user at one time [37]. Using the batch farm the analysis of all APEX test run data could be done in just a few days.

7.2 Particle Identification

When producing the invariant mass spectrum of e^+e^- pairs it is essential to minimize meson contamination of the final event sample. During the test run the meson background was dominated by π^+ . In the Right-HRS, the observed ratio of e^+ to meson background rates, N_{e^+}/N_{meson} , is $\sim 1/1.5$ with a 2.232 GeV electron beam incident on the tantalum foil target (determined using the gas Cherenkov data). Ideally the on-line N_{e^+}/N_{π^+} ratio should be $\gtrsim 10/1$, so we require an online meson background rejection factor of $\gtrsim 15$ in the Right-HRS. The observed ratio of e^- to meson background rates in the Left-HRS is $\sim 50/1$, so on-line meson background rejection is not required in the Left-HRS.

There are two types of particles identification detectors in the HRSs: the gas Cherenkov counter (GC) and the two-layer lead-glass calorimeter (LG). While the GC is sensitive to electrons and positrons in the momentum range of interest for this experiment, the probability of pions inducing any signal in the GC is $< 2\%$. This translates to a pion rejection factor of at least 50. The LG has good segmentation and amplitude resolution, which allows a pion rejection factor of at least 100. The simplest trigger configuration which provides on-line π^+ rejection uses only the GC in the Right-HRS. This was the configuration used during the APEX test run. The LG was used to analyze the particle identification efficiency of the GC.

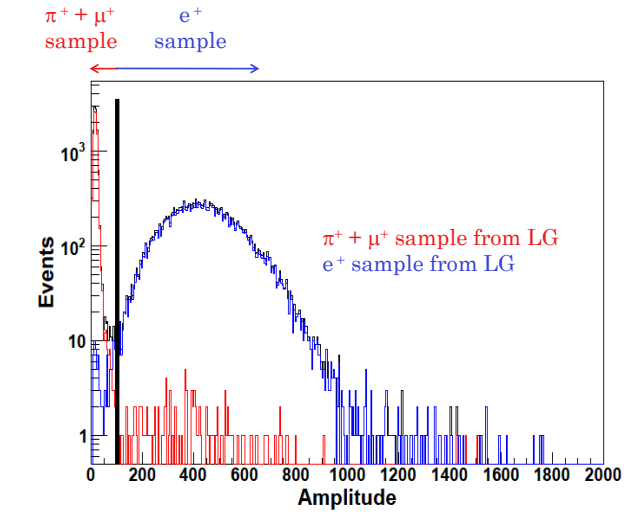
Fig. 7.1a shows the ADC sum of all ten PMTs in the Right-HRS GC for the lead target data. The sharp peak at the lower end of the spectrum is assumed to contain the meson background and everything that follows is assumed to contain

e^+ . Also shown is the GC ADC spectrum for e^+ (blue) and meson background (red) events as determined by the LG in the Right-HRS. Particles are identified in the LG by plotting the total energy deposited in both layers of the calorimeter over the initial momentum of the incoming particle (Fig. 7.1b). The first peak at the lower end of the spectrum contains π^+ , the second peak contains μ^+ , and the third peak contains e^+ . Also shown are the e^+ (blue) and meson background (red) events as determined by the GC.

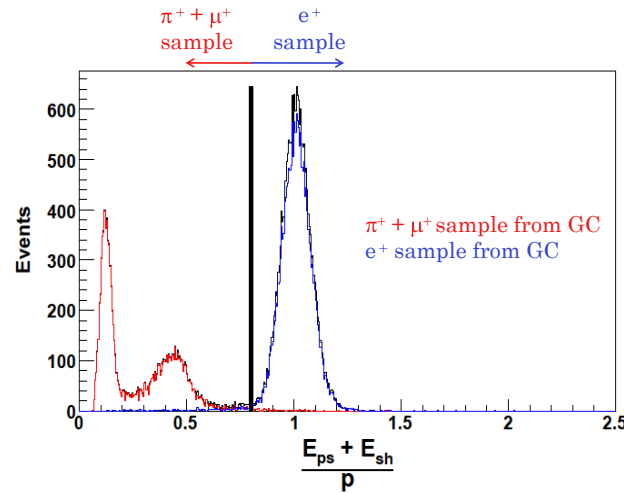
The meson background efficiency is calculated by taking the fraction of meson background (as determined by the calorimeter) found in the GC e^+ region. A similar approach can be used to calculate the e^+ detection efficiency of the GC. When operating at a ~ 57 kHz Right-HRS trigger rate the gas Cherenkov counter has a 99.5% e^+ detection efficiency and 98.7% meson background rejection efficiency. In other words, the meson background is rejected on-line by a factor of ~ 75 which is ~ 5 times higher than the minimum requirement. Using the GC counters of both HRSs the meson background contamination of the final event sample was determined to be 0.9%, the majority of which comes from $e^+\pi^-$ events.

7.3 Event Selection

Events accepted into the final data sample were selected by applying a series of cuts to the data. These cuts were designed to select only events with good quality tracks with trajectories residing within the calibrated region of the spectrometers, and to reduce the number of accidental coincidence events.



(a)



(b)

FIG. 7.1: The lead glass calorimeter was used to study the particle identification efficiency of the gas Cherenkov counter used in the coincidence trigger. (A) shows the ADC sum of all ten PMTs in the Cherenkov detector. Events with amplitudes to the right of the black line are considered e^+ , while events with amplitudes to the left are considered meson background. The blue and red lines correspond to e^+ and meson background events as determined by the calorimeter. (B) shows the total energy deposited in both layers of the calorimeter over the initial momentum of the incoming particles. The first peak contains π^+ events, the second contains μ^+ events, and the third contains e^+ events.

7.3.1 Coincidence Timing

To select e^+e^- coincidence events a triple coincidence trigger was implemented. The trigger consisted of the S2m scintillator planes of both HRSs and the gas Cherenkov counter of the Right-HRS (positron arm). The gas Cherenkov counter was used to provide on-line π^+ rejection. Although the trigger was designed to only select e^+e^- pairs there are still a significant number of background events recorded from accidental coincidence events. Accidentals result from uncorrelated background events that happen to arrive at the detectors within the coincidence timing window.

A timing diagram of the coincidence trigger is shown in Fig. 7.2a. When triggered, the S2m plane of each HRS sends a 20 ns pulse to a coincidence unit, whereas width of the gas Cherenkov counter pulse is 10 ns. When all three pulses overlap the data from all detectors is recorded and the event is tagged as a “golden” coincidence event.

The coincidence timing spectrum from a single data run is shown in Fig. 7.2b. The plot shows the time difference between the T1 trigger (Left-HRS S2m plane) and the T6 trigger (“golden” coincidence trigger). The ~ 10 ns wide peak contains true coincidence events, whereas the rest of the spectrum contains accidental coincidence events. To select only true coincidence events a 12.5 ns wide cut was imposed around the true coincidence timing peak (260-272.5 ns).

The rate of accidentals can be estimated from the singles rate in each HRS and

the duration of the timing window:

$$N_{\text{accidentals}} \simeq \sigma N_{\text{Left}} N_{\text{Right}} \quad (7.1)$$

where $N_{\text{accidentals}}$ is the rate of accidentals, N_{Left} and N_{Right} are the singles rates of each HRS, and σ is the size of the timing window. This means that $N_{\text{accidentals}}$ scales with the square of the total coincidence trigger rate. The test run data had a signal to background ratio of $\sim 5/1$ (Fig. 7.2b). The full experiment will use a multi-foil target with a total target thickness of 4.3% radiation lengths (see Sec. 4.4.1), which is ~ 10 times thicker than the test run target. Also, the PREX collimators described in Sec. 7.3.2 will not be present during the full experiment, so the spectrometer acceptance will be increased by a factor of ~ 2 . The resulting signal to background ratio will be $\sim 1/4$; however, this can be improved offline to $\sim 12/1$ by applying timing cuts (factor of ~ 5 accidental reduction) and correcting on multiple target hits (factor of ~ 10 accidental reduction).

7.3.2 Acceptance Cuts

To accurately reconstruct the momentum of particles at the target it is important to avoid recording events with trajectories outside the calibrated region of the spectrometers. The PREX experiment [35], which took place in Hall A prior to the APEX test run, had installed collimators at the entrance of each spectrometer (Fig. 7.3). Due to a lack of time the collimators were not removed for the test run, and therefore restricted the acceptance of the HRSs.

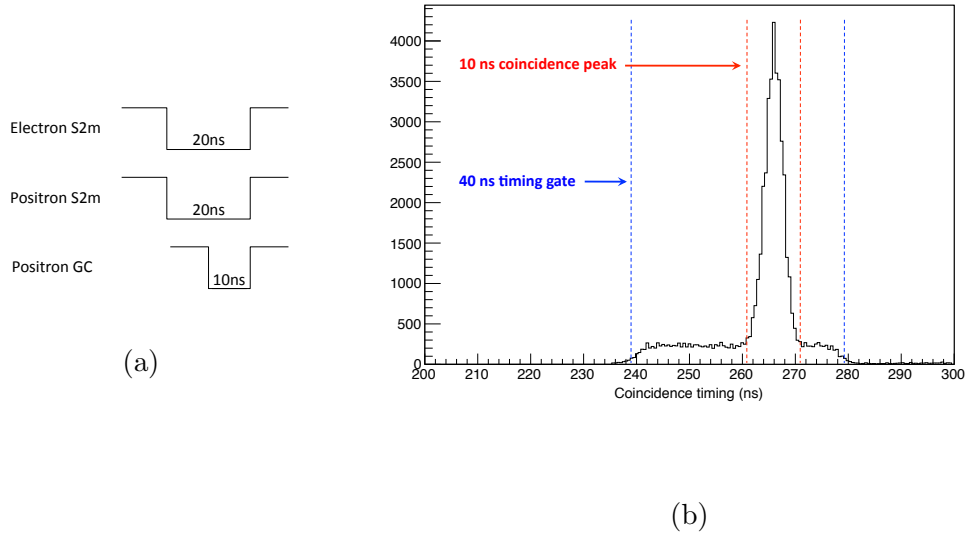


FIG. 7.2: (a) shows a timing diagram of the coincidence trigger used during the test run. The overlap of both 20 ns S2m pulses and the 10 ns Right-HRS gas Cherenkov pulse creates a “golden” coincidence trigger. (b) shows the time difference between the Left-HRS S2m plane and the coincidence trigger. Notice the 40 ns duration of the coincidence timing gate and the 10 ns peak containing true coincidence events.

For each spectrometer, the acceptance is defined by three sets of two-dimensional polygonal cuts made in θ_{tg} vs. ϕ_{tg} , δ_{tg} vs. ϕ_{tg} , and δ_{tg} vs. θ_{tg} . The θ_{tg} , ϕ_{tg} , and δ_{tg} variables correspond to the vertical angle, horizontal angle, and momentum deviation, respectively, in the target coordinate system as described in Sec. 6.3.1. The cuts are shown in Fig. 7.4. The solid angle acceptance after applying these cuts is $\simeq 2.8(2.9)$ msr for the left (right) HRS, whereas the nominal solid angle acceptance without the presence of the PREX collimators is 4.3 msr.

7.3.3 Final Event Sample

The timing and graphical cuts described above were applied to the data to select the final event sample. Using the timing distribution in Fig. 7.2b one finds

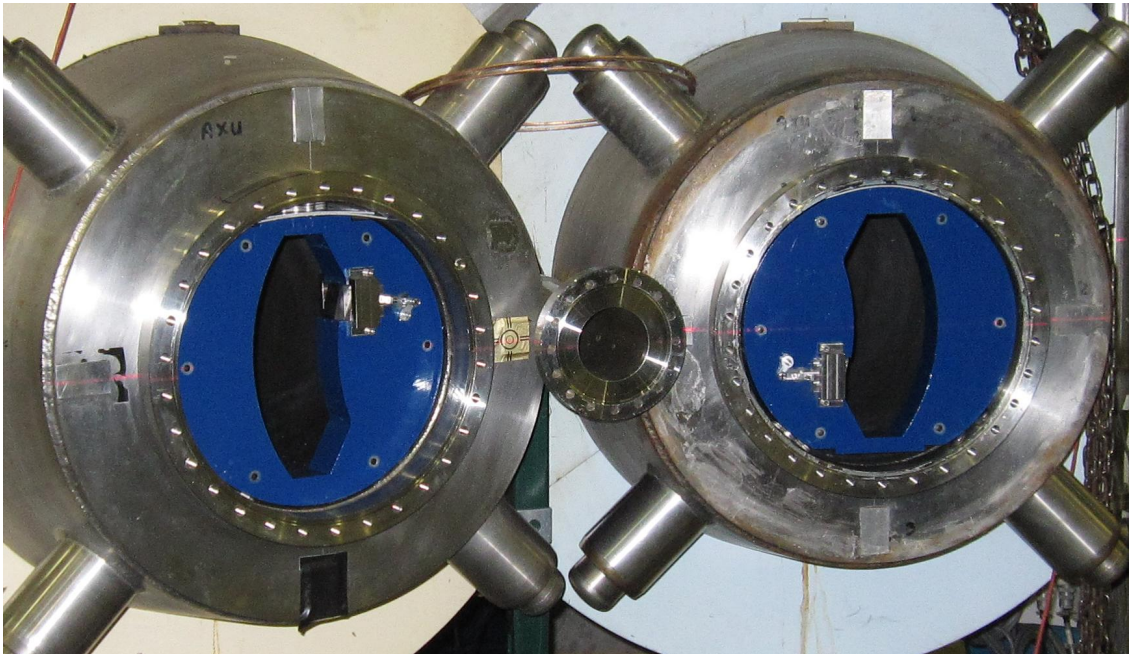


FIG. 7.3: The presence of collimators from the PREX experiment reduced the solid angle acceptance of each spectrometer from the nominal 4.1 msr to $\simeq 2.8(2.9)$ msr for the left (right) HRS.

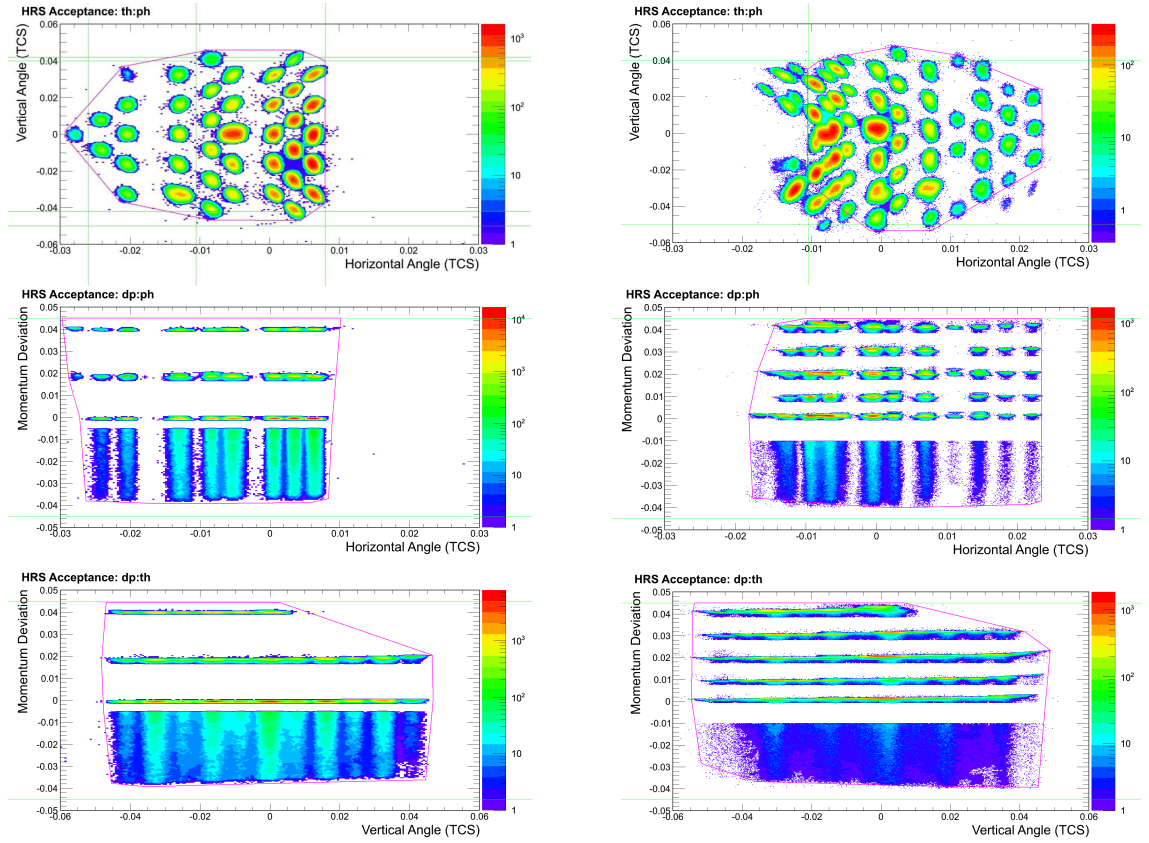


FIG. 7.4: The acceptance of each spectrometer is defined by 2-D graphical cuts applied to θ_{tg} vs. ϕ_{tg} , δ_{tg} vs. ϕ_{tg} , and δ_{tg} vs. θ_{tg} . The cuts are shown by the area outlined in pink.

that 14.9% of events in the coincidence peak contain accidentals. An easy way to reduce the accidentals by a factor ~ 2 is to demand the sum of the e^- and e^+ momentum be less than the beam energy. After applying this energy cut the fraction of accidentals in the coincidence peak was reduced to 7.4%, as expected.

In addition to the cuts described above we require good quality track reconstruction in the VDC. If the analyzer is unable to reconstruct a good quality track for an event, e.g. there is ambiguity between clusters in the U and V planes of a VDC (see Sec. 7.4), it will set the root variable "tr.ok" to zero; otherwise, the variable will be set to one. Events with good quality tracks are selected by requiring that "tr.ok==1". Multiple tracks observed in the same spectrometer for a single event create ambiguity in the track selection. Therefore, we require that events have only one observed track in each spectrometer.

After applying all cuts to the data the final event sample contains 770,500 events with only 0.9% contamination from meson backgrounds, and 7.4% accidental e^+e^- coincidence events.

7.4 Track Reconstruction

The momentum reconstruction of e^+e^- pairs begins with the measurement of the position and angle of the incoming particles in the focal plane. This measurement is made using the VDCs, the details of which are described in Sec. 3.2.3. Tracks enter the VDCs nominally at 45° and produce signals in 3-7 wires at a time. TDCs measure the time interval between the wire signals and a common stop signal that

is generated from one of the triggers.

Activated wires adjacent to one another are organized into clusters. The drift time, or the time it takes ionized electrons to travel from the trajectory to the sense wires, is determined for each wire within the cluster. Wires at the edge of a cluster have a longer drift time than wires near the center of the cluster, as illustrated in Fig. 7.5. The cluster search algorithm scans the VDC data for ‘V’ shaped clusters in time. The drift time of each wire is measured by the TDCs and converted into the drift distance, or the perpendicular distance from the trajectory to the wire plane. A linear fit is performed on the drift distances within a cluster, giving the approximate track angle, θ_{Q_i} , and intersection point, Q_i , at the wire plane [43].

Two VDCs are used in each HRS, each with U and V planes. As shown in Fig. 7.6a, the global trajectory angles are defined according to

$$\tan \theta_Q = \frac{Q_2 - Q_1}{d}, \quad (7.2)$$

where $Q \in (U, V)$ and the distance d between like wire planes (U1 and U2; V1 and V2) is $\simeq 0.335\text{m}$ [25]. Keep in mind that the wires in the U planes are orthogonal to those in the V planes. The global angles θ_Q can then be used to project the track coordinate measured by the V1 plane into the U1 plane, as shown in Fig. 7.6b. The variable V is the V1 coordinate projected into the U1 plane, and is given by

$$V = V1 - \Delta V = V1 - l_0 \tan \theta_V, \quad (7.3)$$

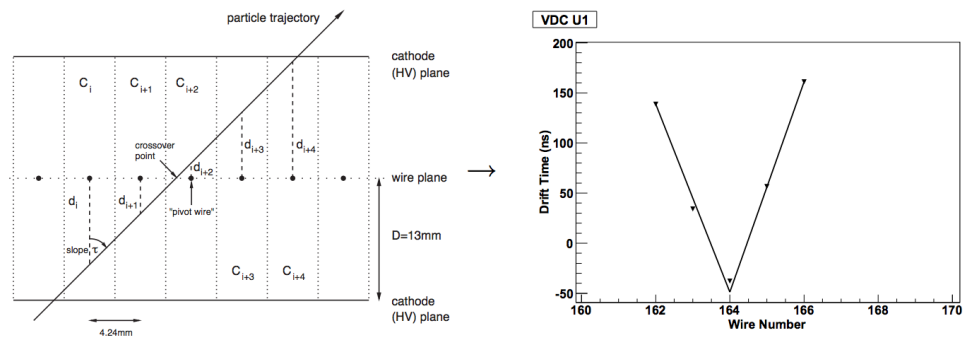
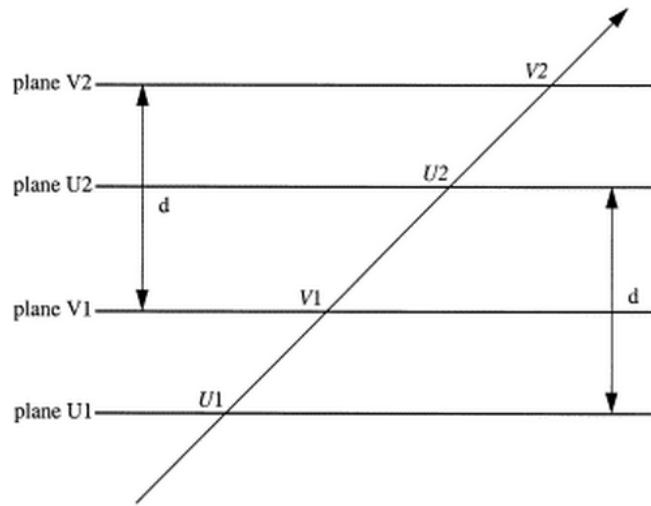


FIG. 7.5: Example of a VDC cluster containing five activated wires. Wires toward the edge of the cluster have a longer drift time than wires near the center. Thus, the drift times of the wires within the cluster exhibit a ‘V’ shape.

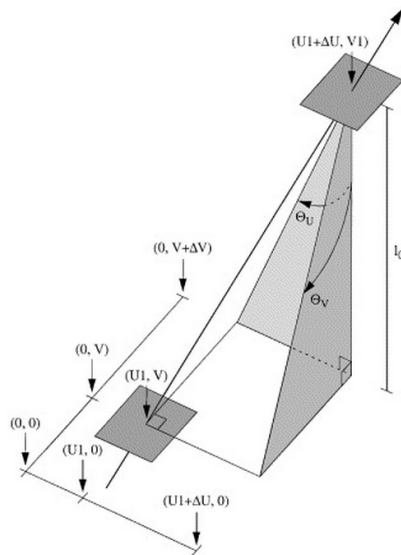
where the distance l_0 between the U1 and V1 planes is 26 mm [25]. The design of this two-VDC system allows all trajectories to be characterized by a set of four unique coordinates (U, V, θ_U , and θ_V). These coordinates can then be transformed into other coordinate systems, as described in Sec. 6.3.

A couple of modifications were made to the track reconstruction algorithm for the analysis of the test run data. The track reconstruction required that the time difference between the U cluster and V cluster be within ± 40 ns. Also, if there is any ambiguity in the association of U clusters with V clusters, i.e. a cluster in the U plane is associated with more than one V cluster, then the tracking ends and the event is flagged. Fig. 7.7 demonstrates both of these modifications.

An understanding of the track reconstruction efficiency is required to compute the rate of e^+e^- pair production during the test run. The track reconstruction efficiency can be estimated by determining how often the reconstructed trajectories of true e^+e^- pair events fall within the active region of the VDCs. True coincidence events are selected by applying the coincidence peak timing cut described above. The number of these events with trajectories passing through the acceptable region of the VDC plane is determined by applying the “loose” acceptance cuts defined in Table 7.1. The cuts are made on the detector coordinate system variables (see Sec. 6.3.1) and are shown in Fig. 7.8. The track reconstruction efficiencies are calculated by taking the ratio of coincidence events that pass the cuts to the total coincidence events, N_{cut}/N . The track reconstruction efficiencies for the LHRS (RHRS) are 99.0% (98.2%).



(a)



(b)

FIG. 7.6: (a) The intersection points at like planes ($U1$ and $U2$; $V1$ and $V2$) can be used to determine the global trajectory angles, θ_U and θ_V . Note that the wires in the U planes are orthogonal to those in the V planes. The wires in both planes are oriented 45° with respect to the plane of the page. (b) The global trajectory angles can then be used to project the $V1$ plane coordinates into the $U1$ plane.

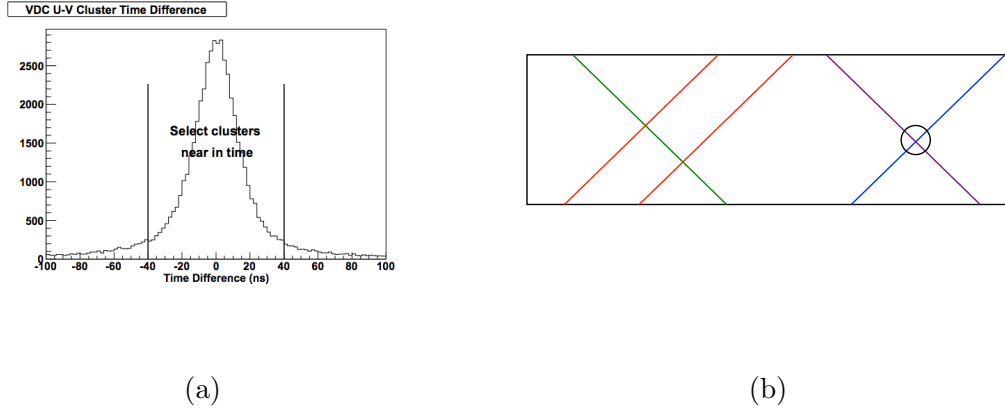


FIG. 7.7: Modifications made to the tracking algorithm. (a) shows the distribution of the time difference between the U and V clusters. A cut was made requiring that the time difference be within ± 40 ns. (b) demonstrates a case where a U cluster (green line) is associated with more than one V clusters (red lines). Tracks are not constructed for events exhibiting UV association ambiguity.

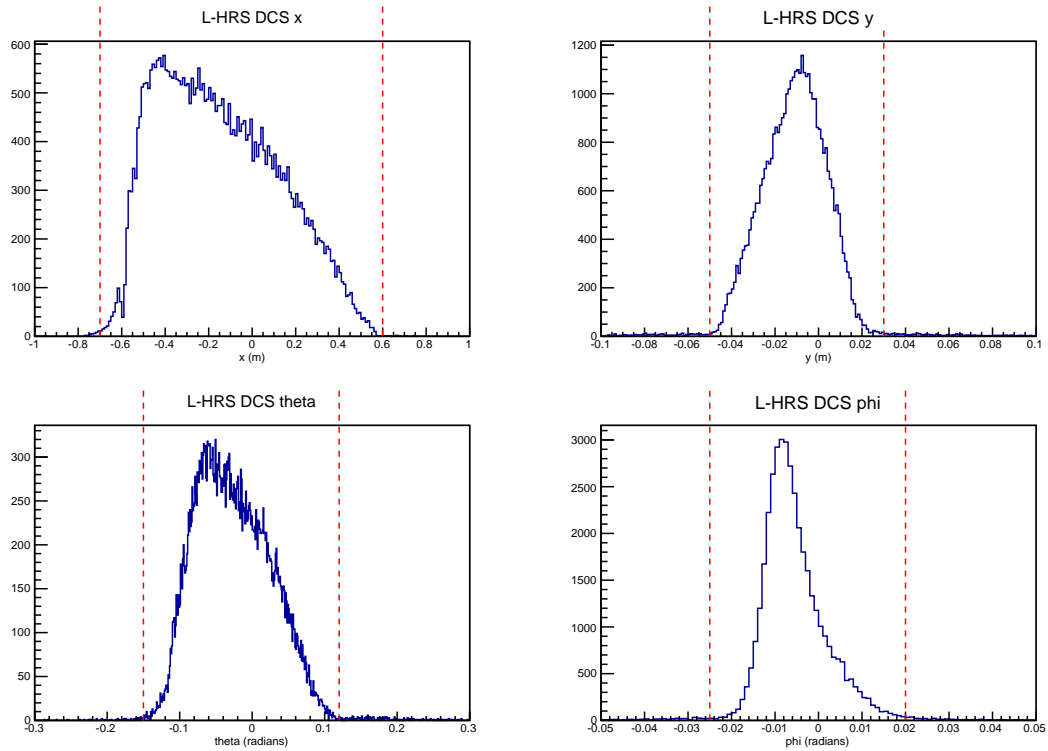
TABLE 7.1: “Loose” acceptance cuts used for estimating the track reconstruction efficiency. All variables are in the detector coordinate system.

Left-HRS	Right-HRS
$-0.7 \text{ m} < x < 0.6 \text{ m}$	$-0.7 \text{ m} < x < 0.6 \text{ m}$
$-0.05 \text{ m} < y < 0.03 \text{ m}$	$-0.04 \text{ m} < y < 0.04 \text{ m}$
$-150 \text{ mrad} < \theta < 120 \text{ mrad}$	$-150 \text{ mrad} < \theta < 120 \text{ mrad}$
$-25 \text{ mrad} < \phi < 25 \text{ mrad}$	$-20 \text{ mrad} < \phi < 25 \text{ mrad}$

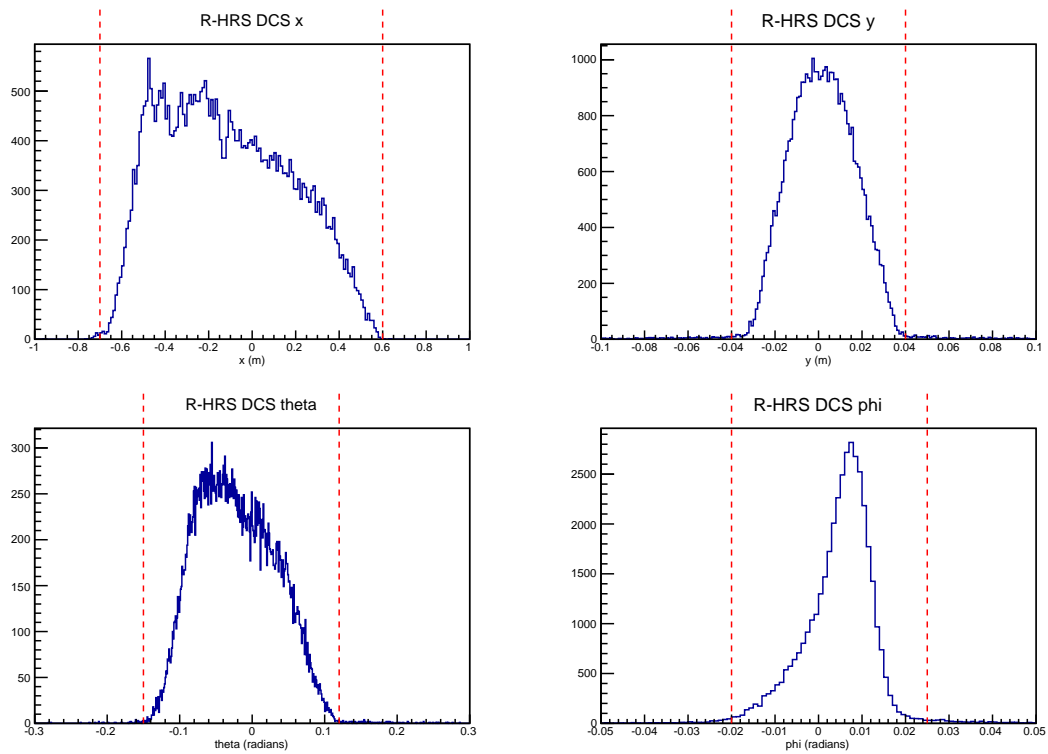
7.5 Invariant Mass Calculation and Comparison to MC Data

The invariant mass of e^+e^- pairs can be calculated as

$$m_0^2 = (E_{e^+} + E_{e^-})^2 - (\vec{p}_{e^+} + \vec{p}_{e^-})^2. \quad (7.4)$$



(a)



(b)

FIG. 7.8: Plots illustrating the “loose” acceptance cuts used to determine the track reconstruction efficiency for the (a) Left-HRS and (b) Right-HRS. All variables are in the detector coordinate system. 112

Resolving the parentheses:

$$m_0^2 = E_{e^+}^2 + E_{e^-}^2 + 2E_{e^+}E_{e^-} - \vec{p}_{e^+}^2 - \vec{p}_{e^-}^2 - 2\vec{p}_{e^+} \cdot \vec{p}_{e^-}. \quad (7.5)$$

Substituting in $m_{e^\pm}^2 = E_{e^\pm}^2 - \vec{p}_{e^\pm}^2$ gives

$$m_0^2 = m_{e^+}^2 + m_{e^-}^2 + 2E_{e^+}E_{e^-} - 2\vec{p}_{e^+} \cdot \vec{p}_{e^-}. \quad (7.6)$$

Since the masses of e^+ and e^- are negligible, the invariant mass can be expressed

$$m_0^2 = 2|p_{e^+}||p_{e^-}| - 2\vec{p}_{e^+} \cdot \vec{p}_{e^-}. \quad (7.7)$$

Eq. 7.7 can be written in terms of the x , y , and z momentum components in the lab frame or "Hall A Coordinate System" (HCS):

$$m_0^2 = 2(|p^{e^+}||p^{e^-}| - (p_x^{e^+}p_x^{e^-} + p_y^{e^+}p_y^{e^-} + p_z^{e^+}p_z^{e^-})). \quad (7.8)$$

In the HCS $+\hat{z}$ points in the beam direction and $+\hat{y}$ points upward.

Each HRS measures the δ , θ , and ϕ variables in the "Target Coordinate System" or TCS, whose z -axis points towards the center of HRS's entrance. $\delta = 1 - \frac{p}{p_0}$, where p_0 is the central momentum setting of the HRS, and θ and ϕ are the vertical and horizontal angles with respect to z_{TCS} . These variables can be translated into the three dimensional momentum variables of the particle at the vertex in the HCS

using the equations

$$p_x = p_{z_{\text{TCS}}} (\tan \phi \cos \theta_0 + \sin \theta_0) \quad (7.9)$$

$$p_y = p_{z_{\text{TCS}}} \tan \theta \quad (7.10)$$

$$p_z = p_{z_{\text{TCS}}} (\cos \theta_0 - \tan \phi \sin \theta_0) \quad (7.11)$$

where

$$p_{z_{\text{TCS}}} = \frac{p_0(1 + \delta)}{\sqrt{1 + \tan^2 \theta + \tan^2 \phi}} \quad (7.12)$$

and θ_0 is the angle of the HRS with respect to the beam ($+5^\circ$ for the Left-HRS and -5° for the Right-HRS).

After making the final event selection of the entire production data sample, the invariant mass of each event was calculated. Over 770,500 true e^+e^- pairs were collected in the mass range of 175-250 MeV. Fig. 7.9 shows the invariant mass spectrum for all good e^+e^- pairs collected during the test run. The bin width of the histogram is 50 keV.

The production of leading order QED trident processes was calculated using MadGraph and MadEvent, as discussed in Sec. 4.2. The acceptance cuts that were applied to the final data sample of the test run (Sec. 7.3.2) were also applied to the calculated coincident event sample. The invariant mass spectrum of the calculated

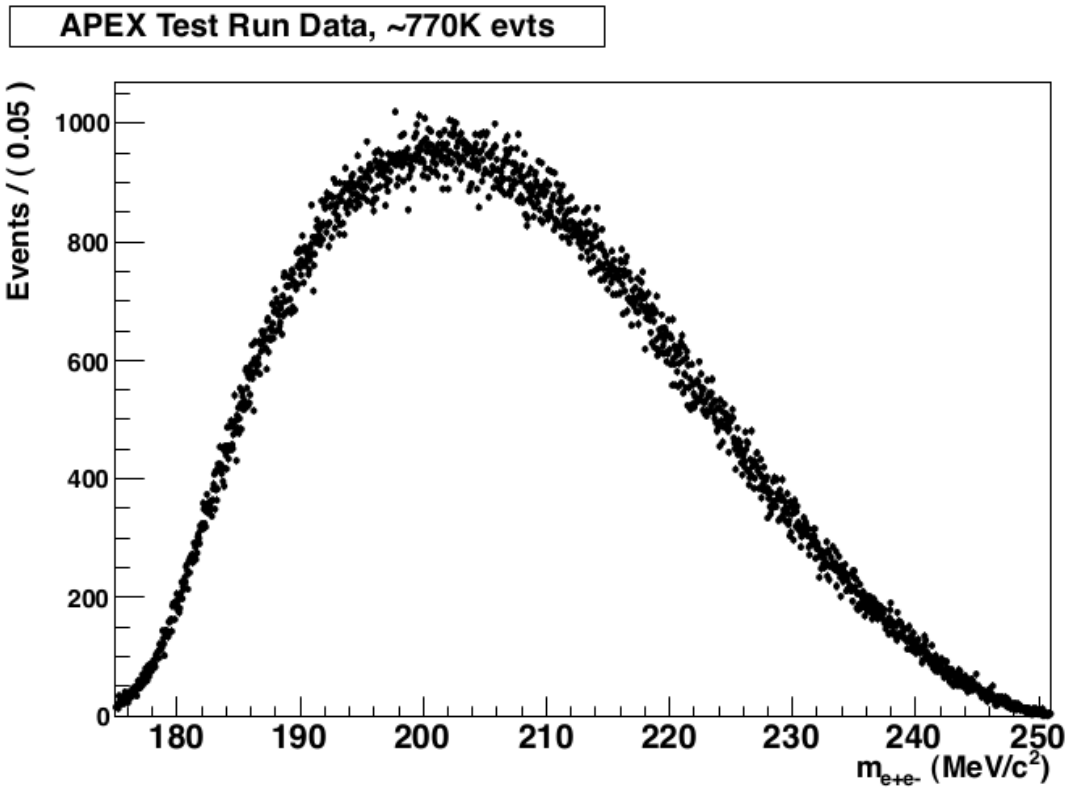


FIG. 7.9: The invariant mass spectrum of all true e^+e^- pairs collected during the test run. Data was collected in the mass range of 175-250 MeV.

event sample normalized to the test run data is shown in Fig. 7.10. The calculated QED trident spectrum was added to the accidental event sample, which consisted of trigger events residing outside of the coincidence timing peak (see Fig. 7.2b). The QED trident rates calculated for the test run configuration agree within a few percent with the actual data. The differential momentum and angular distributions agree with the data to within 5 – 10%. Fig. 7.11 compares the Monte Carlo data with the test run data.

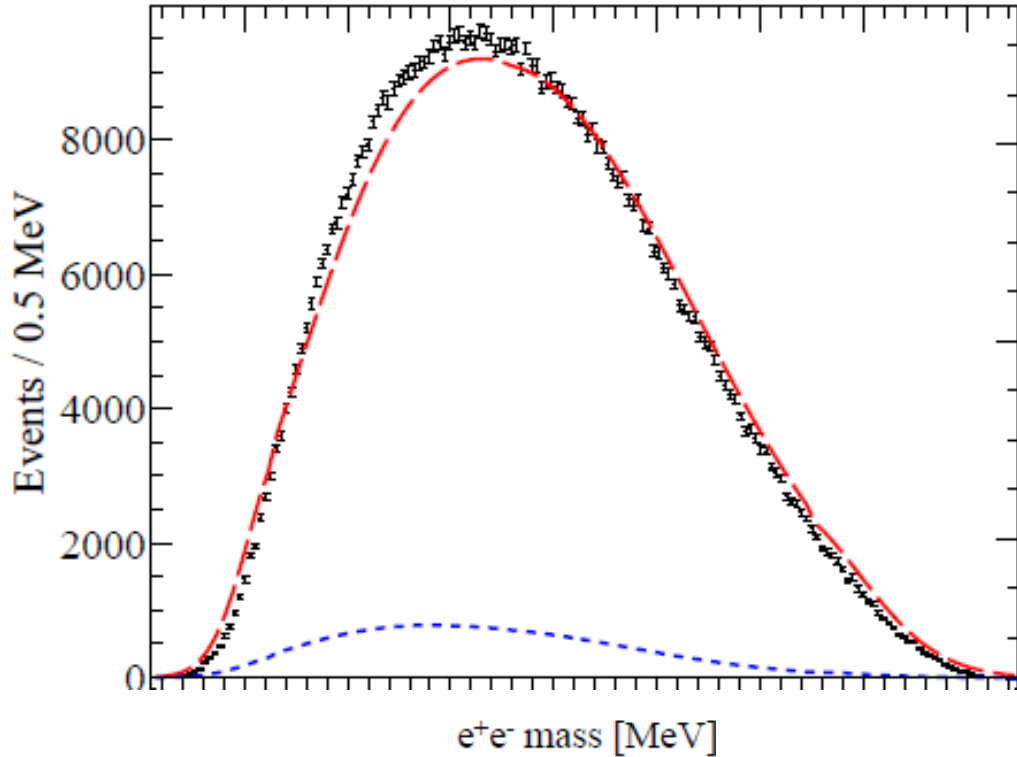


FIG. 7.10: The invariant mass spectrum of e^+e^- pair events collected during the test run (black points, with error bars), accidental coincidence events (blue short-dash line), and the QED calculation of trident background added to the accidental event sample (red long-dash line).

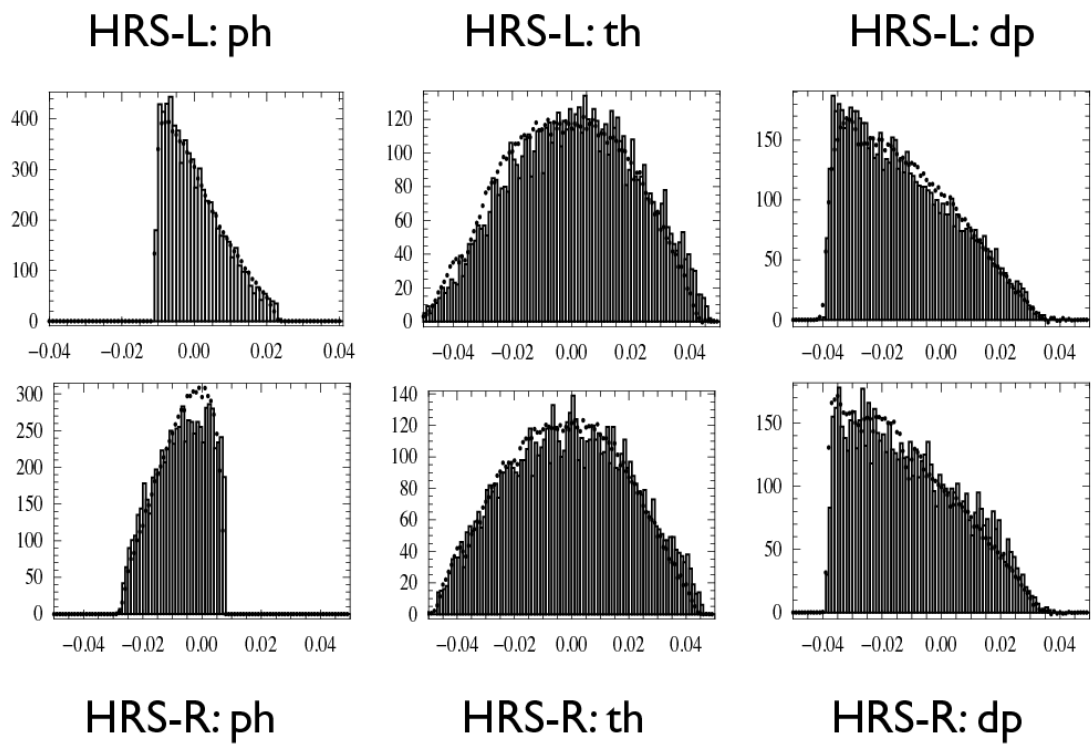


FIG. 7.11: Angular and δp distributions of the Monte Carlo simulations (histogram) and the test run data (black dots).

7.6 Mass Resolution

The uncertainty of the A' invariant mass can be calculated using the uncertainty principle in the form $\delta E \delta t > \frac{\hbar}{2}$, where δt is taken to be the lifetime of the particle. The ranges of ϵ and $m_{A'}$ explored by APEX correspond to an invariant mass uncertainty that is much smaller than the mass resolution achievable by the experiment [20]. Therefore, the width of the A' resonance will be equal to the experimental mass resolution.

Determining the mass resolution is essential to understanding the sensitivity of the peak search. The invariant mass of e^+e^- pairs can be calculated to leading order according to

$$m^2 \approx p_0^2(4\theta_0^2 + 4\theta_0^2\delta_+ + 4\theta_0^2\delta_- + 8\theta_0(\phi_+ - \phi_-) + 2\theta_+\theta_-), \quad (7.13)$$

where p_0 is the central momentum setting of both HRSs, θ_0 is the angle between the beamline and the central trajectory of the spectrometer, δ_{\pm} is the relative momentum, ϕ_{\pm} is the horizontal angle, θ_{\pm} is the vertical angle, and all variables are in the target coordinate system. Due to the excellent HRS relative momentum resolution of $\mathcal{O}(10^{-4})$, the mass resolution is completely dominated by the horizontal and vertical angular resolutions.

7.6.1 Angular Resolution

The angular resolution can be broken up into 3 separate parts: multiple scattering inside of the target, track measurement errors by the HRS detectors, and imperfections in the magnetic optics reconstruction matrix. We will discuss the calculation of all three contributions and how each affects the final mass resolution.

Multiple Scattering in the Target

When traveling through a medium electrons and positrons experience many small angle deflections due to Coulomb scattering from nuclei. The resulting angular distribution from this multiple scattering is given by [44]

$$\Omega = \frac{13.6 \text{ MeV}}{p} \sqrt{\frac{X}{X_0}} \left(1 + 0.038 \ln \frac{X}{X_0}\right) \quad (7.14)$$

where p is the particle momentum, x is the target thickness, and x_0 is the radiation length of the target material. The tantalum foil target used during the test run has a thickness of 22 mg/cm^2 , or $0.0032X_0$. This target thickness leads to a 0.37 mrad contribution to the uncertainty in both horizontal and vertical angles.

Track Measurement Errors and Imperfections in the Optics Matrix

To calibrate the magnetic optics matrix elements, data was taken with a tungsten sieve plate inserted at the entrance of each spectrometer, as discussed in Sec. 6.3.3. The sieve plates each have a grid of holes drilled through them with known positions and widths. When electrons scatter from the target toward the

spectrometer only electrons with trajectories passing directly through the sieve holes will be detected. Therefore, the reconstructed trajectories of the electrons projected at the sieve plane should resemble the sieve hole pattern. The reconstruction of the holes can be compared with the surveyed locations and widths of the holes to determine the track measurement errors of the HRS and the imperfections in the final optics reconstruction matrix.

The x and y distributions of each hole were plotted and fit with a Gaussian on top of a linear background (Fig. 7.12). The reconstructed positions and widths of each hole were extracted from the fit and compared with the surveyed hole positions and widths. The track measurement uncertainty of the HRS detectors was determined by comparing the reconstructed and surveyed hole widths:

$$\Delta_{\sigma_x}^2 = \sigma_{x_{\text{reconstructed}}}^2 - \sigma_{x_{\text{surveyed}}}^2, \quad \Delta_{\sigma_y}^2 = \sigma_{y_{\text{reconstructed}}}^2 - \sigma_{y_{\text{surveyed}}}^2. \quad (7.15)$$

The imperfections of the optics reconstruction matrix were determined by comparing the reconstructed and surveyed hole positions:

$$\Delta_x = x_{\text{reconstructed}} - x_{\text{surveyed}}, \quad \Delta_y = y_{\text{reconstructed}} - y_{\text{surveyed}}. \quad (7.16)$$

These results were converted into angular uncertainties by dividing them by the distance to the center of the target, D_{target} and taking the inverse tangent:

$$\phi = \arctan \frac{x}{D_{\text{target}}}. \quad (7.17)$$

Table 7.2 summarizes the contributions to the angular resolution averaged over all sieve holes located within the calibrated acceptance.

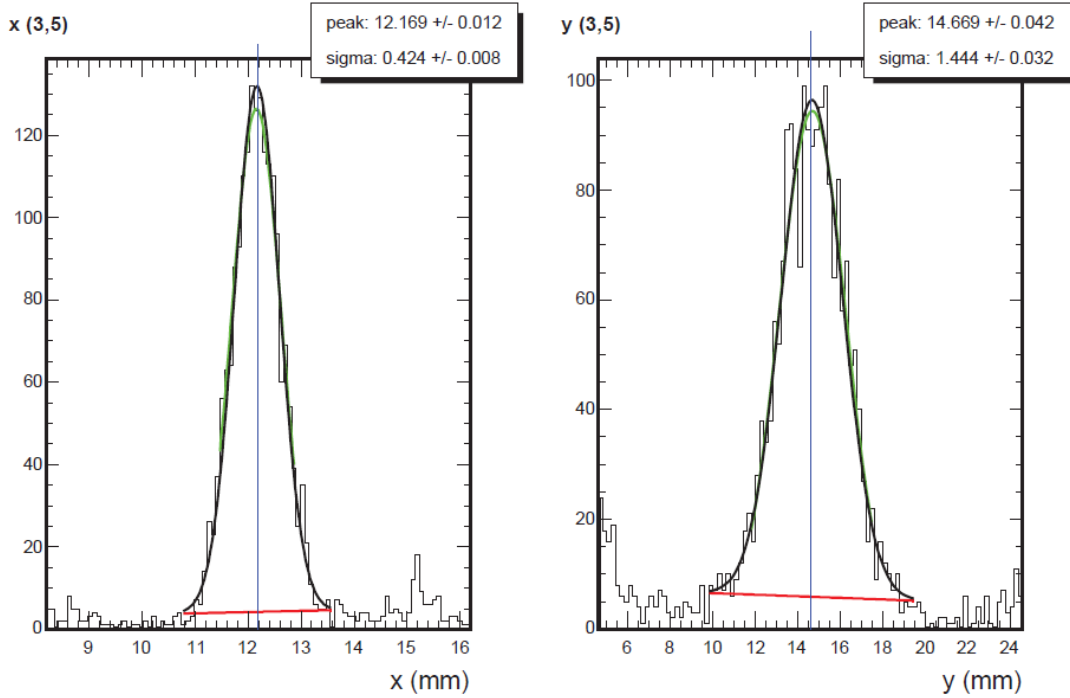


FIG. 7.12: The x and y distributions for a single sieve hole. The distributions were fit with a Gaussian (black) on top of a linear background (red). The blue line indicates the surveyed location of the hole. The peak and sigma of the fit correspond to the reconstructed position and width of the hole.

7.6.2 Determining the Mass Resolution

In this section we will discuss the procedure used to determine the mass resolution of the APEX test run. The first step is to simulate a new invariant mass spectrum by adjusting existing data according to the angular resolutions of the experiment. The simulation was done using real events from a single production run.

TABLE 7.2: Summary of the contributions to the angular resolution averaged over all sieve holes located within the calibrated acceptance.

	Left-HRS		Right-HRS	
	Track reconst. errors	Optics matrix imperf.	Track reconst. errors	Optics matrix imperf.
Horizontal (mrad)	0.33	0.1	0.43	0.1
Vertical (mrad)	1.85	0.22	1.77	0.22

For each event the horizontal and vertical components of the trajectories were randomly adjusted. More specifically, a new angle was randomly selected according to a Gaussian distribution centered at the real angle for that event and with a σ equal to the angular resolution. The angular resolution was determined for each sieve hole individually, so the angular resolution associated with the hole located closest to the particle's trajectory was used in generating the new angle (multiple scattering was also included). After the new angles were generated a new invariant mass was calculated for that event.

After simulating new invariant masses for all events, the difference between the fake mass and real mass was plotted in a histogram (Fig. 7.13). The RMS value of the resulting distribution corresponds to the mass resolution of the experiment. Finally, the mass resolution was determined for different values of invariant mass. Fig. 7.14 shows how the mass resolution varies with invariant mass. The resulting fit function is

$$f(x) = -0.0001x^2 + 0.058x - 5.3961, \quad (7.18)$$

where x is the invariant mass. This equation was used in the peak search, the details of which are discussed in Ch. 8.

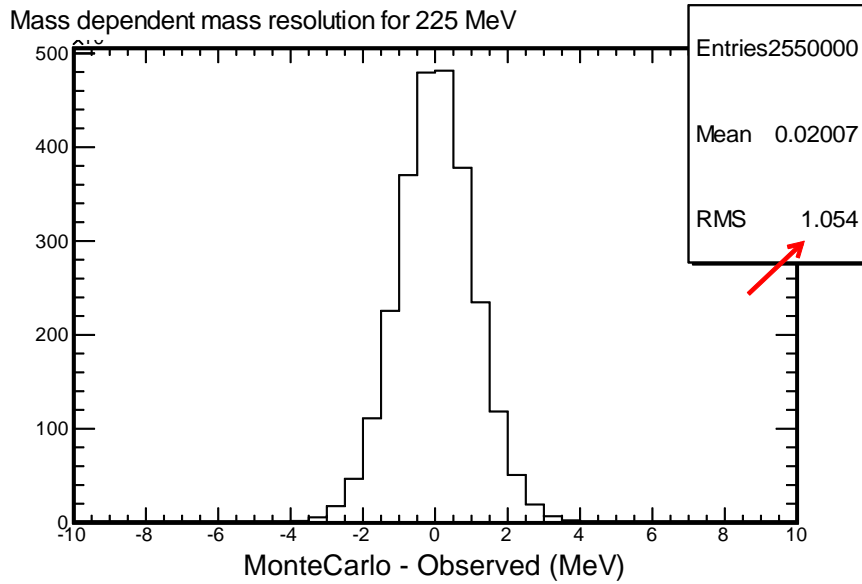


FIG. 7.13: New invariant masses were simulated by adjusting real data to the angular resolutions of the experiment. The differences between the simulated masses and real masses are shown in the histogram. The RMS of this distribution corresponds to the mass resolution of the experiment.

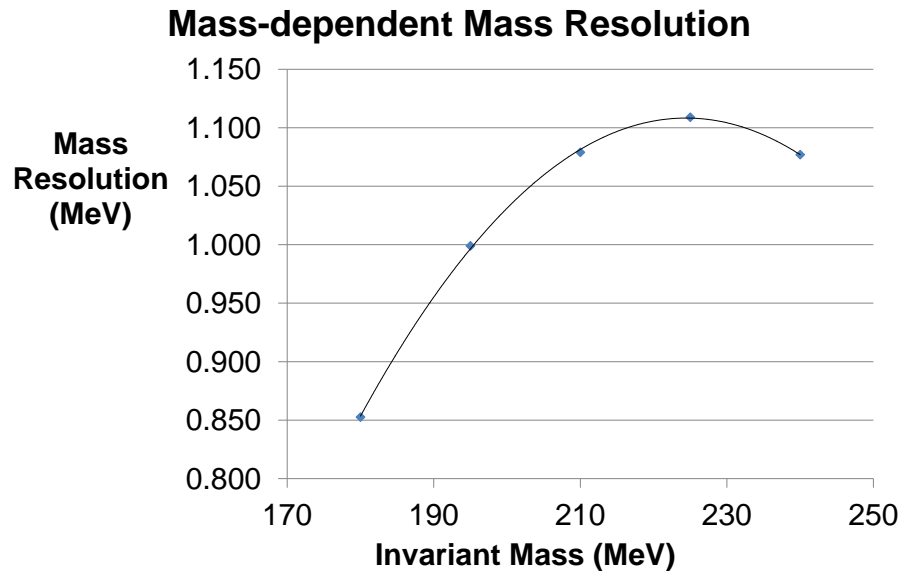


FIG. 7.14: The mass resolution as a function of invariant mass. The resulting fit function was used in the final peak search.

7.7 Addressing the PAC Concerns

The purpose of the APEX test run was to address several concerns expressed by the PAC35 about the experiment’s proposal. In this section we will present the results of our investigation of the issues raised by the PAC35 report. These results were also discussed at the “Searching for a New Gauge Boson at JLab” workshop [31].

The Multi-foil Target

The multi-foil target has a superior design over the wire-mesh target presented in the original proposal. The details of the multi-foil target are discussed in Sec. 4.4.1. The target was constructed and shipped to Jefferson Lab, although it was never installed due to time constraints.

The z vertex resolution achieved during the Pentaquark experiment was 1.1 cm [40]. This resolution would be sufficient for resolving the production target foils, which are separated by 5.5 cm along the beam line.

Central Scattering Angle

Fine resolution of the e^+e^- invariant mass is required to achieve a high precision search for the A' . The resolution of the invariant mass measurements is dominated by the horizontal angular resolution which has contributions coming from multiple scattering in the target, uncertainties in the track reconstruction by the HRS detectors, and imperfections in the optics reconstruction matrix. Multiple

scattering in the target contributes $\sim 0.4/p[\text{GeV}]$ mrad in each HRS with a spectrometer setting of p , contributing ~ 0.5 MeV to the mass resolution. The second and third contributions combined give an uncertainty of ~ 0.5 mrad in each HRS, and contributes $0.7 \text{ MeV} \cdot p[\text{GeV}]$ to the mass resolution.

Due to the high momentum resolution of the HRS, particle momenta are measured to within 10^{-4} . A fractional momentum resolution of 5×10^{-4} only contributes $0.07 \text{ MeV} \cdot p[\text{GeV}]$ to the mass resolution, which is considered negligible. The 1 mrad uncertainty in vertical angles also only contributes $0.12 \text{ MeV} \cdot p[\text{GeV}]$ to the mass resolution.

The position of the spectrometers defines the absolute scale of the e^+e^- pair invariant mass, but has a small effect on the event-by-event mass resolution. A Monte Carlo simulation was done to determine what effect the uncertainty in the angle between the spectrometers would have on the mass resolution. The simulation demonstrated that a 1 mrad uncertainty would only contribute 8×10^{-5} to the event-by-event invariant mass resolution.

VDC Operation at High Rates

For the proposed experiment the VDCs must be capable of operating at a maximum rate of 5 MHz. Such high rate operation was made possible by utilizing the custom amplifier/discriminator cards described in Sec. 4.4.3. These A/D cards allow the VDCs to operate at -3.5 kV instead of -4 kV. Operating at a reduced voltage allows long term operation while still using the standard VDC gas mixture.

The custom A/D cards were installed during the test run and data was taken using a lead target in order to achieve VDC rates up to 5 MHz.

The VDC wire efficiency during high rate data taking was checked during the test run. For every event, all wires in a given VDC plane are scanned. Events are identified where two wires in the plane fire and a third wire is between them. If the third wire also fires, the event is defined to be efficient. An example of the VDC wire efficiency of a single VDC plane for high rate data is shown in Fig. 7.15. The drift time distribution during high rate data taking exhibited a normal profile, as shown in Fig. 7.16. Also, the drift time to coordinate calibration is the same for low and high rate data, as shown in Fig. 7.17. We observe a small reduction in cluster size at high rates (Fig. 7.18), which is due to reduced efficiency. Finally, the test run demonstrated a track reconstruction efficiency of $\sim 60\%$ for high rate operation.

π^+ Rejection at High Rates

The Right-HRS GC detector is used in the trigger to provide on-line π^+ rejection. To study the GC pion rejection efficiency at high rates, data was taken with a $30 \mu\text{A}$ electron beam incident on the lead target described in Sec. 5.2.1. The Right-HRS trigger rate for this data was ~ 765 kHz (85 kHz positrons and 680 kHz meson background). Fig. 7.19 shows the GC amplitude spectrum for the high rate data. Just as before, the sharp peak on the left contains meson background whereas the distribution that follows contains positrons. The red and blue distributions correspond to the meson background and e^+ samples, respectively, as determined by the

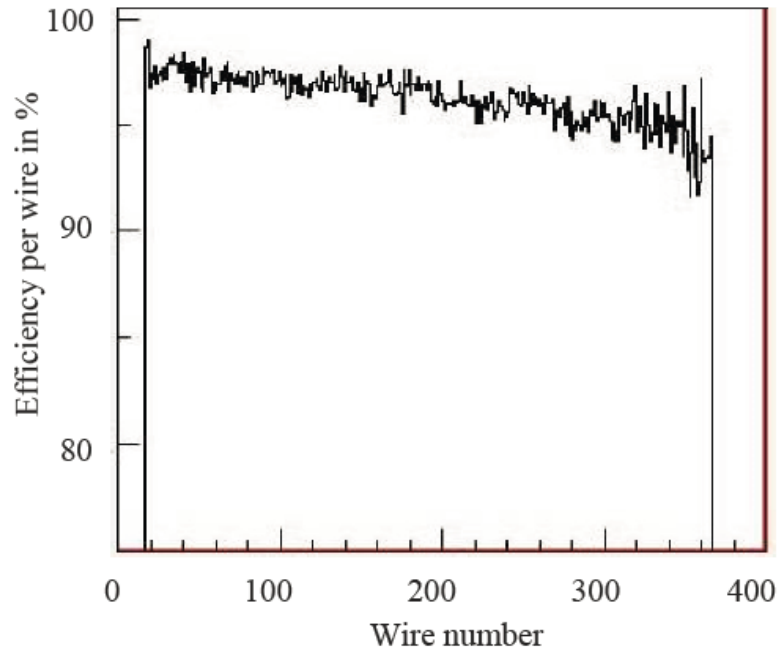


FIG. 7.15: The VDC wire efficiency for a single plane for high rate data. Events are identified where two wires fire and a third wire is between them. If the third wire also fires, the event is considered efficient. Otherwise the event is defined as inefficient.

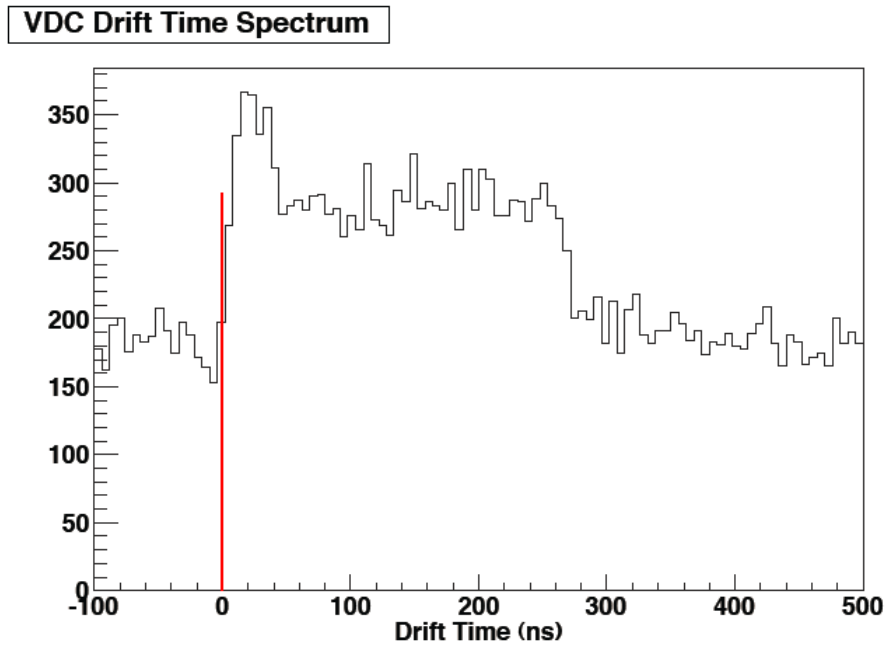


FIG. 7.16: An example of the VDC drift time during high rate operation.

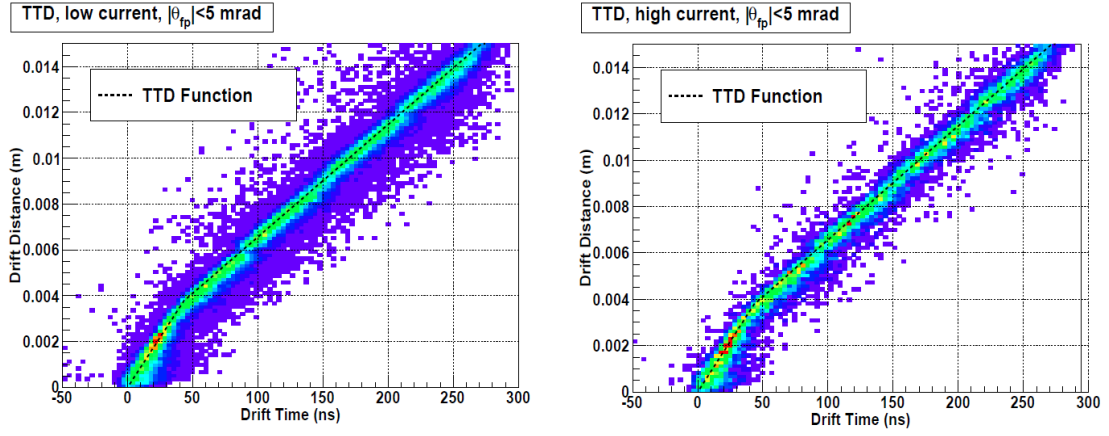


FIG. 7.17: The VDC drift time-to-distance calibration. There are no serious differences between high and low rate data.

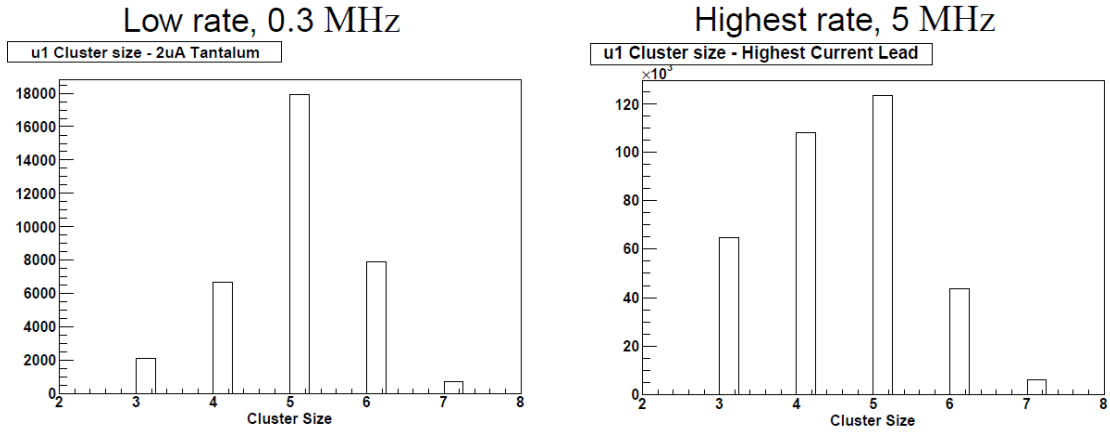


FIG. 7.18: Cluster sizes for low and high rate data. We observe a reduction in cluster size for high rate data due to reduced efficiency.

LG. The pion rejection efficiency of the GC was determined using the same method described in Sec. 7.2. Using this analysis we obtain an on-line meson background rejection factor of 30 for data taken at close to the expected maximum rate.

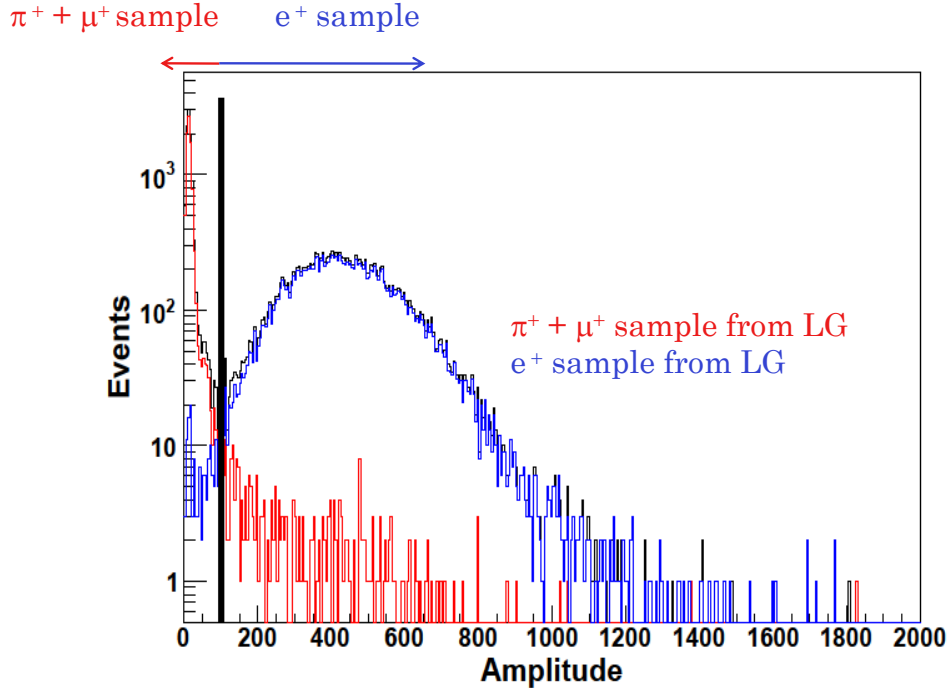


FIG. 7.19: The Right-HRS gas Cherenkov amplitude spectrum at a track rate of 750 kHz. At this rate the pion rejection factor is 30, which is sufficient for the reduction of the DAQ rate.

Coincidence Timing Window

For high rate data taking it is important to have a small coincidence timing window in order to minimize the DAQ dead time and avoid recording excess accidental coincidence events. The APEX test run used a trigger consisting of a coincidence between the two S2m scintillator planes and the GC of the positron arm (Sec. 5.3).

Both S2m planes produced 20 ns signals while the GC produced 10 ns signals. The overlap of these three signals provides a coincidence timing window of 40 ns. The S0 counters of each arm were used to align the average timing of the S2m and GC signals. This fine tuning allowed us to produce a 15 ns wide timing peak consisting of true coincidence events, as shown in Fig. 7.2b. This demonstrates the possibility of implementing a 15 ns coincidence timing window without losing true coincidence data.

Septum Magnet Field

The test run demonstrated that the septum magnet provides the required field uniformity when used to bend 1.13 GeV particles to 5° . The highest-energy configuration for APEX (4.46 GeV) requires bending of 2.23 GeV particles to 5.5° . A new septum magnet is currently being designed for Hall A experiments and will provide a uniform magnetic field under such a configuration [45].

Backgrounds

The A' will appear as a narrow resonance on top of a smooth QED background distribution. The QED background will consist primarily of e^+e^- pairs produced through bremsstrahlung radiation of virtual photons. The signal to background ratio is not reducible but defined by the ratio of coupling constants, $\alpha'/\alpha_{\text{fs}}$. Any additional contributions to the background, physics or accidental, lead to a relatively small loss in the experiment's sensitivity as long as their rates are only a fraction

of the QED pair production rate. The amount of additional background present in the final test run data sample was calculated in order to understand its impact on the sensitivity of the A' search.

The GC detectors in both spectrometers were used to determine how much meson background was present in the final data sample. Events with a GC amplitude (sum of all 10 PMTs) less than 100 ADC counts are considered to be meson background. The final data sample contains only 0.9% meson background contamination, the majority of which is made of $e^+\pi^-$ events. The accidental background was estimated using the coincidence timing spectrum shown in Fig. 7.2b. True coincidence events were selected by making a 12.5 ns cut centered about the peak. Events outside of this 12.5 ns window are considered to be accidentals. Using this coincidence time spectrum we find that 7.4% of the final event sample is made of accidental coincidence events.

8

Resonance Search and Results

The analysis of the APEX test run data yields an invariant mass spectrum of e^+e^- pairs. This mass spectrum provides the starting point for the $A' \rightarrow e^+e^-$ search. The next steps are to search the mass spectrum for a resonance and, if a resonance is not found, set an exclusion limit on the coupling α' . In this chapter we will describe the procedure used to search for peaks in the spectrum and quantify both the significance of any observed peaks and the exclusion power of the experiment. The entire APEX collaboration contributed to the resonance search analysis. The final results of the search will be presented at the end of the chapter.

8.1 Searching for a Resonance

An A' signal would appear as a Gaussian peak on top of a polynomial background distribution. The signal would have an unknown height and width σ equal

to the experimental mass resolution. The general idea behind the A' resonance search is to scan the entire e^+e^- invariant mass spectrum searching for a significant number of signal events at each mass hypothesis. The search is performed by constructing a fixed size window centered around the mass hypothesis m . The data in this window is fit with a polynomial plus a Gaussian centered at m with a width σ equal to the experimental mass resolution. The polynomial coefficients and the normalization of the Gaussian are free parameters chosen to maximize the Poisson likelihood of the data (see Sec. 8.1.2).

The significance of a resonance can be formulated in terms of the probability that the resonance could be observed by accident, in other words, the probability that such a resonance can be observed due to statistical fluctuations. To determine this probability a series of pseudo-experiments are performed on background-only Monte Carlo data sets. These data sets are independently generated based on the simulations described in Sec. 8.1.1. To quantify the significance of an observed signal we use a quantity known as a p -value. The p -value is the probability that an experimental observation agrees with the null hypothesis (no signal present). Observing a large signal would have small agreement with the null hypothesis, and thus give a small p -value. For example, if an observed signal has a p -value p_{obs} , and a p -value that is less than or equal to p_{obs} is observed in 50% of the background-only pseudo-data sets, then there is a 50% chance of accidentally producing such a signal through statistical fluctuations and it should not be considered as evidence of new physics.

Often in physics the statistical significance of a result is given in terms of the standard deviation σ of a normal distribution. A normal distribution and integer multiples of σ are shown in Fig. 8.1. The number of sigmas measures the probability of observing the same result by chance. This probability is obtained by integrating the normal distribution from $n\sigma$ to infinity. For example, a 3σ signal would have a 1.35×10^{-3} chance of occurring due to statistical fluctuations. So in our case, a 3σ evidence would require that such an observed signal only occur with a frequency of 1.35×10^{-3} in the background only pseudo-data sets.

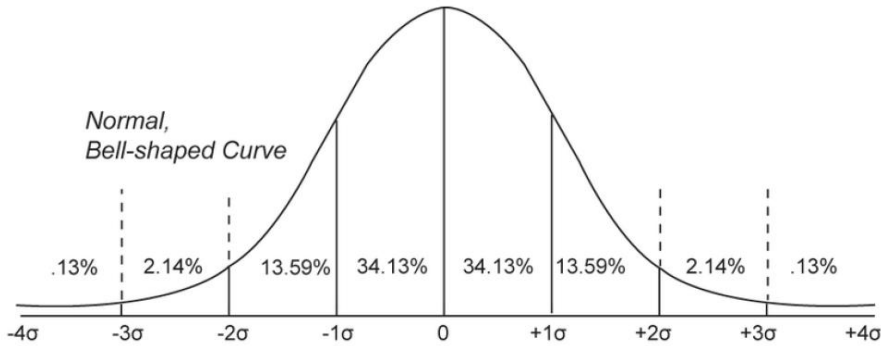


FIG. 8.1: A normal distribution with integer multiples of the standard deviation σ shown. The statistical significance of a result is often given in terms of the number of standard deviations, $n\sigma$. The probability of producing a result by chance is found by integrating the normal distribution from $n\sigma$ to infinity. These probabilities are shown up to 3σ .

8.1.1 Pseudo-data Sets

The pseudo-data sets were generated from the “toy function”

$$\frac{(170 - m)^2(265 - m)^2}{m^4} \quad (8.1)$$

between 171 and 264 MeV (Fig. 8.2). Each bin of a data set was filled according to independent Poisson distributions with expectation values given by the function above scaled to provide a total of 7×10^5 events. Pseudo-data sets with signals were also created using the same procedure with signal events generated according to a Gaussian probability distribution function (PDF).

Additional studies were done using pseudo-data sets that were generated using a simulated QED trident mass spectrum, and also on a 10% sample of the experimental data to avoid possible bias [17].

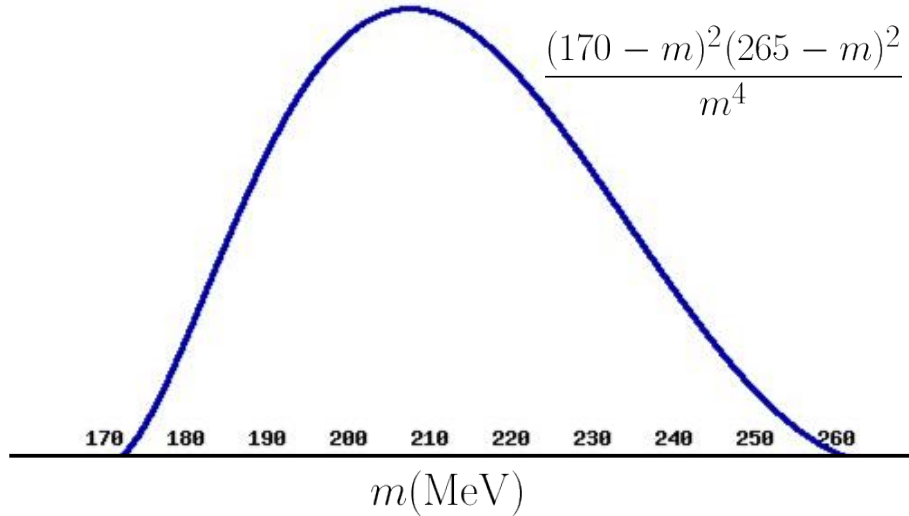


FIG. 8.2: The “toy function” used to generate pseudo-data sets.

8.1.2 Profile Likelihood Ratio

For a fixed A' mass $m_{A'}$, the distribution of events can be modeled using the probability distribution

$$P(m_{e^+e^-}) = \frac{1}{S + B} (S \cdot \text{N}(m_{e^+e^-} | m_{A'}, \sigma) + B \cdot \text{Polynomial}(m_{e^+e^-}, a_i)), \quad (8.2)$$

where $m_{e^+e^-}$ is the invariant mass of the e^+e^- pair, S is the number of signal events, B is the number of background events, N is a normal (Gaussian) probability distribution, and the background shape is given by a polynomial with coefficients a_i .

This probability function becomes a likelihood function, L , as a function of the model parameters. To test a hypothesized value for S against alternatives, we use the profile likelihood ratio (PLR) [46]

$$\lambda(S) = \frac{L(S, \hat{B}, \hat{a}_i)}{L(\hat{S}, \hat{B}, \hat{a}_i)}. \quad (8.3)$$

In the numerator, \hat{B} and \hat{a}_i are the values of B and a_i that maximize L for the assumed S . In other words, \hat{B} and \hat{a}_i are *conditional* Maximum Likelihood Estimators (MLEs) and consequently are functions of S itself. The denominator, instead, is maximized to best fit the data without any constraints on S , thus \hat{S} , \hat{B} , and \hat{a}_i are the *unconditional* MLEs. When the hypothesized S coincides with \hat{S} , the PLR goes to 1, thus showing great compatibility between the data and the

hypothesis. If S does not agree with \hat{S} , the PLR goes to 0, thus showing a high degree of incompatibility between the data and hypothesis.

The Wilks' theorem states that under the null hypothesis, or $S = 0$, the log-likelihood ratio $t = -2 \ln \lambda(S)$ is distributed according to a χ^2 function with the number of degrees of freedom equal to the number of parameters of interest, which in our case is the one parameter S [47]. Because of its χ^2 distribution under the null hypothesis, the quantity t can be used as a test statistic to either claim discovery of a new signal or to put an upper limit on the case of the absence of a signal.

For example, if we want to establish an upper limit at 90% confidence, a threshold is set so that the integral of the null hypothesis probability distribution function (PDF) from 0 to the threshold is 0.90. Then for a given experimental outcome, the value of t is calculated for the observed data. If t is found to be equal to or greater than the threshold, the presence of a signal is excluded at a level equal to or greater than 90%.

The observed test statistic t_{obs} can be translated into a p -value using

$$p = \int_{t_{obs}}^{\infty} f(t) dt, \quad (8.4)$$

where $f(t)$ is the probability distribution function of t . Fig. 8.3 illustrates the relation between the p -value obtained from the observed t as well as its relation to the significance Z .

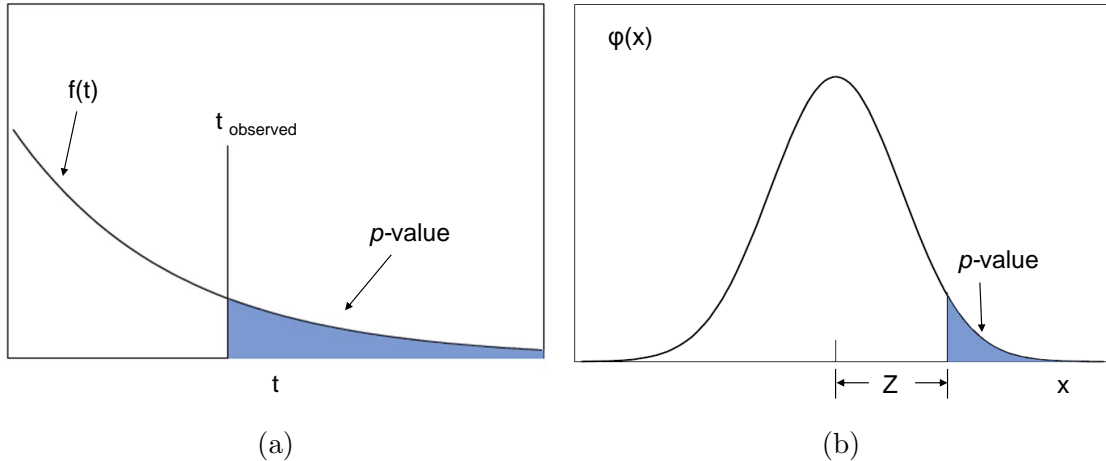


FIG. 8.3: (a) The relation between the p -value and PDF of the test statistic $f(t)$. The p -value is obtained from the observed value of the test statistic t_{observed} . (b) The standard normal distribution showing the relation between the p -value and the significance Z .

8.1.3 The Look Elsewhere Effect

When testing the background-only (null) hypothesis it is possible for a large statistical fluctuation to mimic a signal. Furthermore, when scanning a wide mass range for a resonance it is possible for such statistical fluctuations to occur anywhere within the mass range. Thus the probability of observing an accidental signal increases significantly. This phenomenon is known as the “Look Elsewhere Effect” (LEE). Take, for example, a mass range consisting of a single bin. If we perform 100 pseudo-experiments and find S signal events in 10 of them, then there is a 10% chance of observing such a signal from statistical fluctuations. Now let’s take a mass range consisting of 10 bins. For simplicity, let’s assume that each bin has a 10% chance of producing S signal events. The probability of observing an accidental signal somewhere in the 10 bin spectrum would be 100%.

One simple way of accounting for the LEE is to scale the lowest p -value ob-

tained from the data by a “trials factor”, which is the ratio between the probability of observing a signal at some fixed mass point to the probability of observing it anywhere in the range. This scaling can be quantitatively expressed as

$$p \rightarrow p \times \frac{\text{massrange}}{\text{massresolution}}. \quad (8.5)$$

This is equivalent to requiring a smaller threshold for the uncorrected p -value when claiming evidence of new physics. In reality, the “trials factor” is only a first order correction and is too crude for determining a threshold for the smallest p -value with good accuracy.

Another solution is to run many pseudo-experiments on the background-only Monte Carlo data sets described in Sec. 8.1.1 and find for each one the fluctuation resulting in the lowest p -value. For 3σ evidence of an A' signal, a p -value less than or equal to the threshold should only be observed with frequency 1.35×10^{-3} . Using this method would yield the right answer; however, obtaining the correct threshold with any accuracy would require a very large number of pseudo-experiments. Instead, the method described in [48] was used to obtain a threshold. This method only requires a modest number of pseudo-experiments. The lowest p -value from each pseudo-experiment is ranked, and the estimated quantile is obtained by dividing the rank by the total number of pseudo-experiments performed plus one. The p -values are then plotted versus their respective quantile. Fig. 8.4 shows an example of such a plot containing data from 7500 pseudo-experiments. In this example the p -value for 3σ significance is around 10^{-5} .

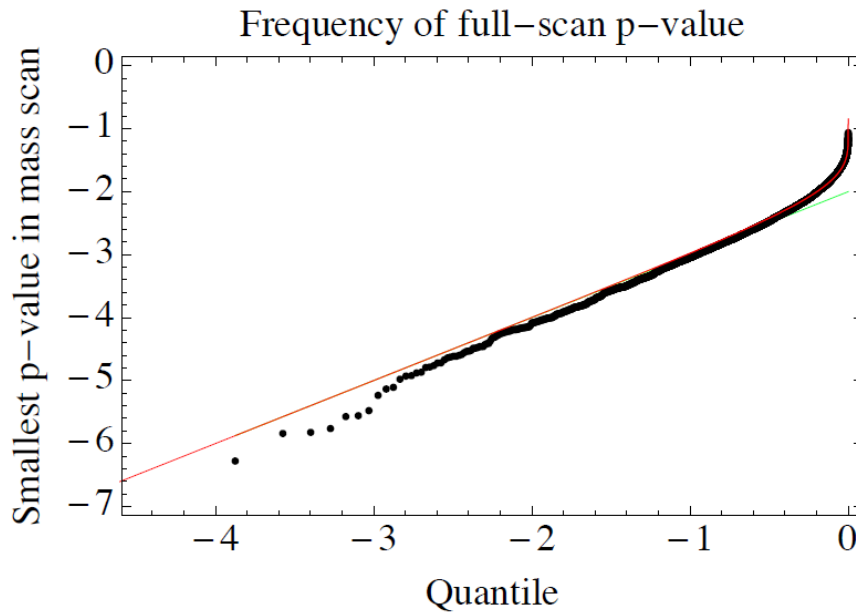


FIG. 8.4: An example of limit setting on the lowest observed p -value. Full mass scans were performed on 7500 pseudo-data sets. The lowest p -value was obtained from each mass scan and ranked. The quantile of each pseudo-experiment was calculated by dividing the rank by the (total number of pseudo-experiments performed + 1). This plot shows the p -value vs. quantile for all 7500 mass scans. The numbers on the axes are exponents. From this plot we find that a signal with 3σ significance, or occurring with a frequency of 1.35×10^{-3} from statistical fluctuations, would require a p -value of $\sim 10^{-5}$.

8.1.4 Search Parameters

Before performing the resonance search some search parameters must be optimized. These parameters include the size of the invariant mass binning, the fitting window size, and the order of the polynomial in the fit function. The search parameters were tested on the pseudo-data sets described in Sec. 8.2 in order to find values for the parameters that maximize the sensitivity of the search while also minimizing systematic pulls. The parameters were also tested on a 10% sample of the experimental data that was scaled up in order to avoid potential bias.

Mass Binning

Ideally the peak search would be performed using an unbinned mass spectrum. Due to the large number of statistics, however, this would be intractably time consuming. A binned analysis is much more manageable and any systematic pulls due to choice of statistical tool (ROOT, Mathematica, etc.) can be made negligible by choosing small enough bins.

The systematic pull was calculated for pseudo-data sets using

$$\text{Pull} = \frac{S_{\text{bestfit}} - S_{\text{inserted}}}{S_{\text{error,fit}}}. \quad (8.6)$$

The pulls were calculated for several different bin sizes. The pull distributions for 0.5 MeV and 0.05 MeV bin sizes are shown in Fig. 8.5. We found that when $S_{\text{inserted}} = 0$ the average pull generated using a bin size of 0.05 MeV was ~ 100

times smaller than when using a bin size of 0.5 MeV. A bin size of 0.05 MeV was used in the final analysis.

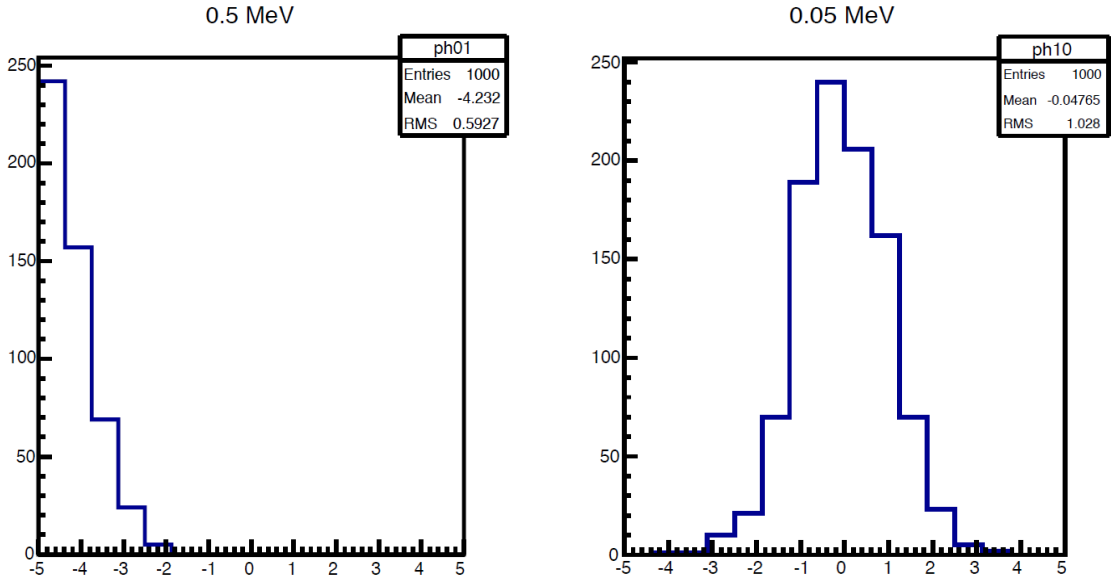


FIG. 8.5: Pulls generated for pseudo-data sets when $S_{\text{inserted}} = 0$. The pull is calculated using $\text{Pull} = \frac{S_{\text{bestfit}} - S_{\text{inserted}}}{S_{\text{error,fit}}}$. An average pull of -4.232 is generated for 0.5 MeV binning (left) and -0.048 for 0.05 MeV binning (right).

Polynomial Order and Window Size

To search for the A' , a polynomial background model plus a Gaussian signal is fit to a window centered about each candidate A' mass. The uncertainty in the polynomial coefficients corresponds to the uncertainty in the shape of the background model. To optimize the sensitivity of the resonance search the uncertainty in the shape of the background model must be minimized. Extensive tests were done on

pseudo-data sets to determine which window size and order of polynomial optimized the sensitivity of the search while also minimizing systematic pulls.

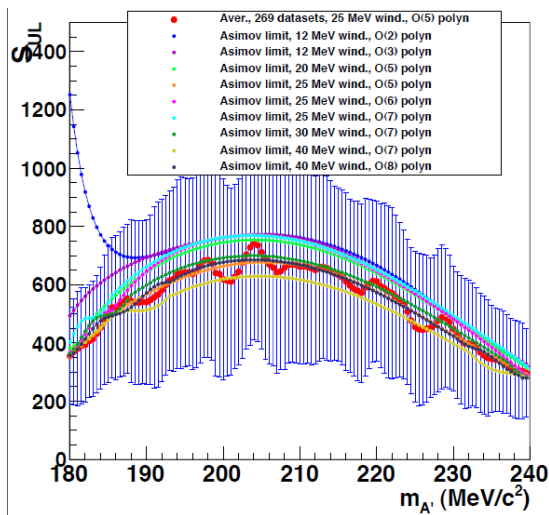
Fig. 8.6 shows results of tests that were done using several different values of polynomial order and window size. Fig. 8.6a demonstrates the upper limit on the number of signal events allowed for the null hypothesis to hold true. Fig. 8.6b shows the systematic pulls generated by each test case. It was found that a 30.5 MeV window with 7th order polynomial (dark green line) optimized between sensitivity in S and minimal pull. The window is centered about each mass candidate, except for masses within 15 MeV of the edge of the spectrum, for which a window of equal size touching the boundary is used. The fit is repeated across the mass spectrum in steps of 0.25 MeV.

8.1.5 Results

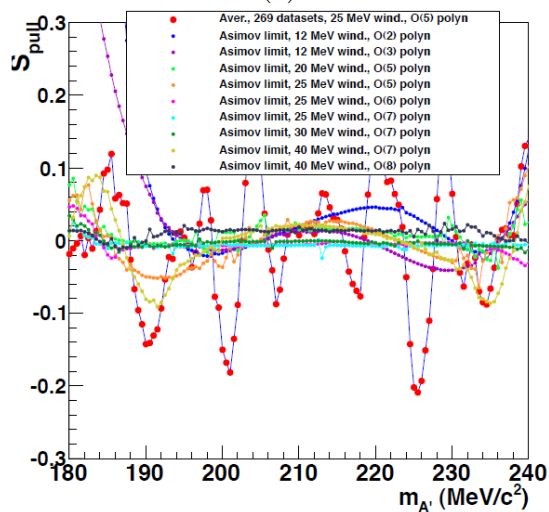
The results of the resonance search show no evidence of an A' signal in the mass range of 175-250 MeV. The most significant signal found 224.5 MeV has a local p -value of 0.6% (see Fig. 8.7). After correcting for the LEE the associated global p -value is 40%, meaning that 40% of the background-only pseudo-experiments resulted in more significant signals due to statistical fluctuations.

8.2 Setting Limits on $\alpha'/\alpha_{\text{fs}}$

The second part of performing the A' search is setting a limit on the coupling α' . The goal is to translate the upper limit on the number of signal events S



(a)



(b)

FIG. 8.6: Different combinations of polynomial order and window size are tested in order to optimize between sensitivity in S and minimal pull. (a) shows the upper limit on the number of signal events S allowed for the null hypothesis to hold true. (b) shows the average pulls generated by the different combinations.

into a limit on α' . If α' is extremely small, the A' production cross section will also be small and the number of observed signal events will be reduced. Statistical fluctuations may then mask the presence of a true A' signal. To search for A' s with smaller couplings we must increase the number statistics collected during the experiment, thus reducing the size of the statistical fluctuations. By collecting more statistics we extend the experimental reach to smaller values of α' . A large number of signal events observed at m_{hyp} might not be large enough to show evidence of an A' signal if there is a significant probability of producing such a signal through statistical fluctuations. This doesn't mean that an A' with mass m_{hyp} does not exist. The A' could have a very small coupling, thus masking the "true" signal with statistical fluctuations. In such a case the number of observed signal events translates into a limit on α' that can be excluded. The existence of an A' with α' smaller than this limit would not be excluded.

As discussed in Sec. 4.2 we use a ratio method that normalizes A' production to the measured QED trident rate to minimize systematic uncertainty from acceptance and trigger efficiencies. Using this method we will set an upper limit on α'/α_{fs} using the equation

$$\left(\frac{\alpha'}{\alpha_{fs}}\right)_{\max} = \left(\frac{S_{\max}/m_{A'}}{f B/\delta m}\right) \times \left(\frac{2N_{\text{eff}}\alpha_{fs}}{3\pi}\right), \quad (8.7)$$

where N_{eff} is the number of possible decay channels ($N_{\text{eff}} = 1$ for $m_{A'} < 2m_{\mu}$, and increases to $\simeq 1.6$ at $m_{A'} \simeq 250$ MeV), f is the ratio of the radiative-only cross section to the full trident cross section (varies linearly from 0.21 to 0.25

across the APEX mass range), S_{\max} is the upper limit on the number of signal events observed at $m_{A'}$, and $B/\delta m$ is the number trident background events observed per unit mass evaluated in a 1 MeV range around $m_{A'}$.

8.2.1 Setting Limits on S

The number of observed signal events S is determined using the PLR method described in Sec. 8.1.2. This method finds the value of S that best fits the data. The log-likelihood ratio is used to calculate the corresponding p -value, which is then corrected for the LEE. If the p -value does not show evidence of an A' signal, then we set a limit on α' using the upper limit of S . The 2σ (90% confidence) upper limit of S is derived by setting the p -value to 0.1 and then inverting the PLR to solve for S_{\max} . The LEE does not need to be accounted for when deriving S_{\max} .

The statistical fluctuations that produce artificial signals can also have the opposite effect, resulting in flat or negative signals. Regions of the mass spectrum where the best fit results in a value of S that is equal to or even less than zero would result in the exclusion of all possible values of α' according to Eq. 8.7. As a result, these regions lack sensitivity in the search for a signal. To avoid completely excluding such regions we use a 50% power-constrained limit on S [49]. For each mass candidate there is an associated S_{median} , which is the median value of the 2σ limit of signal events observed for all pseudo-experiments. If $S_{\max} < S_{\text{median}}$ (the observed upper limit is less than the pseudo-experiment median upper limit) then the resonance search is said to have insufficient signal sensitivity for that mass

candidate. In such a case, S_{median} is used instead of S_{max} .

8.2.2 Results

The middle section of Fig. 8.7 shows the 2σ upper bound on the absolute yield of $A' \rightarrow e^+e^-$ signal events across the A' mass spectrum. The red line shows the best fit of S . The shaded grey region denotes the 2σ upper limit with 50% power-constraint. The expected limit (S_{median}) is denoted by the dashed grey line. The solid (dotted) blue line shows the 2σ limit when it is above (below) the expected limit. For comparison, the dot-dashed line shows the expected limit if the background shape were known exactly, i.e. if the polynomial coefficients were fixed. This illustrates the contribution of statistical uncertainty to the expected limit.

The resulting 2σ limit on $\alpha'/\alpha_{\text{fs}}$ is shown in blue in Fig. 8.8. The small gaps are associated with the larger signal excesses that were observed in the data. Also shown is the existing 2σ exclusion from the muon anomalous magnetic moment a_μ (fine hatched) [50], KLOE (solid gray) [16], the result reported by Mainz (green) [18], and an estimate using a BaBar result (wide hatched) [19]. The full APEX experiment will roughly cover the entire area of the plot.

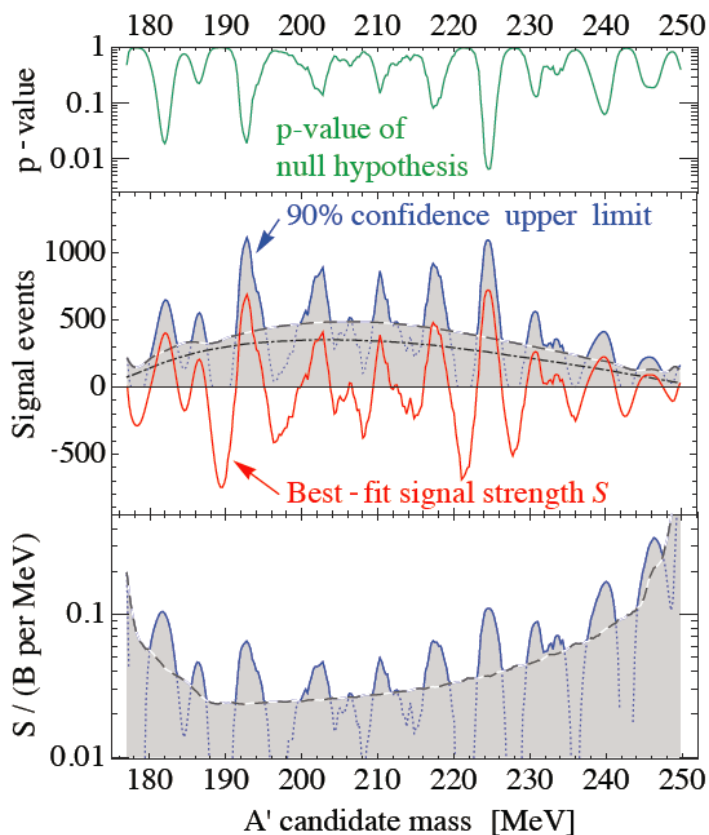


FIG. 8.7: *Top:* Local p -value versus A' mass. *Middle:* The 2σ upper limit on signal events. The shaded grey region shows the 50% power-constrained region. The red line denotes the best fit on the number of signal events. The expected limit is shown by the dashed line. The blue solid (dotted) line denotes the 2σ upper limit when it falls above (below) the expected limit. To illustrate the contribution from statistical fluctuations, the dot-dashed line shows the expected limit if the background shape were known exactly. *Bottom:* The 50% power-constrained 2σ upper limit and expected limits as above, but shown as the ratio of signal events to QED background.

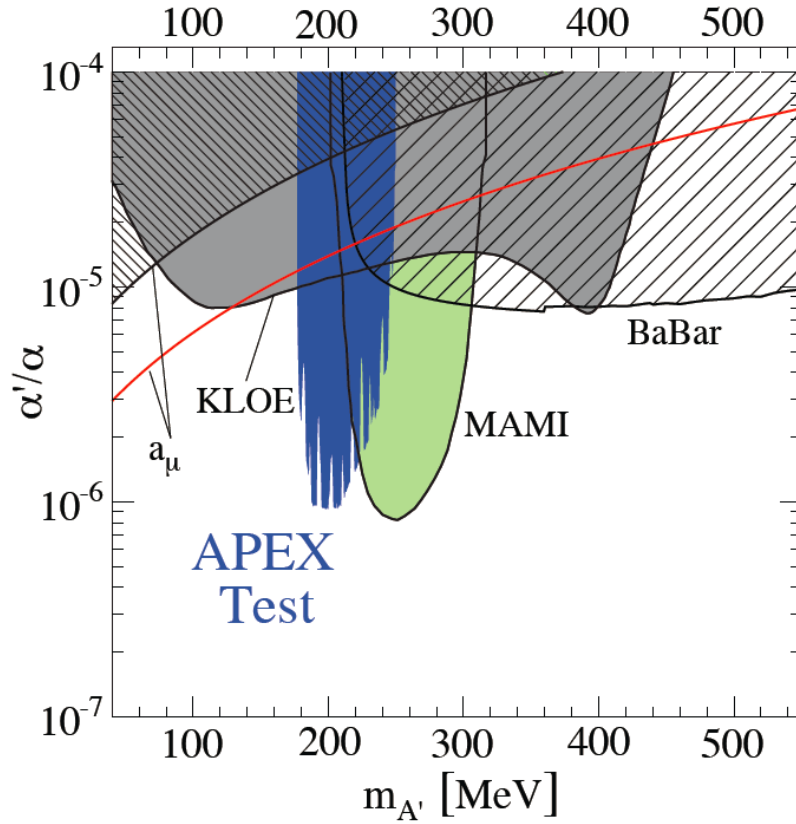


FIG. 8.8: The 2σ upper limit on $\alpha'/\alpha_{\text{fs}}$ versus A' mass for the APEX test run is shown in blue. Also shown are existing 2σ limits from the muon anomalous magnetic moment a_μ (fine hatched) [50], KLOE (solid gray) [16], the result reported by Mainz (green) [18], and an estimate using a BaBar result (wide hatched) [19].

9

Conclusion

The APEX test run found no evidence of $A' \rightarrow e^+e^-$ electro-production in the mass range 175-250 MeV. The data was used to place an upper limit of $\alpha'/\alpha_{\text{fs}} \simeq 10^{-6}$ in this mass range at 90% confidence. The full coverage in phase space from the test run data is shown in Fig. 8.8.

The test run demonstrated that the proposed experimental plan of the full APEX experiment is sound. It led to the construction of the specialized target described in Sec. 4.4.1 and acquiring the custom electronics required for the trigger. The software tools required to perform the peak search analysis were developed and used to perform a search on a significant amount of acquired data. All aspects discussed in [20] were demonstrated to work, and the full APEX experiment will be ready to run as early as possible.

9.1 Impact of the APEX Test Run Results

The existence of a new light gauge boson with small coupling to electrically charged matter is one of the only ways new forces can couple to the Standard Model. The existence of such a particle is motivated by recent astrophysical anomalies, and may also be the solution to the muon anomalous magnetic moment discrepancy. Therefore, the possible existence of A' bosons must not be overlooked. Although the APEX test run did not find evidence of an A' , it succeeded in excluding its possible existence in a highly motivated region of parameter space. The results of the test run contributed to the ongoing efforts of other experimental searches to explore all possible A' masses and couplings.

In Fig. 8.8, the area between the red line and the fine hatched region is where the A' can explain the observed discrepancy between the calculated and measured muon anomalous magnetic moment at 90% confidence. Part of this area is excluded by the test run analysis, confirming results reported by KLOE, BaBar, and MAMI. The full APEX experiment will roughly cover the entire area of this plot.

9.2 Future Experiments

In addition to APEX, two other experiments at Jefferson Lab will search for the A' . Fig. 9.1 shows the areas of parameter space that will be covered by these experiments. The APEX search region is outlined in purple. The Heavy Photon Search (HPS) [14] will run in Hall B. It will search for electro-produced A' s using

both invariant mass and separated decay vertex signatures using a compact, large acceptance forward spectrometer. Because it can measure A' decays with vertex positions located far away from the trident background, HPS is sensitive to values of α'/α_{fs} as small as 10^{-10} . The HPS search regions are outlined in red, with the lower area corresponding to the region where the vertex of the A' decay is displaced. The Dark Light experiment [51] will search for A' 's using Jefferson Lab's Free Electron Laser (FEL). The sensitivity of Dark Light is outlined in blue.

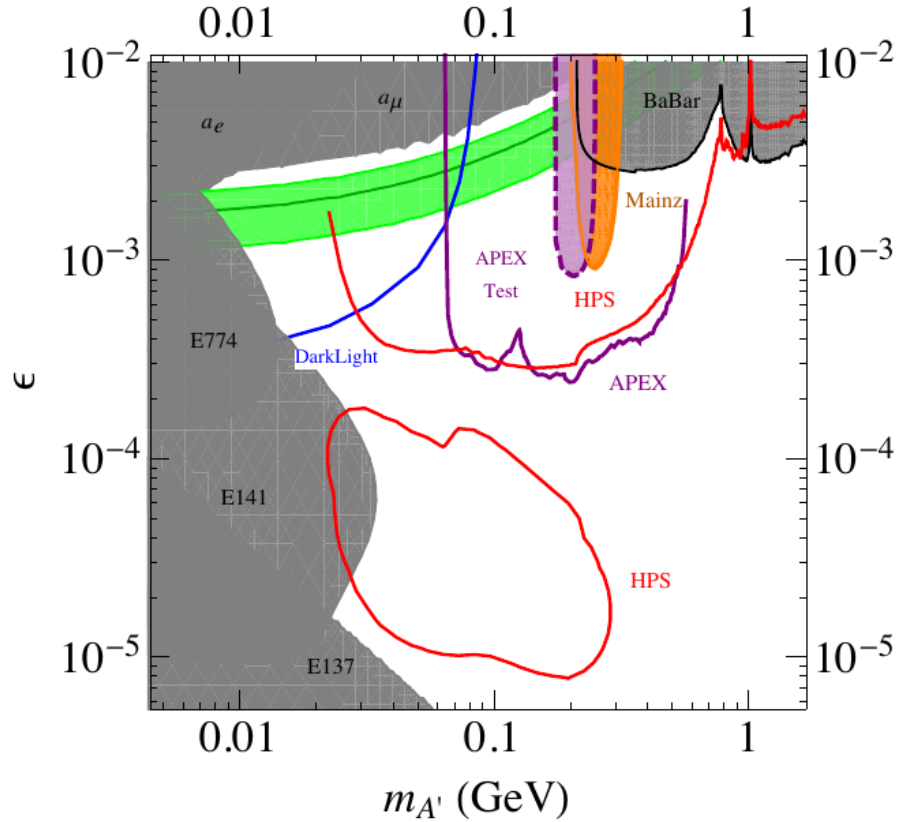


FIG. 9.1: Sensitivity of future A' searches at Jefferson Lab. Shown are the expected search regions of the APEX (purple), HPS (red), and Dark Light (blue) experiments.

In summary, the APEX test run results put new constraints on the existence of a new A' boson, contributing to the overall effort to explore a highly motivated

region of phase space. The results of the test run demonstrate that fixed-target searches can explore a wide range of masses and couplings for sub-GeV forces.

LIST OF TABLES

Table	Page
3.1 Characteristics of the Hall A High Resolution Spectrometers	30
4.1 Expected rates for APEX experiment	64
5.1 Triggers of the APEX test run.	72
6.1 Summary of the angular calibration runs	94
7.1 Loose cuts for track determining reconstruction efficiency	111
7.2 Summary of the contributions to the angular resolution.	122

LIST OF FIGURES

Figure	Page
1.1 A' bremsstrahlung and decay into an e^+e^- pair	4
1.2 Motivated region of parameter space	6
2.1 Kinetic mixing Feynman diagram	10
2.2 PAMELA results	12
2.3 Leading order contributions to a_μ	15
2.4 Current limits	16
2.5 Anticipated sensitivity for APEX	19
3.1 The CEBAF accelerator layout for 6 GeV operation	22
3.2 Top view of Hall A	24
3.3 The beam position monitors	27
3.4 Rastered beam spot	28
3.5 Layout of the HRS	29
3.6 Side view of the detector stack	31
3.7 Vertical drift chambers	33
3.8 S2m scintillator plane	34
3.9 Gas Cherenkov counter	36
3.10 Lead glass calorimeters	37
4.1 A' production off a fixed target	41
4.2 Diagrams of the QED background processes	45
4.3 Electron momentum vs. positron momentum simulation	46
4.4 APEX sensitivity for different energy settings	48
4.5 The layout of the experimental setup	52
4.6 Final design of the APEX target	54

4.7	SciFi detector	59
4.8	APEX trigger	61
4.9	Sparsification timing diagram	62
5.1	The lead target	69
5.2	The septum magnets	70
5.3	Trigger electronics for the test run	73
6.1	Timing alignment of the S2m plane	76
6.2	Gas Cherenkov PMT amplitude sum	78
6.3	VDC time offset calibration.	80
6.4	Raster current vs. beam position	82
6.5	Coordinate systems	86
6.6	Schematic of sieve slit setup	90
6.7	Reconstructed foil positions	92
6.8	Reconstructed sieve holes after calibration	93
6.9	Results of δ calibration	95
7.1	Particle identification	100
7.2	Coincidence timing spectrum	103
7.3	PREX collimator	104
7.4	Geometrical acceptance cuts	105
7.5	VDC cluster example	108
7.6	VDC track reconstruction	110
7.7	Tracking modifications	111
7.8	Loose cuts for determining track reconstruction efficiency	112
7.9	Invariant mass spectrum of the test run data	115
7.10	Comparison of the test run data and calculated invariant mass spectrum	116
7.11	Comparison of the test run data and calculated angular distributions	117
7.12	1D reconstructed spatial distributions of a sieve hole.	121
7.13	Difference between simulated and real invariant mass	123
7.14	Mass resolution as a function of invariant mass	123
7.15	VDC wire efficiency	127
7.16	VDC drift time for high rate data	127
7.17	VDC drift time-to-distance calibration	128
7.18	VDC cluster size	129
7.19	PID at high rates	130

8.1	Bell curve	135
8.2	Toy function	136
8.3	Relation of p -value to the test statistic t and significance Z	139
8.4	Setting a limit on the observed p -value	141
8.5	Pulls generated from different bin sizes	143
8.6	Window size and polynomial order	145
8.7	Local p -values and the upper bound on number of signal events . . .	149
8.8	Test run exclusion limits of α'/α_{fs}	150
9.1	Sensitivity of future A' searches	153

BIBLIOGRAPHY

- [1] J. D. Bjorken, R. Essig, P. Schuster, and N. Toro, arXiv:arXiv:0906.0580 [hep-ph] (2009).
- [2] M. Endo *et al.*, arXiv:1209.2558 [hep-ph] (2012).
- [3] J. L. Hewett *et al.* (2012), pp. 131–150.
- [4] O. Adriani *et al.*, arXiv:0810.4995 [astro-ph] (2009).
- [5] M. Ackermann *et al.*, arXiv:1008.3999 [astro-ph.HE] (2010).
- [6] J. Chang *et al.*, Nature **456**, 362 (2008).
- [7] F. Aharonian *et al.*, arXiv:0811.3894 [astro-ph] (2008).
- [8] B. Holdom, Phys. Lett. B **166**, 196 (1986).
- [9] D. Finkbeiner *et al.*, arXiv:1011.3082 [hep-ph] (2011).
- [10] O. Adriani *et al.*, arXiv:0810.4994 [astro-ph] (2009).
- [11] M. Kamionkowski, arXiv:hep-ph/9710467 (1997).
- [12] J. L. Feng *et al.*, arXiv:1005.4678 [hep-ph] (2010).
- [13] G. W. Bennett *et al.*, arXiv:hep-ex/0602035 (2006).

- [14] P. H. Adrian *et al.*, *Heavy Photon Search Experiment at Jefferson Laboratory: proposal for 2014-2015 run*, Tech. Rep., Jefferson Lab (2013), https://confluence.slac.stanford.edu/download/attachments/86676777/hps_2014.pdf.
- [15] S. Andreas *et al.*, arXiv:1209.6083 [hep-ph] (2012).
- [16] F. Archilli *et al.*, arXiv:1107.2531 [hep-ex] (2011).
- [17] S. Abrahamyan *et al.*, arXiv:1108.2750 [hep-ex] (2011).
- [18] H. Merkel *et al.*, arXiv:1101.4091 [nucl-ex] (2011).
- [19] B. Aubert *et al.*, arXiv:0905.4539 [hep-ex] (2009).
- [20] J. D. Bjorken *et al.*, *The A' Experiment (APEX): Search for a New Vector Boson A' Decaying to e^+e^-* , Tech. Rep., Jefferson Lab (2010), <http://hallaweb.jlab.org/collab/PAC/PAC37/E12-10-009-APEX.pdf>.
- [21] C. W. Leemann, D. R. Douglas, and G. A. Krafft, *Annu. Rev. Nucl. Sci.* **51**, 413 (2001).
- [22] K. Unser, *Nucl. Sci.* **28**(3), 2344 (1981).
- [23] J. Alcorn *et al.* (Hall A Collaboration), *Nucl. Phys.* **A522**, 294 (2004).
- [24] W. Barry, *Basic Noise Considerations for CEBAF Beam Position Monitors*, Tech. Rep. JLab-TN-91-087, Jefferson Lab (1991).
- [25] K. Fissum *et al.*, *Nucl. Phys.* **A474**(2), 108 (2001).
- [26] Hall A Collaboration, *JLab Hall A General Operations Manual*, Tech. Rep., Jefferson Lab (2008), hallaweb.jlab.org/experiment/E05-102/e05-102/docs/osp_4.pdf.

- [27] W. A. Watson, J. Chen, G. Heyes, E. Jastrzembski, and D. Quarrie, *CODA: A scalable, distributed data acquisition system*, Tech. Rep., Jefferson Lab (1993).
- [28] R. Essig, P. Schuster, and N. Toro, arXiv:0903.3941 [hep-ph] (2009).
- [29] K. J. Kim and Y. Tsai, Phys. Rev. D **8**, 3109 (1973).
- [30] J. Alwall, P. Demin, S. de Visscher, R. Frederix, M. Herquet, *et al.*, arXiv:0706.2334 [hep-ph] (2007).
- [31] S. Abrahamyan *et al.*, *Searching for a New Gauge Boson at JLab Workshop*, Tech. Rep., Jefferson Lab (2010), <http://www.jlab.org/conferences/boson2010/program.html>.
- [32] I. Rachek *et al.*, *Hall A Annual Report*, Tech. Rep., Jefferson Lab (2007).
- [33] I. Rachek and B. Wojtsekhowski, *Reduction of DAQ dead time in Hall A experiments*, Tech. Rep. JLab-TN-11-017, Jefferson Lab (2011).
- [34] H. E. Montgomery *et al.*, *JLab PAC35 Report*, Tech. Rep., Jefferson Lab (2010), http://www.jlab.org/exp_prog/PACpage/PAC35/PAC35_report.pdf.
- [35] S. Abrahamyan *et al.* (PREX Collaboration), arXiv:1201.2568 [nucl-ex] (2012).
- [36] S. Riordan, *Measurements of the Electric Form Factor of the Neutron at $Q^2 = 1.7$ and 3.5 GeV²*, Ph.D. thesis, Carnegie Mellon University (2008).
- [37] M. Mihovilovic, *Measurement of double polarized asymmetries in quasi-elastic processes $^3\vec{\text{He}}(\vec{e}, e'd)$ and $^3\vec{\text{He}}(\vec{e}, e'p)$* , Ph.D. thesis, University of Ljubljana (2012).
- [38] N. Liyanage, *Optics Calibration of the Hall A High Resolution Spectrometers using the new optimizer*, Tech. Rep. JLAB-TN-02-012, Jefferson Lab (2002).

- [39] J. Huang, *Double Spin Asymmetry A_{LT} in Charged Pion Production from Deep Inelastic Scattering on a Transversely Polarized ^3He Target*, Ph.D. thesis, Massachusetts Institute of Technology (2012).
- [40] Y. Qiang, *Search for Pentaquark Partners Θ^{++} , Σ^0 and N_0 in $H(e, e'K(\pi))X$ Reactions at Jefferson Lab Hall A*, Ph.D. thesis, MIT (2007).
- [41] O. Hanson, *ROOT/C++ Analyzer for Hall A* (2012), <http://hallaweb.jlab.org/podd/>.
- [42] R. Brun, *ROOT, An Object-Oriented Data Analysis Framework* (2013), <http://root.cern.ch/drupal/>.
- [43] A. Orsborn, *Assessment of Hall A Vertical Drift Chamber Analysis Software Performance Through Monte Carlo Simulation*, Tech. Rep. JLAB-TN-05-069, Jefferson Lab (2005).
- [44] H. A. Bethe, *Phys. Rev.* **89**, 1256 (1953).
- [45] B. Wojtsekhowski, *APEX: A Search for Dark Photons in Hall A (E12-10-009)* (2012), http://hallaweb.jlab.org/collab/meeting/2012-winter/talks/Tuesday%20Afternoon/Wojtsekhowski_APEX.pdf.
- [46] G. Ranucci, arXiv:1201.4604 [physics.data-an] pp. 77–85 (2012).
- [47] S. S. Wilks, *The Annals of Mathematical Statistics* **9**, 60 (1938).
- [48] E. Gross and O. Vitells, arXiv:1005.1891 [physics.data-an] (2010).
- [49] G. Cowan, K. Cranmer, E. Gross, and O. Vitells, arXiv:1105.3166 (2011).
- [50] M. Pospelov, arXiv:0811.1030 [hep-ph] (2009).

- [51] P. Balakrishnan *et al.*, *A Proposal for the DarkLight Experiment at the Jefferson Laboratory Free Electron Laser*, Tech. Rep., Jefferson Lab (2010), http://dmtpc.mit.edu/twiki/pub/Projects/DarkLight/Proposal_a_4Dec2010.pdf.